
Microscopy of Spin-Charge Dynamics in Fermi-Hubbard Chains

Jayadev Vijayan



München 2020

Microscopy of Spin-Charge Dynamics in Fermi-Hubbard Chains

Dissertation an der Fakultät für Physik
Ludwig-Maximilians-Universität München



vorgelegt von
Jayadev Vijayan
aus Trichur, Indien

München, 16.12.2019

Tag der mündlichen Prüfung: 07.02.2020

Erstgutachter: Prof. Immanuel Bloch

Zweitgutachter: Prof. Ulrich Schollwöck

Weitere Prüfungskommissionsmitglieder: Prof. Matthias Kling, Prof. Jan Lipfert

Zusammenfassung

Ein mikroskopisches Verständnis für die Dynamik in stark korrelierten elektronischen Systemen zu erhalten, ist seit vielen Jahrzehnten eine Herausforderung geblieben. Das Wechselspiel zwischen den Spin- und Ladungsfreiheitsgraden in diesen Materialien bei verschiedenen Temperaturen und unterschiedlicher Dotierung ist bisher nicht gut verstanden und weiterhin ein Gebiet, auf dem intensiv Forschung betrieben wird.

In letzter Zeit haben sich Quantensimulatoren basierend auf ultrakalten Atomen in optischen Gittern als vielversprechende Plattform für die Erforschung stark korrelierter fermionischer Systeme herausgebildet. Diese Doktorarbeit beschäftigt sich mit den an einem Quantengasmikroskop mit fermionischem ${}^6\text{Li}$ durchgeführten Experimenten, in denen Fermi-Hubbard-Systeme präpariert und einzelne Gitterplätze und Spins aufgelöst werden können.

Die Hauptergebnisse dieser Arbeit erforschen die mikroskopische Dynamik in eindimensionalen Materialien, worin individuelle Bausteine wie das Elektron mit Ladung e und Spin $1/2$ nicht mehr relevant für die Beschreibung des Systems sind und stattdessen durch kollektive Spin- und Ladungsanregungen, die sich unabhängig voneinander bewegen können, ersetzt werden - ein Phänomen namens Spin-Ladungs-Trennung. In unserem Quantensimulator benutzen wir analoge eindimensionale Fermi-Hubbard-Ketten aus ${}^6\text{Li}$, um zeit- und orts aufgelöste Mikroskopie der durch einen lokalen Quench entstehenden Spin- und Ladungsanregungen durchzuführen. Durch die Detektion signifikant unterschiedlicher Geschwindigkeiten und den Nachweis einer fehlenden Bindung zwischen den Anregungen demonstrieren wir Spin-Ladungs-Trennung. Unsere mikroskopische Methode ermöglicht uns weiterhin, den zusätzlichen Spin der Spinanregung quantitativ zu bestimmen, was unsere Ergebnisse mit dem Effekt der Fragmentierung in Verbindung bringt.

In einem weiteren Experiment werden Fermi-Hubbard-Ketten im Gleichgewicht präpariert und inkommensurable Spin-Korrelationen beobachtet, die in der Gegenwart von Dichtedotierung und Spinpolarisierung auftreten. Der Wellenvektor dieser inkommensurablen Korrelationen zeigt einen linearen Zusammenhang zwischen Dotierung und Polarisierung.

Zuletzt wird das Wechselspiel zwischen Spin und Ladung im Übergang zwischen einer und zwei Dimensionen untersucht. Die Spin-Korrelationen in der Umgebung der Störstelle zeigen einen drastischen Unterschied im zweidimensionalen Fall und die in einer Dimension präsenten antiferromagnetischen Korrelationen verschwinden. Im Fall einer einzelnen Störstelle in einem reinen zweidimensionalen System offenbart sich das Wechselspiel zwischen Spin und Ladung als deformierte Spinwolke in der Umgebung der Störstelle und deutet auf die Bildung eines magnetischen Polarons hin.

Die hier dargestellten Experimente demonstrieren die Fähigkeiten eines Quantensimulators; durch Messungen an einem stark korrelierten System im Ortsraum mit mikroskopischer Auflösung einzelner Gitterplätze können wir auftretende Phänomene studieren, Theorien überprüfen und Bereiche erforschen, die mit anderen experimentellen Plattformen nicht erreichbar sind.

Abstract

Obtaining a microscopic understanding of the dynamics in strongly correlated electronic systems has remained a challenge for many decades. The interplay between the spin and charge degrees of freedom in these materials at different temperatures and dopant concentrations is not well understood and is still an area of intense scientific research.

Recently, quantum simulators based on ultracold atoms in optical lattices have emerged as a promising platform to probe strongly correlated fermionic systems. This thesis reports on the work carried out with a quantum gas microscope of ultracold fermionic ${}^6\text{Li}$, where Fermi-Hubbard systems are prepared and imaged with single site spin and density resolution.

The main results of the thesis explore the microscopic dynamics underlying one-dimensional materials, where individual constituents such as the electron with charge e and spin $1/2$ are not relevant to the description of the system anymore and are instead replaced by spin and charge excitations that can propagate independent of one another - a phenomenon called spin-charge separation. In our quantum simulator, we use analogous one-dimensional Fermi-Hubbard chains of ${}^6\text{Li}$, to perform time- and space-resolved microscopy of the spin and charge excitations following a local quench. By extracting their strikingly different velocities and showing an absence of binding between the excitations, we demonstrate spin-charge separation. Our microscopic technique also allows us to quantitatively extract the excess spin carried by the spin excitation, connecting our results to the phenomenon of fractionalization.

In another set of experiments, Fermi-Hubbard chains are probed at equilibrium and incommensurate spin correlations arising in the presence of both density doping and spin polarization are observed. The wavevector of these incommensurate correlations are found to have a linear dependence on doping and polarization.

Finally, the effect of the spin-charge interplay is probed in the crossover from one to two dimensions. The spin correlations across dopants are seen to be dramatically different in two dimensions, and the strong antiferromagnetic correlations across dopants present in one dimension disappear. For a single dopant in a fully two dimensional system, the spin-charge interplay manifests as a distorted spin cloud surrounding the dopant, indicating the formation of a magnetic polaron.

The experiments reported here demonstrate the power of a quantum simulator; by probing the physics of strongly correlated systems in real space with unprecedented resolution, we can zoom into emergent phenomena, validate theories and access regimes that are not possible in other experimental settings.

Contents

1	Introduction	1
2	Background	7
2.1	The Fermi-Hubbard model	7
2.1.1	Phase diagram	8
2.1.2	t - J and Heisenberg models	10
2.2	Ultracold atom quantum simulator	11
2.2.1	Optical lattices	11
2.3	Doping one-dimensional antiferromagnets	13
2.3.1	Incommensurate magnetism	14
2.3.2	Spin-charge separation	15
2.3.3	Beyond the Luttinger liquid regime	17
2.4	Doping two-dimensional antiferromagnets	22
2.5	Experimental limitations	24
3	A Fermi gas microscope	25
3.1	Properties of Lithium	25
3.2	Preparation of degenerate Fermi gases	26
3.3	Optical lattices	30
3.4	Single site resolved imaging	31
3.4.1	Raman sideband cooling in a pinning lattice	32
3.4.2	Single site density resolution	33
3.4.3	Single site spin resolution	35
3.5	Antiferromagnetic correlations in Hubbard chains	36
4	Real-space observation of incommensurate magnetism	39
4.1	Experimentally probing incommensurate magnetism	40
4.2	Effect of doping on spin correlations	41
4.3	Effect of magnetization on spin correlations	44
4.4	Conclusion	47

5 Spin-charge dynamics in one dimension	49
5.1 Quenching one dimensional antiferromagnets	50
5.1.1 Pushout beam	51
5.1.2 System preparation	53
5.2 Dynamics of holons and spinons	54
5.2.1 Holon dynamics	54
5.2.2 Extraction of holon velocity	56
5.2.3 Spinon dynamics	57
5.2.4 Extraction of spinon velocity	58
5.3 Theoretical extraction of velocities	59
5.3.1 Extended $t - J$ model	59
5.3.2 Heisenberg model for the spinons	61
5.4 Spatial separation of spin and charge excitations	63
5.4.1 Tracking spin correlations across a hole	63
5.4.2 Overlap of holon and spinon distributions	64
5.4.3 Absence of binding beyond the nearest neighbor	65
5.5 Connection to spin-charge fractionalization	67
5.5.1 Fractionalization at zero temperature	67
5.5.2 Fractionalization at non-zero temperature	69
5.6 Extracted velocity dependence on t and J	73
5.7 Conclusion	75
6 Crossing over from one to two dimensions	77
6.1 Development of correlations in two dimensions	78
6.1.1 Preparing two dimensional systems	78
6.1.2 Spin correlations across dopants	80
6.2 Single dopant in a two dimensional antiferromagnet	82
6.2.1 Formation of magnetic polarons	82
6.3 Conclusion	85
7 Summary and outlook	87
Bibliography	91
Acknowledgements	109

Chapter 1

Introduction

In a system of many interacting particles, the emerging degrees of freedom can fundamentally differ from those of its individual constituents. Complexity can arise from the simplest of ingredients and if the underlying physics is not well understood, the outcomes of the interactions can be unpredictable. Decades of work have been put in by scientists to understand such emergent phenomena and is at the foundation of many unsolved problems in physics today. This is especially true in the study of condensed matter systems - where the interactions between electrons give rise to a wide range of macroscopically observable phenomena.

Understanding the microscopic principles underlying these phenomena has been a challenge both theoretically and experimentally. From a theoretical point of view, the Hilbert space of a system of N interacting quantum particles scales as 2^N , and calculating properties of systems with even a few tens of particles quickly becomes computationally unfeasible. From an experimental point of view, probing the interplay of various processes in matter microscopically at length scales of 10^{-10} m and time scales of femtoseconds, is extremely challenging.

It is with such challenges in mind that Richard Feynman proposed the use of quantum simulators [1] - a precisely controllable analogous experimental system that mimics an interacting quantum system with many degrees of freedom [2] - to study the emergence of complexity.

As he put it himself - "Nature isn't classical, dammit, and if you want to make a simulation of nature, you'd better make it quantum mechanical, and by golly it's a wonderful problem, because it doesn't look so easy".

Quantum simulation with ultracold atoms

The idea of simulating interacting quantum systems with neutral atoms relies heavily on pioneering work done previously on cooling atoms down to degeneracy. S. Chu, C. Cohen-Tannoudji and W.D. Phillips won the Nobel prize in physics (1997) "for the development of methods to cool and trap atoms with laser light". Following earlier proposals [3] and combining the technique of slowing down heated atoms using a counter-propagating laser beam and a coil with varying magnetic field (Zeeman slower) [4] with the technique of laser cooling with three orthogonal pairs of counter-propagating laser beams (optical molasses) [5, 6], they had successfully managed to cool and trap atoms at microkelvin temperatures. Further improvements in cooling include the development of polarization-gradient cooling [7, 8] and sideband cooling [9].

The first successful attempts at cooling all the way to degeneracy - the creation

of a Bose-Einstein condensate - was achieved by E. A. Cornell, W. Ketterle and C. E. Wieman with Sodium and Rubidium atoms [10, 11], for which they were awarded the Nobel prize in 2001. Bose-Einstein condensates with bosonic Lithium was achieved soon after [12]. The key step in going from microkelvin to nanokelvin temperatures was a process called “evaporative cooling”, by which hotter atoms were allowed to leave the trap while the colder atoms interacted with one another to rethermalize at a lower temperature.

The development of a degenerate gas of fermions was a harder challenge and consequently took longer to achieve. The primary difficulty lies in adapting evaporative cooling to fermions where rethermalization from collisions between atoms is hard to engineer. In order to make the fermions rethermalize, evaporative cooling was performed with spin mixtures [13, 14] and later with mixtures of different atomic species [15–18].

Following the successful realization of degenerate Bose and Fermi gases, efforts were made to realize strongly correlated systems which would act as a quantum simulator for many condensed matter systems that involve particle moving along a lattice and interacting with one another.

One way to engineer enhanced interactions between atoms is to use Feshbach resonances to control their scattering lengths, thereby allowing tunable interactions between atoms. Such strongly interacting Fermi gases were realized [19, 20] and studies on fermion pairing and superfluidity were carried out [21–27].

However, the strongly correlated regime can alternatively also be achieved by suppressing the kinetic energy of atoms using an optical lattice [28]. The realization of strongly correlated many-body systems in optical lattices was confirmed with the observation of the superfluid - Mott insulator transition with bosons [21]. This platform paved the way for theoretical proposals and experiments [29–33] on the quantum simulations of solid state systems, given the control that could be achieved with cold atoms (bosons and fermions) in optical lattices [34–38].

Probing with single site resolution

One of the major limitations of experiments in condensed matter physics probing strongly correlated systems in real materials (as opposed to synthetic materials in a quantum simulator) is the lack of microscopic observables. They typically rely on extracting global observables of the materials using spectroscopic [39–43] or conductance measurement techniques [44–50] to probe the underlying physics. There have been no experiments which could probe the lattices with the resolution of a single site.

With strongly correlated ultracold atoms in optical lattices, however, the lattice spacing can be as high as a few micrometers, which can be resolved easily with existing techniques in optical microscopy. A quantum gas microscope takes advantage of the relatively large spacings in an optical lattice to perform in-situ single-site resolved fluorescent imaging. To image atoms trapped in a lattice, it is necessary to cool them in-situ while the fluorescent photons are being collected [51, 52].

The first quantum gas microscope experiments were performed with bosonic ^{87}Rb [53, 54]. They were soon able to demonstrate the transition to a Mott insulator with single-site resolution [54–56], observe the spreading of correlations [57],

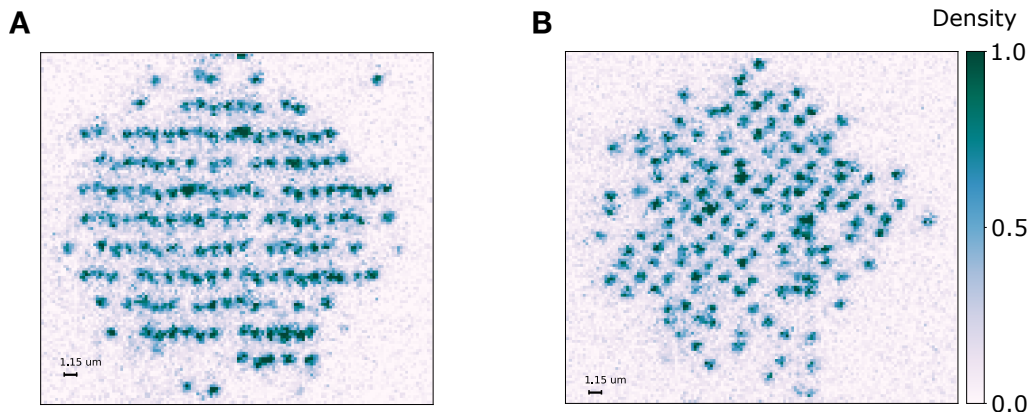


FIGURE 1.1: **Quantum gas microscopy with single site resolution.** **A**, Fluorescence signal from atoms in an optical lattice, forming a Mott insulator. By looking at the distribution of number of photons originating from a single lattice site, the density per lattice site can be reconstructed. Spin resolution at the single site is obtained, in our case, by employing a Stern-Gerlach splitting of the lattice gas before imaging, as shown in **(B)**. Details of the imaging scheme are described in Chapter 3.

antiferromagnetic spin-1/2 chains [58] and the Higgs amplitude mode [59]. Experiments studying the dynamics of many-body systems out-of-equilibrium were also carried out with single-site resolution [60], for example, the observation of quantum walks [61] and magnon bound states [62] and measurement of entanglement entropy [63].

Challenges in adapting the cooling techniques from bosons to alkaline fermions (mainly ${}^6\text{Li}$ and ${}^{40}\text{K}$) resulted in a delay in the emergence of fermionic quantum gas microscopes. The main reasons are the presence of a small excited state hyperfine splitting and low mass, which make standard laser cooling during the imaging challenging.

In 2015, however, several groups independently reported single-site resolved imaging of fermions in optical lattices, using different imaging techniques, such as electromagnetically induced transparency [64], Raman sideband cooling [65–67] and others [68, 69]. Later experiments with fermionic quantum gas microscopes have realized Mott insulators [70, 71], band insulators [67] and systems with anti-ferromagnetic correlations [71–74].

The various phases emerging in solid state materials have at their origin the interplay between the spin order of the fermionic electrons (fermionic atoms in the quantum simulator) and the kinetic energy of charge impurities (holes or doublons - sites with no atom or two atoms in the lowest band respectively). To probe the phases microscopically thus requires the ability to simultaneously resolve charge (density) and spin at every lattice site. While other Fermi gas experiments require removing the two different spin components in successive snapshots, our experiment (see Fig. 1.1) has the ability to detect both these quantities in a single snapshot, enabling the measurement of local as well as multipoint spin correlation functions.

Using the various techniques discussed in this chapter, which were developed

over decades, we have the tools required to perform experiments that go in the direction of Feynman’s original proposal - to probe the fundamental processes underlying complex many-body systems microscopically by using synthetic quantum matter.

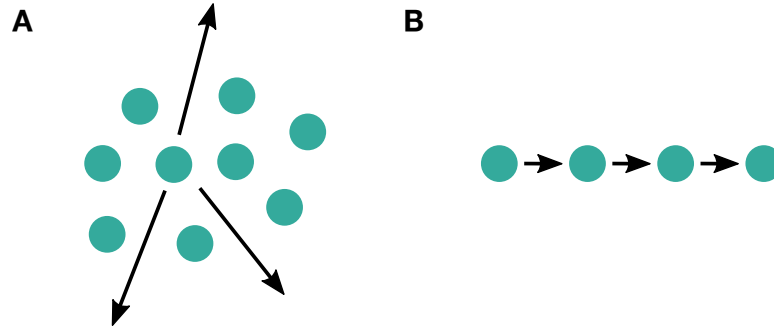


FIGURE 1.2: **Behaviour of many-body systems in different dimensions.** **A**, In systems where particles are allowed to move anywhere on a plane, free quasiparticle excitations that resemble individual particles can exist. **B**, However, when the only way for a particle to move is by pushing its neighbour, the individual particle excitations are replaced by *collective* excitations. Idea for illustration taken from [75].

This thesis mainly reports on experiments performed with an ultracold quantum simulator using fermionic lithium atoms trapped in 1D and 2D optical lattices. The underlying physics in different dimensions can be dramatically different, as illustrated in Fig. 1.2. The microscopic insight emerging from our experiments have been able to demonstrate certain phenomena that have been predicted to exist theoretically, but have been hard to prove directly and unambiguously in traditional condensed matter physics experiments. In particular, we demonstrate the presence of incommensurate spin correlations and spin-charge separation in 1D Fermi-Hubbard chains and the breakdown of spin-charge separation and the formation of magnetic polarons in 2D systems.

I have tried to keep the contents presented here as self-contained as possible and in places where this was not possible, provided references to follow.

This thesis should be useful to give a curious reader an overview of the latest developments in the field of quantum simulation of the Fermi-Hubbard model. It should be able to provide an experimental physicist an idea of the tools and techniques used to prepare degenerate Fermi gases and perform single-site resolved microscopy of lattice gases. And finally, it should be accessible and of interest to a wide range of physicists who deal with the study of strongly correlated matter in a variety of different scenarios.

A summary of the organization of the chapters in this thesis is given below:

- **Chapter 2:** Provides a discussion of the relevant background necessary to understand the results present in the following chapters. A description of the Fermi-Hubbard model and how we use an ultracold atom quantum simulator to realize this model is reviewed. It also includes a basic discussion of the

phenomena of spin-charge separation, incommensurate magnetism and the formation of magnetic polarons, laying a foundation for the results of chapters 4, 5 and 6.

- **Chapter 3:** Is a summary of our experimental setup for quantum gas microscopy with fermions. Experimental sequences that lead to the Fermi-Hubbard systems needed for our studies are described. A discussion of the additional tools in imaging that enable spin-resolved characterization and results showing antiferromagnetic correlations is included.
- **Chapter 4:** Describes the experimental results pertaining to the real-space observation in equilibrium Fermi-Hubbard chains of incommensurate spin correlations. Incommensurate correlations arising both from density doping and spin imbalance are discussed in detail in the remainder of the chapter.
- **Chapter 5:** The time- and space-resolved observation of the phenomenon of spin-charge separation in one-dimensional chains following a local quench is described in detail. It first describes the experimental setup required to perform a quench and observe the resulting dynamics of spin and charge excitations through their signatures in the hole and nearest neighbour correlation distributions in the chain. Then, the methods used to extract the velocities of these quasiparticle excitations experimentally and theoretically are described. Finally, results arising from use of different observables in the analysis showing the absence of binding between the excitations, are discussed.
- **Chapter 6:** This chapter describes the fate of spin-charge separation in Fermi-Hubbard systems in the crossover from one to two dimensions. A description of the process of preparing two dimensional systems is included. The spin correlations across the dopants are shown to change dramatically in the crossover from 1D to 2D, indicating the formation of magnetic polarons. The second section summarizes the results from a dedicated set of experiments performed to probe the effect of a single dopant in a 2D antiferromagnet.
- **Chapter 7:** The results described in the previous chapters and summarized and put into perspective. Future and current directions being taken and techniques being implemented in the field of Fermi gas microscopy are discussed.

Chapters 4, 5 and 6 are largely based on results published in the following papers in which I have been an author:

1. *“Direct observation of incommensurate magnetism in Hubbard chains”*.
Guillaume Salomon, Joannis Koepsell, Jayadev Vijayan, Timon A. Hilker, Jacopo Nespolo, Lode Pollet, Immanuel Bloch and Christian Gross.
Nature **565**, 56–60 (2019)
2. *“Time-Resolved Observation of Spin-Charge Deconfinement in Fermionic Hubbard Chains”*.
Jayadev Vijayan, Pimonpan Sompert, Guillaume Salomon, Joannis Koepsell, Sarah Hirthe, Annabelle Bohrdt, Fabian Grusdt, Immanuel Bloch and Christian Gross.
Science **367**, 186–189 (2020)

3. *“Imaging magnetic polarons in the doped Fermi–Hubbard model”.*

Joannis Koepsell, Jayadev Vijayan, Pimonpan Sompert, Fabian Grusdt, Timon A. Hilker, Eugene Demler, Guillaume Salomon, Immanuel Bloch and Christian Gross.

Nature **572**, 358–362 (2019)

Chapter 2

Background

The results presented in this thesis comprise entirely of experiments performed on an analog quantum simulator using the platform of ultracold atoms in optical lattices. In order to develop a microscopic understanding of the phases emerging in quantum many-body systems, we perform single-site-resolved imaging of our lattice gas, enabling us to obtain a microscopic insight of the interplay between spin and charge.

The essential physics of these many-body systems is believed to be captured by the Hubbard model, which is widely used to model their effective electronic degrees of freedom. Our quantum simulator realizes the Fermi-Hubbard model with ultracold atoms, a description of which is provided in 2.1, to study the emergent physics of such systems.

The properties of ultracold fermionic atoms in optical lattices that enable the realization of the Fermi-Hubbard model, is discussed in Sec. 2.2. A conceptual description of the phenomena we probe in the experiments reported here - incommensurate magnetism and spin-charge separation in 1D Fermi-Hubbard chains and the formation of magnetic polarons in 2D Fermi-Hubbard systems - are discussed in Sec. 2.3 and Sec. 2.4 respectively. Parts of this chapter are adapted from the thesis of T. Hilker [76].

2.1 The Fermi-Hubbard model

A minimalistic model that is commonly used to describe strongly correlated fermionic many-body systems, with spins $\sigma \in \{\uparrow, \downarrow\}$ and in a lattice potential, is the (Fermi-) Hubbard model.

First introduced in the context of solid-state systems where crystal ions form a periodic lattice with electrons in the conduction band, it was used to study the magnetic properties and dynamics of electrons. [77, 78].

There are certain assumptions made in the derivation of the Fermi-Hubbard Hamiltonian. First, it is assumed that the system is limited to a single band of the lattice and the tunneling of particles is restricted to nearest neighbouring sites. These conditions hold in the tight-binding regime [79]. In solid-state systems, such a process occurs when electrons from the conduction band tunnel from one ion to another in the lattice, due to spatial overlap of their electronic wavefunctions. The second assumption is that only electrons on the same site interact. This is a result of the Coloumb interaction between two electrons, which in first order is limited to the

same lattice site. At longer distances, the contribution from the Coulomb interaction is assumed to be screened by the positively charged ions, and consequently, any long-range interaction is neglected.

The Fermi-Hubbard Hamiltonian has the form:

$$\hat{H} = -t \sum_{\langle i,j \rangle, \sigma} (c_{i,\sigma}^\dagger c_{j,\sigma} + h.c.) + U \sum_i n_{i\uparrow} n_{i\downarrow} \quad (2.1)$$

where $c_{i,\sigma}^\dagger$ and $c_{i,\sigma}$ are the creation and annihilation operators of Wannier states on site i and spin σ respectively, the first term of the Hamiltonian is summed over nearest neighbouring sites and h.c. is the Hermitian conjugate.

The first term of the Hamiltonian describes the tunneling of fermions between adjacent sites. It is the kinetic energy term which favours the delocalization of fermions across the lattice.

The second term describes the cost of finding two fermions on the same site. Under the assumption that only the lowest band is occupied, the two fermions necessarily have different spin states, by Pauli's exclusion principle.

A third term can be added to the Hamiltonian to describe the effect of spatial inhomogeneity in the lattice potential:

$$\hat{H}_{\text{pot}} = \sum_{i,\sigma} \epsilon_i n_{i,\sigma} \quad (2.2)$$

It corrects the local potential of each site by ϵ_i . The relative energy differences between neighbouring sites can be neglected as long as the difference is smaller than the local energy width of the band, which is given by $4t$ along a lattice axis in the tight-binding limit.

Such a Hamiltonian also accurately describes our experimentally realized systems of fermionic atoms in optical lattices, making it an ideal simulator. The exact mapping of the terms of the Fermi-Hubbard Hamiltonian in cold-atom optical lattice systems is described in Sec. 2.2.

2.1.1 Phase diagram

Many-body systems studied in condensed matter physics such as cuprates - solid state materials which contain within them copper oxide planes - exhibit a wide range of phases, the existence of which have been confirmed empirically by experiments, producing a phase diagram as shown in Fig. 2.1. However, an understanding of the underlying microscopic mechanism leading to these emergent phases is still a subject of debate.

The repulsive branch of the Fermi-Hubbard model ($U/t \gg 1$) is believed to capture many of the phases shown in Fig. 2.1. The fact that the seemingly simple Hubbard model cannot be solved numerically has motivated many laboratories around the world to pursue experiments to explore the origins of these phases.

An attractive branch of the Fermi-Hubbard model also exists [81, 82] where the different spin states are mapped to doubly occupied sites and holes. Several experiments have been carried out exploring the regime of attractive interactions [83–92].

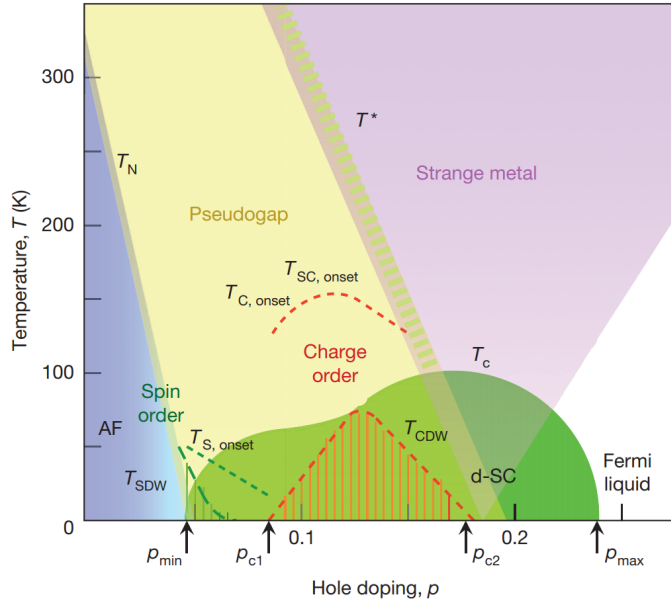


FIGURE 2.1: **Temperature vs doping phase diagram for cuprates.** At low temperatures and no doping, the dominant phase has antiferromagnetic spin order. All the other exotic phases, such as the pseudogap, strange metal and d -wave superconducting phase, occur when antiferromagnets are doped to different levels at different temperatures. Figure is taken from [80].

However, since all the work reported here are in the regime of repulsive interactions, the attractive branch is not discussed in any detail.

The three major energy scales of importance are that of t , U and the spin exchange amplitude $J = 4t^2/U$. The former two describe the motional degrees of freedom (“charge sector”), and the latter describes the spin degrees of freedom (“spin sector”).

Let us first look at the phases present at half-filling, when there is no doping. At high temperatures ($T \gg t$ and $T > U$), the system exhibits metallic properties [93]. There is an absence of any kind of density/charge ordering as the atoms are delocalized throughout the system. This can be understood as a weakly interacting state with an incompletely filled band.

Increasing the repulsive interactions ($U/t \gg 1$) introduces an energy cost for having more than one atom per site. As a result, a Mott insulating state is formed, which is different from the band insulator in that there is only one atom per site.

At lower temperatures ($k_B T \approx J = 4t^2/U$), the spin degrees of freedom of the Mott insulator come into play. Atoms with opposite spins on neighbouring sites can exchange their spins via a second order tunneling process which has a coupling strength of $J = 4t^2/U$. Such a process is forbidden for atoms with parallel spins on adjacent sites due to Pauli’s exclusion principle, leading to an energy cost of J for every pair of adjacent parallel spins. Thus, at temperatures $T < J$, it becomes energetically unfavourable to have two spins of the same kind on adjacent sites, leading to antiferromagnetic spin order. Any entropy present in such systems is transferred into the spin sector and the charge sector remains “frozen”. The system can then be described by the Heisenberg model, discussed in the Sec. 2.1.2.

Now let us look at phases that emerge away from half-filling, in the presence of

finite doping. Doping a Mott insulating system with antiferromagnetic correlations, depending on the level of doping, leads to the emergence of many interesting phases - a pseudogap [94, 95], strange metal, commensurate and incommensurate antiferromagnetic phase [96] and at lower temperatures, a d -wave superconducting phase [43, 97, 98].

The fundamental building block of these phases occurring in two and three dimensions is a single dopant in an antiferromagnetic system. We perform experiments realizing precisely such a situation and the results are discussed in Chapter 6.

The physics of the Fermi-Hubbard model changes dramatically depending on dimensionality already at the level of a single dopant and consequently, a single dopant in two dimensions behaves fundamentally differently from a single dopant in one dimension, as we shall see.

2.1.2 t - J and Heisenberg models

Almost all the experiments described in this thesis are performed in the presence of doping. In the limit $U \gg t$ and in the presence of doping, the Fermi-Hubbard model can in leading order of t/U , be approximated by the $t - J$ model [99]:

$$\hat{H}_{t-J} = \hat{\mathcal{P}} \left[-t \sum_{\langle i,j \rangle, \sigma} \hat{a}_{i,\sigma}^\dagger \hat{a}_{j,\sigma} + J \sum_j \left(\hat{\mathbf{S}}_{j+1} \cdot \hat{\mathbf{S}}_j - \frac{\hat{n}_{j+1} \hat{n}_j}{4} \right) + \hat{H}_{\text{NNN}} \right] \hat{\mathcal{P}}. \quad (2.3)$$

where \mathcal{P} is the projection operator on the subspace without double occupancy, and $\langle i, j \rangle$ is a sequence of nearest neighbouring sites. The operator $\hat{a}_{j,\sigma}^\dagger$ creates a fermion with spin σ on site j and $\hat{n}_j = \sum_\sigma \hat{a}_{j,\sigma}^\dagger \hat{a}_{j,\sigma}$ is the corresponding density operator. The spin operators are defined by $\hat{\mathbf{S}}_j = \frac{1}{2} \sum_{\sigma, \sigma'} \hat{a}_{j,\sigma}^\dagger \vec{\sigma}_{\sigma, \sigma'} \hat{a}_{j,\sigma'}$, where $\vec{\sigma}$ are the Pauli matrices. The first two terms define the $t - J$ model with tunneling of holes with amplitude t and isotropic spin-exchange interactions with coupling constant $J = 4t^2/U$. The last term describes the hole-assisted next-nearest neighbour hopping events.

In the limit of infinite strong interactions, the ground state of a Mott insulator doped with a single hole is ferromagnetic [100], as the tunneling of the hole around the lattice generates a suitable linear combination of basis states exhibiting ferromagnetism [101]. This is in stark contrast to the undoped case, where, as we saw earlier, the ground state is an antiferromagnet. An extended version of the $t - J$ is used extensively for theoretical comparisons in Chapter 5.

A special case of the $t - J$ model is in the absence of doping, when every site is occupied. Then, only the second term of \hat{H}_{t-J} is relevant and the Hamiltonian reduces to:

$$\hat{H}_{\text{Heis.}} = J \sum_{\langle i,j \rangle} \hat{\mathbf{S}}_i \cdot \hat{\mathbf{S}}_j \quad (2.4)$$

Our experimental results concerning the spin degrees of freedom in one dimension are compared to theoretical simulations of the Heisenberg model even in the presence of doping. The reason why this is valid is because the phenomenon of

spin-charge separation decouples the spin sector from the motional degrees of freedom.

2.2 Ultracold atom quantum simulator

The reason behind the success of the platform of ultracold fermions in optical lattices in simulating the physics described by the Fermi-Hubbard model is described in this section.

The advantage of using ultracold spin mixtures of fermionic atoms, as we shall see, is the controlled implementation by which interactions and doping can be tuned independently, enabling us to explore the phase diagram in Fig. 2.1.

In addition, using a quantum gas microscope enables the imaging of the many-body systems with single-site resolution, allowing a direct observation of the dynamics as well as the use of multipoint correlation functions to better characterize the system. In this section, we will see how interactions can be engineered between neutral ultracold atoms and how placing such systems in an optical lattice can be used to simulate the physics in real lattice systems.

2.2.1 Optical lattices

To produce cold atomic gases, experiments rely on using dissipative forces based on spontaneously emitted photons carrying away the energy. This is the working principle of a magneto-optical trap. However, to achieve quantum degeneracy, conservative potentials made by light that is far off-resonant are used.

The dipole moment of an atom is $\vec{p} = \alpha \vec{E}$, where \vec{E} is the electric field amplitude and α is the complex polarizability. Such a system can be modeled as an electron trapped in a dissipative, driven harmonic oscillator where the polarizability α has the form:

$$\alpha = \frac{e^2}{m} \frac{1}{\omega_0^2 - \omega^2 - i\omega\Gamma} \quad (2.5)$$

where ω_0 and ω are the natural and the drive frequencies and Γ is the coefficient of the dissipative term.

For $\omega \ll \omega_0$, the phase shift δ approaches 0 and for $\omega_0 \ll \omega$, δ approaches π . Consequently, a red-detuned trap provides an attractive potential and a blue-detuned trap provides a repulsive potential for the atoms.

To obtain an array of such dipole traps experimentally, one can simply retroreflect or use counterpropagating pairs of beams. Changing the angle and number of beams interfering can produce various geometries of optical lattices, including exotic lattices with hexagonal, dimerized or quasi-crystalline potentials [32, 102, 103]. The resultant potential produced by the off-resonant light field introduces a spatially varying ac Stark shift that the atoms experience.

In the case of two counterpropagating beams, the one dimensional optical lattice generates a potential of the form:

$$V(x) = -V_{0,x} \cos^2(x/d_x) \quad (2.6)$$

where $V_{0,x}$ is the lattice depth which is directly proportional to the intensity of the beam and d_x is the lattice spacing along the x -direction.

Superimposing pairs of counter-propagating or retro-reflected beams along different dimensions can lead to two- and three-dimensional lattices.

A convenient unit for denoting the lattice depth along directions $i = x, y, z$, which will be used throughout the thesis, is the recoil energy:

$$E_r^i = \hbar^2 / (8md_i^2) \quad (2.7)$$

The corresponding eigenstates in three dimensions can be obtained from the single-particle Hamiltonian:

$$\hat{H} = -\frac{\hbar^2}{2m} \Delta^2 + V(\vec{r}) \quad (2.8)$$

A band calculation for the x -axis gives delocalized eigenstates [104], which can be written as a product of plane waves $\Psi_{n_x, q_x}(x) = e^{iq_x x} u_{n_x, q_x}(x)$, with a band index n_x , quasimomentum q_x and a periodic function $u_{n_x, q_x}(x)$. These Bloch states can be represented using Wannier states as $w_{n,j}(\vec{r}) = \frac{1}{\sqrt{N}} \sum_q e^{-iq \cdot \vec{r}_j} u_{n, \vec{q}}(\vec{r})$ which are localized at different lattice sites \vec{r}_j and are orthogonal to each other.

In the regime where the temperature and chemical potential are small with respect to the bandgap to the next higher band, only the lowest band is occupied and the Hamiltonian reduces to:

$$\hat{H}_{\text{t.b.}} = - \sum_{\langle i, j \rangle} t_{i,j} (\hat{a}_i^\dagger \hat{a}_j + \hat{a}_j^\dagger \hat{a}_i) \quad (2.9)$$

where the indices $\langle i, j \rangle$ run over all nearest neighbouring sites, \hat{a}_i^\dagger creates a particle in the Wannier state $w_i = w_{0,i}$ and the tunneling coefficient $t_{i,j} = \int d\vec{r}^3 w_i(\vec{r}) \hat{H} w_j(\vec{r})$, where \hat{H} is taken from Eq. 2.8.

So far we have seen how to obtain the kinetic term as described by the Fermi-Hubbard model. To fully simulate Fermi-Hubbard systems, we also need to have control over the interaction between spinful fermions.

We make use of the fact that when the atomic gas is cooled to a low enough temperature, only s-wave scattering is relevant [105] and the interactions between fermions can be described by an on-site potential:

$$V_{\text{int}}(\vec{r}_1, \vec{r}_2) = \frac{\pi \hbar^2 a_s}{m} \delta(\vec{r}_1 - \vec{r}_2) \quad (2.10)$$

where a_s is the s-wave scattering length.

Due to their fermionic nature and the suppression of p -wave scattering at low energies, atoms in the same spin states cannot scatter and therefore do not interact. However, atoms in different spin states can be made to interact via s -wave collisions and the nature of the interaction can be tuned by addressing a Feshbach resonance

using magnetic fields [106].

In the lowest band of an optical lattice, the Hamiltonian describing the s-wave interaction (Eq. 2.10) has the form:

$$\hat{H}_{\text{int}} = U \sum_i \hat{n}_{i,\uparrow} \hat{n}_{i,\downarrow} \quad (2.11)$$

The interaction strength U has the form $U = (4\pi\hbar^2 a_s / m) \int d\vec{r}^3 |w(\vec{r})|^4$ where $w(\vec{r})$ is the Wannier function.

Thus, by cooling the atomic gas to low temperatures and loading it into an optical lattice leading to systems with processes described by Eq. 2.9 and Eq. 2.11, we can generate ideal platforms to simulate the Fermi-Hubbard model (Eq. 2.1)

2.3 Doping one-dimensional antiferromagnets

The physics of materials in one and two dimension can be vastly different, even if the underlying model is the same. In one dimension, the spin and charge degrees of freedom are decoupled, leading to the phenomena of incommensurate magnetism and spin-charge separation, as we shall see in this section. As a consequence, the free Landau quasiparticles that describe the system in higher dimensions are no longer sufficient to describe such systems. Instead, the description is replaced by collective excitations.

The low-energy physics of 1D many-body systems are described generically by Luttinger liquid theory, where the emerging excitations are collective waves possessing a simple linear dispersion. In order for a fermion to move in a 1D lattice, it has to move all other identical fermions as they cannot pass through one another, leading to collective excitations.

An interpretation can also be made in momentum space, where the collective excitations can be understood by a linearization of the dispersion relation around the two Fermi points. Every excitation $k \rightarrow k + q$ has an energy $E = u\hbar q$, where u is the group velocity at the Fermi point. As the energy depends only on the group velocity, all excitations with a fixed q have the same energy. Consequently, any interaction couples them and the eigenmodes are excitations with momenta q , with all particles close to a Fermi point sharing this collective excitation.

The excitations are analogous to sound waves propagating with a velocity u , which for noninteracting fermions, is related to the Fermi velocity v_F [107]. A complete description of the asymptotic properties of a Luttinger liquid is provided by the velocity u and the Luttinger parameter K , which is a dimensionless number which controls the decay of all correlation functions and thermodynamic quantities.

In condensed matter experiments, properties of Luttinger liquids have been studied using neutron scattering on weakly coupled quasi-1D spin-1/2 chains [108, 109] and ladder systems [110] and using conductance measurements and scanning tunnelling microscopy on carbon nanotubes [111, 112].

In the experiments, we prepare chains of fermions in the lowest energy band of Hubbard Hamiltonian, which is in turn a minimalistic approximation of the Luttinger liquid theory.

The unprecedented level of control afforded by ultracold atoms in optical lattices means that one can tune the interactions by simply varying external magnetic fields which effectively changes the scattering length, and one can also independently tune the amount of doping by raising or lowering the chemical potential by loading more or fewer atoms into the lattice.

2.3.1 Incommensurate magnetism

Incommensurate magnetism, or incommensurate spin correlations are expected to be present in doped or polarized one dimensional Fermi-Hubbard chains. Doping can be achieved by moving away from half filling and polarization by having a spin-imbalance in the chain.

In such systems, Luttinger liquid theory predicts the presence of an algebraically decaying incommensurate correlations at zero temperature, whose wave vector varied linearly with the amount of doping [75, 113]. In the case of density doping, incommensurate spin-density waves are expected and in the case of excess spin doping, incommensurate spin correlations are expected.

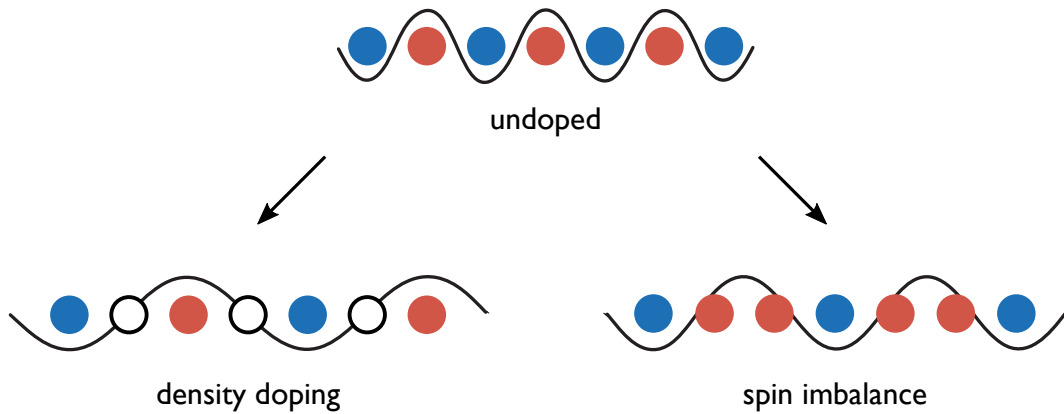


FIGURE 2.2: **Incommensurate magnetism** In an undoped Fermi-Hubbard chain with antiferromagnetic correlations as described by the Heisenberg model ($n = 1, m = 0$), the sign of the spin flips with every single lattice site and is commensurate with the number of lattice sites. However, on introducing either density doping ($n \neq 1$) or excess spin doping ($m \neq 0$), the periodicity of the sign flips of the spin increases by an amount related to the level of doping, and becomes incommensurate with the number of lattice sites in the chain.

Consider an undoped Fermi-Hubbard chain with antiferromagnetic spin correlations. Here the mean occupation density in the chain $n = 1$, and the net magnetization $m = 0$. In such chains, the spin correlations decays with distance, and more importantly, it flips sign with every lattice site. The dependence of the spin correlations on distance has the following form:

$$\langle \hat{S}_i^z \hat{S}_{i+x}^z \rangle \approx A_1 e^{-x/\xi_1} \cos(\pi x) \quad (2.12)$$

What Luttinger liquid theory predicts is that when density doping is introduced into these chains, the wave vector changes linearly with the amount of doping n and the dependence of the spin correlations on distance now has the form:

$$\langle \hat{S}_i^z \hat{S}_{i+x}^z \rangle \approx A_2 e^{-x/\xi_2} \cos(\pi n x) \quad (2.13)$$

Similarly, when excess spin of one kind are present in the system, leading to a net magnetization of m , the dependence of the spin correlations has the form:

$$\langle \hat{S}_i^z \hat{S}_{i+x}^z \rangle \approx A_3 e^{-x/\xi_3} \cos(\pi(1+2m)x) \quad (2.14)$$

By using a quantum gas microscope with both spin and density resolution, we can directly extract properties such as the mean density per chain n and the net magnetization m . Then, we can simply compute the dependence of spin correlations on distance in real space and in this way, observe the phenomenon of incommensurate magnetism (see Fig. 2.2). Chapter 4 is dedicated to the results we obtained in this project.

2.3.2 Spin-charge separation

In systems where individual constituents are replaced by collective excitations, these excitations can behave as independent entities that can propagate at different velocities and be spatially unbound from one another. Such a spatial separation in systems with collective spin and charge excitations, is called spin-charge separation. Additionally, at low temperatures, the spin and charge excitations can carry the exact quantum numbers of spin $1/2$ and charge e respectively, a phenomenon called fractionalization [107].

An excellent summary of the theoretical framework behind spin-charge separation is provided in [75, 114]. Here, we will go through only the key steps involved in understanding the decoupling of the spin and charge sectors starting from the Hubbard Hamiltonian given by 2.1.

In a 1D lattice system of N particles, the particle density operator is:

$$n(x) = \sum_{k=1}^N \delta(x - x_k) \quad (2.15)$$

where x_k is the position operator of the k th particle. It is convenient to rewrite Eq. 2.15 in terms of a labelling field $\Phi(x)$ [115], which is a continuous function of the position, having a value of $\Phi(x_k) = 2\pi k$ at site k .

Using the rule for transforming δ functions

$$\delta(f(x)) = \sum_{\text{zeros of } f} \frac{1}{|f'(x_k)|} \delta(x - x_k) \quad (2.16)$$

the density $n(x)$ can be rewritten in terms of $\Phi(x)$ as follows:

$$n(x) = \sum_k \delta(x - x_k) = \sum_n |\nabla \Phi(x)| \delta(\Phi(x) - 2\pi m) \quad (2.17)$$

where m is an integer. Using the Poisson summation identity $\sum_p e^{ipx} = 2\pi \sum_k \delta(x - 2\pi k)$ where p is an integer, Eq. 2.17 reduces to:

$$n(x) = \frac{\nabla\Phi(x)}{2\pi} \sum_p e^{ip\Phi(x)} \quad (2.18)$$

We can further introduce a field ϕ to express the particle positions with respect to their rest positions $x_k^0 = n_0 k$ on the lattice, defined as:

$$2\phi(x) = 2\pi n_0 x - \Phi(x) \quad (2.19)$$

where $n_0 = N/L$ is the mean density.

Eq. 2.18 then reduces to:

$$n(x) = \left(n_0 - \frac{\nabla\phi(x)}{\pi}\right) \sum_p e^{2ip(\pi n_0 x - \phi(x))} \quad (2.20)$$

The density operator $n(x)$ can also be expressed as a product of the bosonic or fermionic field operators $n(x) = \psi^\dagger(x)\psi(x)$. Using an amplitude-phase ansatz for the field operators $\psi^\dagger(x) = \sqrt{n(x)}e^{-i\theta(x)}$ where $\theta(x)$ is a second field, the commutation rule obeyed by the field operators $[\psi(x), \psi^\dagger(x')] = \delta(x - x')$ can be rewritten as $[\phi(x), \nabla\theta(x')/\pi] = i\delta(x - x')$, which is a commutation relation between a field ($\phi(x)$) and its canonical momentum ($\Pi(x) = \nabla\theta(x)/\pi$).

The bosonic and fermionic field creation operators have the form:

$$\psi_B^\dagger(x) = \sqrt{n_0 - \nabla\phi(x)/\pi} \sum_p e^{i2p(\pi n_0 x - \phi(x))} e^{-i\theta(x)} \quad (2.21)$$

$$\psi_F^\dagger(x) = \sqrt{n_0 - \nabla\phi(x)/\pi} \sum_p e^{i(2p+1)(\pi n_0 x - \phi(x))} e^{-i\theta(x)} \quad (2.22)$$

Through this process, called bosonization, the Hamiltonian can be expressed in terms of fields following bosonic commutator relations regardless of their original statistics. The expression for the density and creation operators from Eqs. 2.20, 2.21 and 2.22 can be substituted into the Fermi-Hubbard Hamiltonian from Eq. 2.1.

In the low-energy limit (i.e, including only the $p = 0$ term), corresponding to slowly varying fields, the kinetic energy term takes the form $\int dx \nabla\psi^\dagger \nabla\psi \rightarrow \int dx n_0 (\nabla\theta)^2$ and the interaction term takes the form $\int dx n(x)^2 \rightarrow \int (\nabla\phi(x))^2$.

In this low-energy limit, the Fermi-Hubbard Hamiltonian can thus be expressed as:

$$H = \frac{1}{2\pi} \int dx \left[vK(\pi\Pi(x))^2 + \frac{v}{K}(\nabla\phi(x))^2 \right] \quad (2.23)$$

The Hamiltonian depends on only two parameters - K and v , respectively the Luttinger liquid parameter and velocity, and together they provide a total characterization of the low-energy physics of 1D systems.

To include the spin component into the above formalism, the process of bosonization is repeated and separate bosonic fields $\phi_{\uparrow,\downarrow}$ are used for each component. The

Hamiltonian from Eq. 2.23 now contains terms of the form $\int dx n_{\uparrow}(x)n_{\downarrow}(x)$. On introducing fields $\phi_{\rho} = (\phi_{\uparrow} + \phi_{\downarrow})/\sqrt{2}$ and $\phi_{\sigma} = (\phi_{\uparrow} - \phi_{\downarrow})/\sqrt{2}$ to encode the charge and spin density respectively, the decoupling of the spin and charge sectors becomes apparent.

The result is the presence of two independent Hamiltonians:

$$H_{\nu} = \frac{1}{2\pi} \int dx \left[v_{\nu} K_{\nu} (\pi \Pi(x))^2 + \frac{v_{\nu}}{K_{\nu}} (\nabla \phi_{\nu}(x))^2 \right] \quad (2.24)$$

with $\nu = \rho, \sigma$ describing the decoupled spin and charge excitations, each characterized by a velocity v_{ν} and Luttinger liquid parameter K_{ν} . The excitations corresponding to $\nu = \rho, \sigma$ are called holons and spinons respectively.

A consequence of the presence of two independent Hamiltonians describing the charge (holons) and spin (spinons) sectors in 1D systems is that single particle fermionic excitations (excitations carrying both spin and charge) do not exist. Instead the spin and charge excitations can move with different velocities given by v_{σ} and v_{ρ} respectively.

2.3.3 Beyond the Luttinger liquid regime

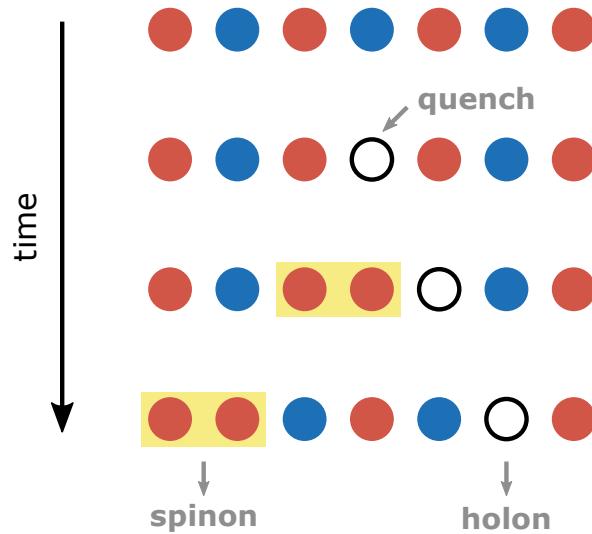


FIGURE 2.3: **Cartoon of the experimental protocol used to probe spin-charge separation, shown here in the absence of thermal fluctuations.** Starting from a one dimensional Heisenberg chain with antiferromagnetic correlations, a local quench is performed to remove a single fermion, essentially causing a change in charge of $(\Delta\text{Charge}) = 1$ and a change in spin of $(\Delta\text{Spin}) = 1/2$ in the chain. Spin-charge separation implies the emergence of two excitation branches, one carrying the excess $(\Delta\text{Charge}) = 1$ called the holon and the other carrying the excess $(\Delta\text{Spin}) = 1/2$ called the spinon. Since these two excitations are independent of each other, they can move with different velocities and be arbitrarily separated from one another in the chain, with no binding between them at any distance of separation.

In our experiment, we probe spin-charge separation by implementing a local quench addressing a single site of the 1D lattice and resonantly removing a single fermion (see Fig. 2.3). After the quench, we wait for variable time of evolution and use our spin and density resolution to independently track the dynamics of spinons and holons.

Such a local quench, which is a delta function in real space, gives rise to spin and charge excitations with a wide range of momenta, and places our experiments beyond the low-energy limit described by the Luttinger liquid theory.

In the limit of infinitely large repulsive interactions ($U \rightarrow \infty$) and zero temperature, Ogata, Shiba and Woynarovich [116, 117] showed that the ground state wavefunction of the doped Fermi-Hubbard model in 1D factorizes exactly into independent spin and charge sectors:

$$\Psi(\{x_{j,v}\}) = \Psi_\rho(\{x_j\})\Psi_\sigma(\{\tilde{x}_{j,v}\}) \quad (2.25)$$

Here, the charge sector of the wavefunction Ψ_ρ describes non-interacting fermions and the spin sector of the wavefunction Ψ_σ describes the ground state of the Heisenberg model for the sites that are occupied. For sufficiently large U , a similar factorization of the spin and charge sectors is expected even at $T \geq 0$, due to the difference in the spin-exchange and tunneling energy scales, $J \ll t$, indicating the validity of spin-charge separation even beyond the low-energy limit.

We will start with the 1D $t - J$ model (Eq. 2.3) and derive expressions for the charge and spin dispersion relations in order to understand the velocities expected in the case of a Luttinger liquid and contrast it with what we realize in our experiment.

To describe the charge degrees of freedom in the 1D $t - J$ model, one can introduce spin-less hole operators \hat{h}_i^\dagger which creates a hole at site i by displacing a spin in real space from site i . The displacement of the spin is performed by describing the spins in terms of Schwinger bosons.

The $t - J$ model can be rewritten in terms of spin operators acting on occupied sites and in terms of hole operators as follows [99]:

$$\begin{aligned} \hat{H}_{t-J} = & t \sum_{\langle i,j \rangle} \left(\hat{h}_i^\dagger \hat{h}_j \hat{\mathcal{F}}_{ij}^\dagger + h.c. \right) + J \sum_{i,j} \left(1 - \hat{n}_i^h \right) \hat{S}_i \cdot \hat{S}_j \left(1 - \hat{n}_j^h \right) \\ & - \frac{J}{4} \sum_{\langle i,j \rangle} \hat{n}_i^h \hat{n}_j^h + \frac{J}{4} \sum_{\langle i,j,k \rangle} \hat{h}_k^\dagger \left(1 - \hat{n}_i^h \right) \hat{h}_i \hat{\mathcal{A}}_{ij}^\dagger \hat{\mathcal{A}}_{kj} \end{aligned} \quad (2.26)$$

where $\hat{n}_i^h = \hat{h}_i^\dagger \hat{h}_i$ is the hole density, \hat{S}_i is the spin operator at site i and the operators $\hat{\mathcal{F}}_{ij}$ and $\hat{\mathcal{A}}_{ij}$ can be expressed in terms of Schwinger bosons [99].

The first term describes the tunneling of holes between two sites, by displacing spins. The displacement of the spins is given by $\hat{\mathcal{F}}_{ij}$ and in the space of occupied sites (called the ‘‘squeezed space’’), the ordering of the spins is unchanged leading to $\hat{\mathcal{F}}_{ij} = 1$.

The second term describes the spin exchange interactions. Two neighbouring spins in squeezed space can interact only if they are not separated by holes in real space and consequently, with increasing density, a reduction in the spin-exchange energy scale J is expected.

The third term describes an attraction between holes. In the limit of $t \gg J$, the contributions of this term becomes negligible compared to the first term of Eq. 2.26. The last term describes the next-nearest neighbour tunneling of a hole which is accompanied by a flipping in sign of the spin on the site between the starting and finishing sites of the hole. This term, which is a second order process in t , is significantly weaker than the first term of Eq. 2.26 in the limit $t \gg J$.

The dispersion relation for the charge sector can be obtained from an effective Hamiltonian for the holes from Eq. 2.26. In the limit of $U/t \gg 1$ and $t \gg J$, the only relevant term of the Hamiltonian is the tunneling term:

$$\hat{H}_{\text{ch}} = t \sum_{\langle i,j \rangle} (\hat{h}_i^\dagger \hat{h}_j + h.c.) = 2t \sum_k \cos(k) \hat{h}_k^\dagger \hat{h}_k \quad (2.27)$$

which is obtained by neglecting terms of order $O(J/t)$. The corresponding dispersion relation is:

$$\hat{\epsilon}_{\text{ch}}(k) = 2t \cos k \quad (2.28)$$

where k is the momentum of the charge wave. This is identical to the dispersion relation of free fermions in a 1D lattice.

To obtain the dispersion relation for the spin sector, the charge sector is traced out from \hat{H}_{t-J} in Eq. 2.26, i.e., $\hat{H}_s = \text{tr}_{\text{ch}}(\hat{\rho}_{\text{ch}} \hat{H}_{t-J})$. The resultant Hamiltonian for the spin sector has the form:

$$\hat{H}_s = J_{\text{eff}}(n) \sum_{\langle \tilde{i}, \tilde{j} \rangle} \hat{S}_{\tilde{i}} \cdot \hat{S}_{\tilde{j}} \quad (2.29)$$

where \sim denotes sites in squeezed space.

From Eq. 2.29, we can see that the dispersion of the spin is proportional to the density-dependent spin exchange coupling, i.e., $\hat{\epsilon}_s \propto J_{\text{eff}}(n)$. To obtain the exact nature of the density dependence of the J_{eff} , we need to understand how the nearest neighbour spin exchange amplitude and the spin exchange interaction arising from the next-nearest neighbour tunneling given by the second and fourth term of Eq. 2.26 respectively, vary with density.

For every spin on a site i in real space and a corresponding site \tilde{i} in squeezed space, it interacts with its neighbouring spin at site $\tilde{i} + 1$ in squeezed space only if there is a spin on site $i + 1$ in real space. This leads to a nearest-neighbour contribution $J_{\text{eff}}^{(1)}$ to the spin exchange amplitude J_{eff} in squeezed space given by:

$$J_{\text{eff}}^{(1)} = J \frac{\langle (1 - \hat{n}_i^h) (1 - \hat{n}_{i+1}^h) \rangle}{\langle (1 - \hat{n}_i^h) \rangle} \quad (2.30)$$

Similarly, the contributions from the next-nearest neighbouring tunneling process is given by:

$$J_{\text{eff}}^{(2)} = \frac{J}{2} \frac{\langle (1 - \hat{n}_i^h) (\hat{h}_{i-1}^\dagger \hat{h}_i + \hat{h}_i^\dagger \hat{h}_{i-1}) \rangle}{\langle (1 - \hat{n}_i^h) \rangle} \quad (2.31)$$

Assuming a Fermi-Dirac distribution function $n_k^F(n, T)$ for the holes with density $n_h = 1 - n$ and having temperature T , we can make use of Wick's theorem to obtain:

$$J_{\text{eff}}(n, T) = Jn \left[1 + \frac{1}{\pi n} \int_0^\pi dk \cos(2k) n_k^F(n, T) \right] \quad (2.32)$$

At zero temperature, the integral can be evaluated exactly to obtain:

$$J_{\text{eff}}(n, T = 0) = Jn \left[1 - \frac{\sin(2\pi n)}{2\pi n} \right] \quad (2.33)$$

Eq. 2.33 is in agreement with results from exact Bethe-ansatz calculations for the 1D Fermi-Hubbard model. The effective Hamiltonian for the spin sector from Eq. 2.29 thus has the form:

$$\hat{H}_s = Jn \left[1 - \frac{\sin(2\pi n)}{2\pi n} \right] \sum_{\langle \vec{i}, \vec{j} \rangle} \hat{S}_{\vec{i}} \cdot \hat{S}_{\vec{j}} \quad (2.34)$$

The corresponding dispersion relation for the spin wave has the form [118]:

$$\begin{aligned} \hat{\epsilon}_s(k) &= \frac{\pi}{2} J_{\text{eff}} |\sin(k_{\text{eff}})| \\ &= \frac{\pi}{2} Jn \left[1 - \frac{\sin(2\pi n)}{2\pi n} \right] |\sin(k/n)| \end{aligned} \quad (2.35)$$

where $k_{\text{eff}} = k/n$ is the density dependent momentum of the spin wave.

The dispersion relations for the charge and the spin sectors corresponding to the expressions in Eq. 2.28 and Eq. 2.35 respectively are shown in Fig. 2.4. In the Luttinger liquid regime, which concerns only low energy excitations, the velocities of the spin and charge excitations can be obtained by linearizing around the Fermi level.

In the dispersion relation for the charge excitations, it can be seen that in the half-filling Mott insulating case, the velocity of the excitation is zero, as expected. When the chain is slightly doped, the Fermi level drops and linearizing around the dispersion yields a velocity of the excitation that is slow. This velocity, given by $d\epsilon/dk$ and indicated by the red bar in Fig. 2.4, is expected in the Luttinger liquid regime close to half filling. As the hole doping is increased further, the Fermi level drops too and the velocity increases until it attains the maximum group velocity $v_t^{\text{max}} = 4\pi t a_x / h$ where t is the tunneling amplitude and a_x is the lattice spacing in the 1D chain. Doping further beyond this point decreases the slope again and the velocity of the charge excitation decreases towards zero for zero doping. This trend intuitively makes sense because when the number of particles is very small, the system is close to the bottom of a band (or top, in case of a full band).

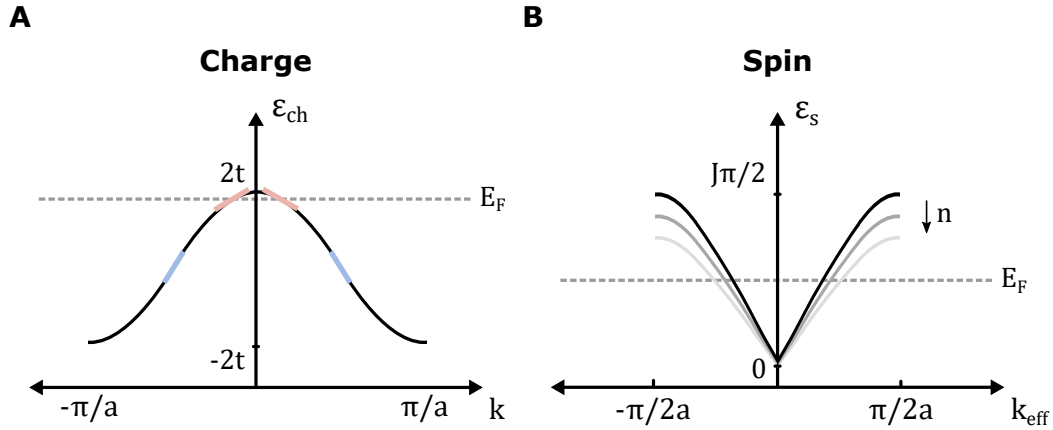


FIGURE 2.4: **Dispersion relations of charge and spin excitation within and beyond the Luttinger liquid regime.** **A**, The charge excitation dispersion relation as obtained from Eq. 2.28 shows the possible charge momentum modes that could be produced. Close to half-filling, the Fermi level (E_F , grey dashed line) intersects the dispersion relation slightly below its peak. The velocity of the charge excitation in the Luttinger liquid regime is given by linearizing around the Fermi level and corresponds to the slope of the red bar. However, in the case of a local quench which excites the entire spectrum, the fastest excited momentum mode corresponds to the one with the largest slope (blue bar). **B**, The spin excitation dispersion relation as obtained from Eq. 2.35 shows the possible spin momentum modes that could be produced. The fastest velocities of the spin excitation occur close to half-filling, where the slope of the dispersion is maximum (black curve). As the density is decreased, the slope and the velocity decreases as well (grey curves). The Fermi level (E_F , grey dashed line) corresponds to an unmagnetized chain, i.e., there are equal number of up and down spins. Following the local single fermion removing quench in the experiment, the fastest excited spin mode is the one that is close to half-filling.

In the dispersion relation for the spin excitations, at half filling (indicated by the black curve in Fig. 2.4), the slope of the dispersion is maximum, yielding a maximum group velocity of $v_j^{\max} = \pi^2 J a_x / h$, where $J = 4t^2 / U$ is the spin exchange amplitude and a_x is the lattice spacing. As hole doping is increased in the chain, the slope decreases and consequently the velocity of the spin excitations decrease. It should be noted that spin-charge separation implies that the spin sector is described simply by the Heisenberg model and the dispersion relation in Fig. 2.4 is shown in squeezed space coordinates.

The dependence of the charge and spin excitation velocities on density and interaction strength is discussed in more detail in Fig. 7.2 of [75]

As we saw in the discussion of Fig. 2.3, in our realization of the experiment, the spin and charge excitations emerge from a quench that is local in real space, leading to excitations carrying a wide range of momentum modes. However, when we track the wavefronts of these excitations with a microscope, we are essentially tracking the dynamics of the fastest momenta modes. In Fig. 2.4, the fastest modes for the charge excitation following our quench correspond to the ones with the highest slope, which is indicated by the blue bars. In the case of the spinon, the velocity is close to the maximum velocity predicted in the Luttinger liquid regime.

It is important to note that the velocities of these spin and charge modes are not necessarily the same as the velocities corresponding to a linearization around the Fermi level, but rather the maximum group velocities v_i^{\max} and v_j^{\max} , indicating that we are no longer in the Luttinger liquid regime. This places our experiments in a unique regime where it can probe the physics beyond the predictions of Luttinger liquid theory, which concerns only with low energy excitations.

Within the length- and time-scales probed in the experiment, the dispersion is found to be linear and no signatures of a binding between the spin and charge excitations are seen. The fact that we can observe spatial separation of the excitations in our experiment means that the spin-charge factorization predicted by Eq. 2.25 at $U \rightarrow \infty$ is also valid in our experimentally realized chains at $U/t = 15$. These results are described in detail in Chapter 5.

2.4 Doping two-dimensional antiferromagnets

In one dimension, the presence of spin-charge separation inhibits the interplay between the spin and charge degrees of freedom, leading to independent excitations. However, in a two dimensional system of interacting fermions, entirely new quasiparticles emerge [119–124].

The study of such systems is of great importance because the dynamics of the emergent quasiparticles in 2D are at the heart of an understanding of the phase diagram of cuprates as shown in Fig. 2.1. The fundamental building block of the phases shown is a single dopant in a 2D antiferromagnet.

This section provides a qualitative understanding of the interplay between spin and charge in 2D at the level of a single dopant.

The simplicity of changing the dimensionality from one to two in our ultracold atom quantum simulator deserves to be emphasized - by simply tuning the laser powers of the x - and y - lattice beams, the tunneling along x - and y -axes can be

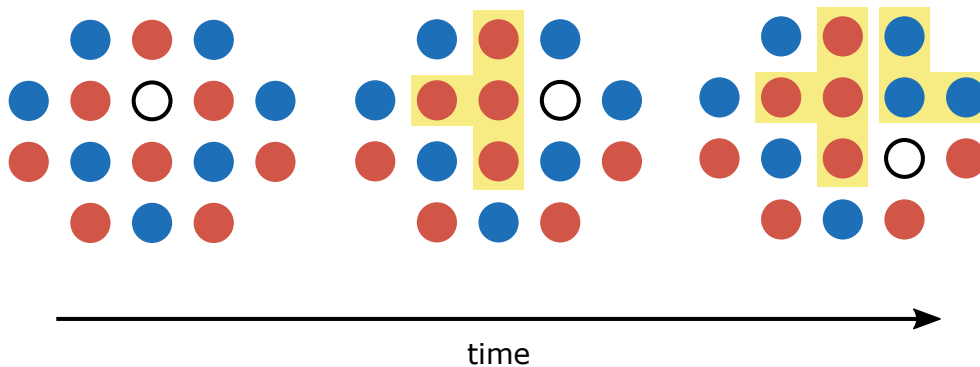


FIGURE 2.5: **Cartoon illustrating the dynamics of a single dopant in a 2D antiferromagnet.** Whereas in one dimension, the competition between the spin and charge sectors is absent, this is not the case in two dimensions. The dopant, which moves to lose kinetic energy, creates ferromagnetic bonds (indicated in yellow) in an otherwise antiferromagnetic lattice. The further the dopant moves, the greater the cost in this “magnetic energy”.

matched, generating a two dimensional Fermi-Hubbard system. In fact, this also enables us to smoothly explore the crossover from one to two dimensions.

In the limit of strong interaction ($U/t \gg 1$) and $t \gg J$, when a 2D Fermi-Hubbard antiferromagnet is doped with a single dopant (see Fig. 2.4), the dopant wants to delocalize at a rate allowed by the tunneling timescale t by virtue of its kinetic energy. However, each hopping event of the dopant creates a ferromagnetic bond in an otherwise antiferromagnetic bond [125, 126], costing an energy of J and leading to an interplay of the spin and charge dynamics. The further the dopant moves, the longer is the string of flipped spins it leaves behind [124, 127], thereby increasing the magnetic cost associated with the ferromagnetic bonds.

One possible result is a global homogeneous reduction of the antiferromagnetic correlations in the system as the dopant explores the system, distorting the spins. An alternative is that the dopant gets dressed by the spin distortions and it has to carry the distorted spin cloud with it as with moves, thereby moving at a velocity given by the spin exchange timescales.

Our experiments reveal that the reduction in antiferromagnetic correlations - the distorted spin cloud - is not spread homogeneously throughout the system, but rather has a radius of around 1 site from the position of the dopant. The magnetic polaron is nothing but the quasiparticle comprising of the dopant and the spin cloud which dresses it.

The experimental results demonstrating the interplay between the spin and charge degrees of freedom in the crossover from one to two dimensions and in fully 2D systems are presented in Chapter 6.

2.5 Experimental limitations

The study of many-body systems has always been challenging due to the complexity that emerges when individual elements lose their character and start behaving in a collective manner. In one dimension, as is the case for incommensurate magnetism and spin-charge separation, the emerging degrees of freedom - independent charge and spin modes - differ fundamentally from that of a single electron. In two dimensions, dopants gets dressed by a spin cloud and the resulting physics is significantly different from that of a single electron in a lattice.

In traditional condensed matter experiments, the signatures of many-body phenomena has relied on scattering experiments which study macroscopic observables. While such experiments have certainly lead to many breakthroughs, they suffer from limitations such as the range of materials that can be produced in a lab and the interpretation of the experimental signatures.

Although the platform of quantum gas microscopy offers the potential to prepare clean samples and access microscopic observables, it comes with its own limitations. The lowest temperatures realized in quantum simulators currently correspond to a several hundred Kelvin in real materials. To probe the Fermi-Hubbard phase diagram at the low temperatures achieved in cuprates is still beyond the reach of experiments today. Another limitation is the system size - traditional condensed matter experiments deal with samples that contain several orders of magnitude larger that the number of particles than in quantum gas microscope experiments. Several insights can be obtained with systems of less than a hundred particles, but anything beyond that is out of reach. The limiting factor for system size are the harmonic confinement of optical beams and the highest absolute output powers of lasers available today. However, several new schemes are emerging in the cold atom community to deal with these limitations and it will certainly be interesting to see how they pan out.

Nevertheless, with our quantum gas microscope, we were able to prepare Fermi-Hubbard systems in one and two dimensions, directly probe microscopic observables such as spatial spin correlations in the presence of dopants, and provide insight into phenomena such as incommensurate magnetism, spin-charge separation and formation of magnetic polarons.

These results are described in the following chapters, starting with an overview of our quantum gas microscope.

Chapter 3

A Fermi gas microscope

In this chapter, the essential components of our quantum gas microscope that enable the realization of the experiments described in the following chapters are described. In particular, the preparation of a degenerate Fermi gases, its loading into an optical lattice and the site-resolved spin and density imaging process will be summarised here. A more detailed description of the experimental setup is available in the thesis of A. Omran [128] and M. Boll [129].

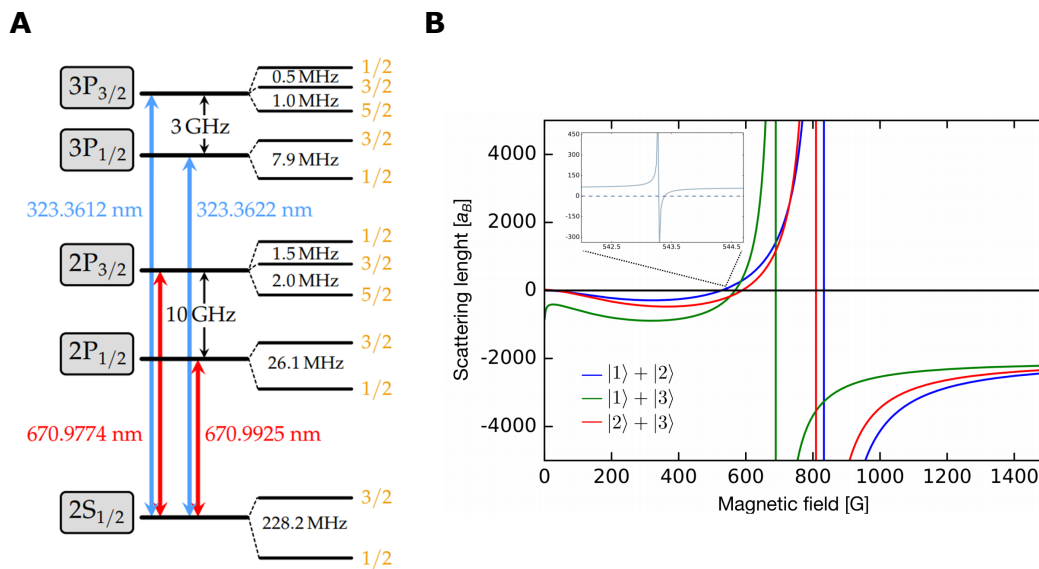


FIGURE 3.1: **A**, Energy levels and transitions in ${}^6\text{Li}$. The relevant fine and hyperfine levels of ${}^6\text{Li}$ are shown. The lowest three hyperfine states $|F = 1/2, m_F = \mp 1/2\rangle$ and $|F = 3/2, m_F = -3/2\rangle$ are denoted by $|1\rangle$, $|2\rangle$ and $|3\rangle$ respectively. **B**, Feshbach resonances for spin mixtures of lowest energy states. All three mixtures provide a broad Feshbach resonance. Figure taken from [128, 129].

3.1 Properties of Lithium

Each experimental sequence requires starting with a heated gas of ${}^6\text{Li}$ and cooling it down to degeneracy to prepare our ultracold spin-balanced samples. This section introduces the atom of our choice - ${}^6\text{Li}$, and briefly describes the various processes involved in the preparation of our ultracold 2D Fermi gases.

The choice of using ${}^6\text{Li}$ stems from the fact that it has a light mass which allows for fast tunneling and consequently, superexchange timescales. Its light mass also allows the use of larger lattice constants than one would with the other commonly used element in Fermi gas experiments, ${}^{40}\text{K}$. The larger spacing is particularly advantageous for resolving single sites in the optical lattice. The level structure of ${}^6\text{Li}$ is shown in Fig. 3.1.

The lowest hyperfine levels $|F = 1/2, m_F = \mp 1/2\rangle$, separated by an energy splitting of 228.2 MHz, denoted by $|1\rangle$ and $|2\rangle$, are respectively the two spin states that we will consider throughout the thesis. The principal D_1 and D_2 transitions from the $2S_{1/2}$ to the $2P_{1/2}$ and the $2P_{3/2}$ states at 671 nm as well as the transitions from the $2S_{1/2}$ to the $3P_{3/2}$ states at 323 nm will be used in the various stages of our experiment, as we will see later in the next section.

${}^6\text{Li}$ also has a broad Feshbach resonance at 832 G with a width of around 300 G (see Fig. 3.1), which allows for easily tunability of interactions of the atoms. Additionally, at a field of 320 G, the scattering length of the $|1\rangle$ and $|2\rangle$ states has a local minimum of $-290a_B$, providing a high scattering rate for efficient evaporative cooling.

3.2 Preparation of degenerate Fermi gases

The experimental sequence used to produce degenerate 2D Fermi gases ready to be loaded into optical square lattices can be summarized as follows:

MOT chamber

The hot gas of ${}^6\text{Li}$ atoms emerging from a heated block of lithium atoms is first decelerated by a Zeeman slower. The Zeeman slower is collimated beam at $\sim 100\text{mW}$ and is 100 MHz red detuned from the cooling transition.

On entering the chamber, the atoms are captured in a MOT at the 671 nm D_2 line. The repumper and the cooler are detuned by $\sim 8\Gamma_{2P}$ with respect to their respective transitions. After 5s of this “red” MOT, we have around 10^8 atoms at 1mK temperature.

The red MOT is followed by a compressed MOT to increase the phase-space density and obtain a lower temperature of the gas. The gradient field and the MOT beam intensities are ramped down in 10ms (see Fig. 3.2), and the detuning is roughly Γ_{2P} . The resulting phase-space density is $n_0\lambda_T^3 \sim 2.1 \times 10^{-6}$, where n_0 is the peak density and $\lambda_T = h/\sqrt{2\pi mk_B T}$ is the thermal de Broglie wavelength. The temperature of the cloud is $\sim 300\mu\text{K}$.

We further cool the gas with a UV-MOT on the narrow $2S_{1/2}$ to $3P_{3/2}$ transition at 323 nm. The UV cooling stage is also relatively quick, lasting less than 15ms. In this time, the frequencies, initially with a detuning of a few linewidths, are ramped closer to resonance. The power of the beams and the gradient are also adjusted (see Fig. 3.2) to optimize loading into the dipole trap, which is discussed in the next paragraph. After the UV-MOT which retains $\approx 30\%$ of the atoms from the red MOT, the cloud is cold enough ($\sim 60\mu\text{K}$) to be loaded directly into an optical dipole trap of 60 W at 1070 nm.

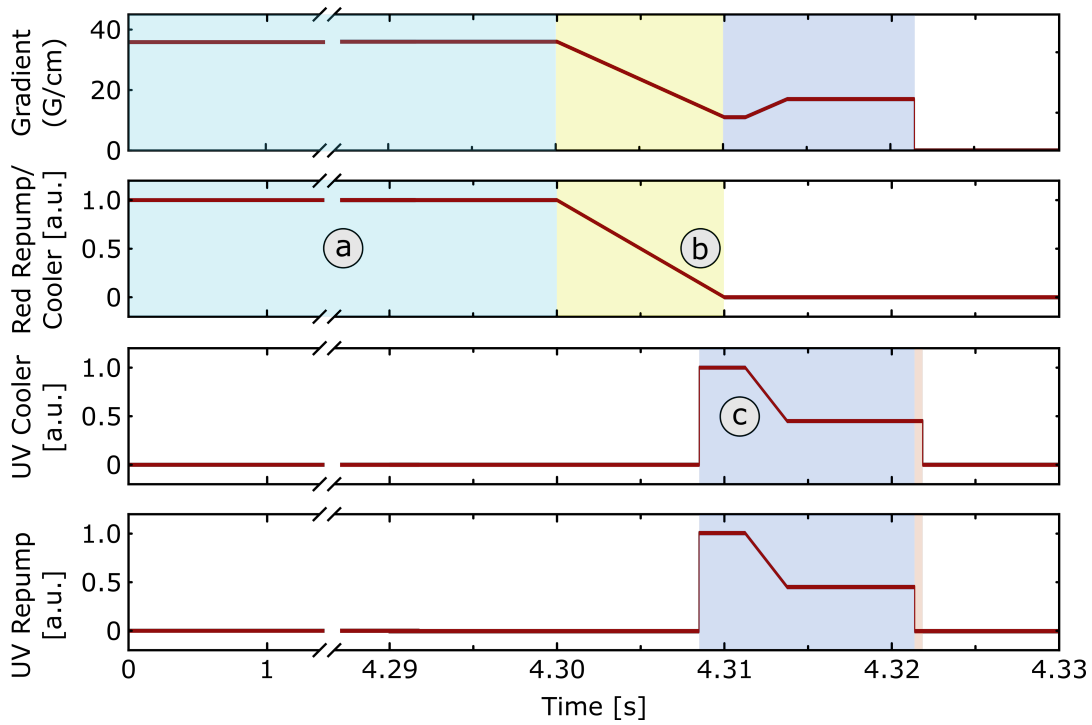


FIGURE 3.2: **Timeline of the MOT.** The sequence of a selected few optical beams used in the generation of our MOT is shown. **a**, The red MOT with six 671nm beams on for around 4s traps 10^8 atoms at 1mK. **b**, The compressed MOT obtained by reducing the gradient and the MOT beams and changing their detuning (see text) lasts 10ms. **c**, The final MOT stage is performed with 323nm UV-MOT beams. It lasts 13ms and the ramps are optimized to load efficiently into an optical dipole trap (see text). At the end of the UV-MOT stage, the repumper is switched off before the cooler and the atoms are optically pumped into a $|1\rangle - |2\rangle$ mixture (red shade).

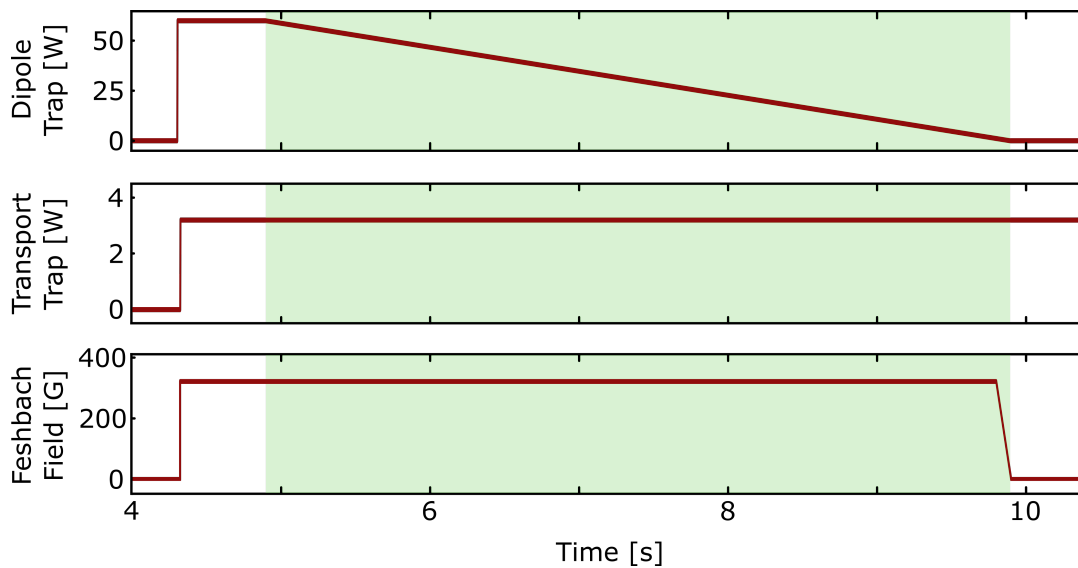


FIGURE 3.3: **Timeline of the cooling before optical transport.** The first stage of evaporative cooling is performed in the MOT chamber to efficiently load atoms from the UV-MOT into the transport trap. The optical dipole trap is ramped down from ~ 60 W to zero in 5s at a homogeneous field of 330G.

Optical transport

A “transport” beam of 3 W at 1064 nm is used to transfer the atoms from the MOT chamber to a glass cell “science” chamber where the rest of the experiment takes place. To transfer efficiently into this beam which is focused to a narrow waist of 28 μm , the atoms from the UV-MOT are first transferred into an optical dipole trap at 1070 nm.

Then gas is then evaporatively cooled in the optical dipole trap by ramping it down from 60 W to 0 W in a few seconds (see Fig. 3.3) while subject to a homogeneous magnetic field of 330 G which sets the scattering length to $-290a_B$. Once held only by the transport trap, the focus of the transport beam is then shifted by 28 cm with two mirrors on an air-bearing translation stage, carrying the atoms to the science chamber.

Science chamber

The atoms entering the science chamber are trapped by a beam angled with respect to the transport beam, thereby forming a “cross” trap. While in the cross trap, a “dimple” trap at 780 nm is turned on and the transport beam is ramped down, providing another stage of evaporative cooling. The dimple trap is a light sheet with a highly elliptical waist - narrow waist of 1.7 μm along the z-axis and a large waist of 10 μm along the x-axis.

The cross trap is then ramped down to a lower value and the atoms ($\approx 10^4$) are trapped in the dimple trap (see Fig. 3.4). In this way, by loading into a small-volume trap from a larger volume trap, we increase the control of the total atom number in the final cloud. The elliptical waist also means that the resulting cloud is now compressed into an elliptical geometry. At this point, a lattice along the vertical (z- axis) direction is ramped up and the dimple is aligned such that the atoms are efficiently loaded into a single plane of the z-lattice.

To ensure the loading of only a single plane and minimize the overlap of the cloud with neighbouring planes, the dimple is spilled out in the presence of a Feshbach field at which the interactions are moderately attractive ($a_S = -290a_B$).

To realize low entropy Hubbard systems with x - and y -lattices, it is important to cool the atoms further as loading into a lattice can cause heating. Therefore, a final step of magnetic evaporation is performed.

First, a strong magnetic offset field at ~ 600 G keeps the $|1\rangle$ and $|2\rangle$ states in the Paschen-Back regime (scattering length of $a_S = +353a_B$), where the magnetic force acting on either spin component is equal.

At the same time, a gradient field is ramped up which tilts the potential and changes the effective trap depth, thereby spilling out the most energetic atoms (see Fig. 3.5). The final value of the gradient field fixes the atom number in the experiment precisely, and consequently, also sets the temperature of the system.

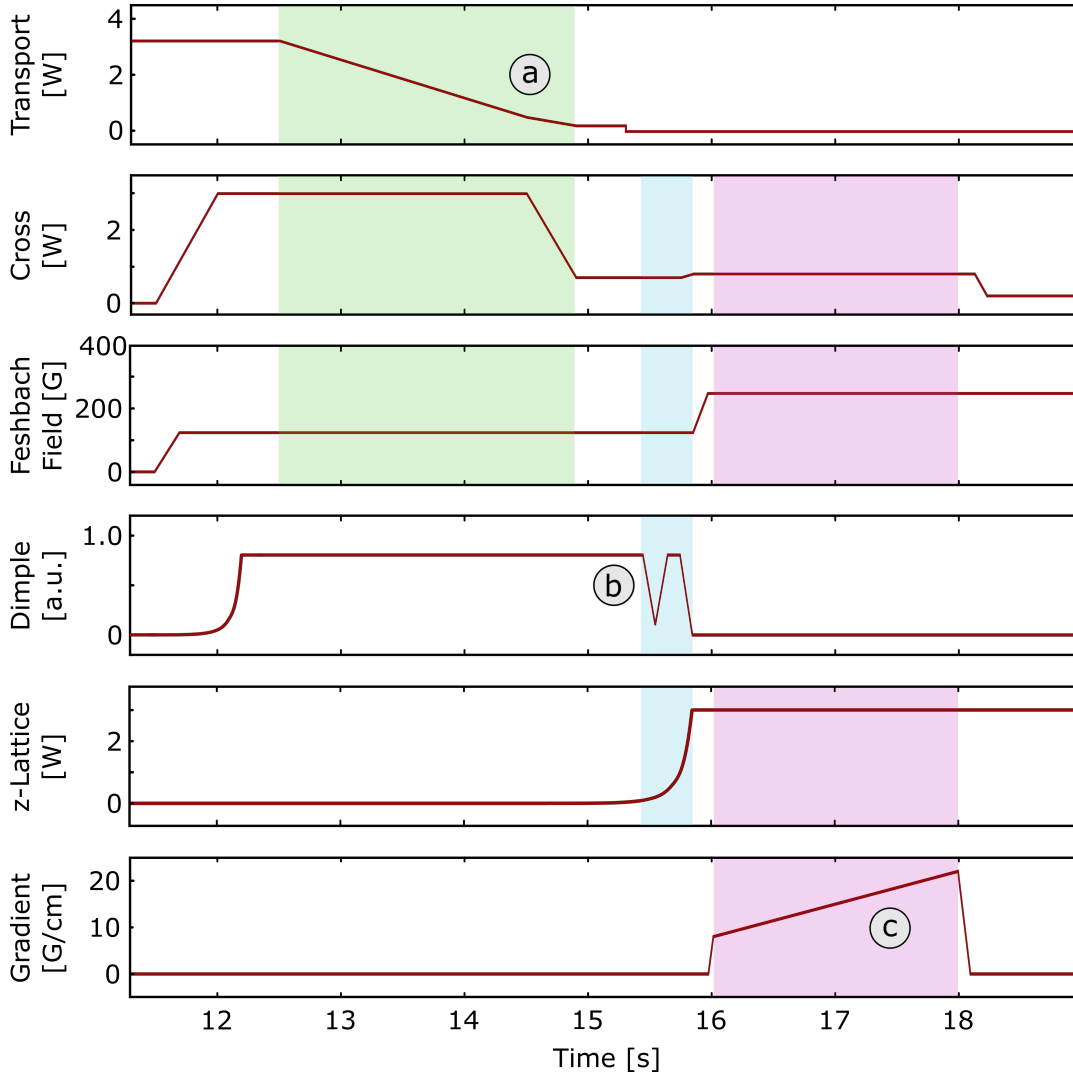


FIGURE 3.4: **Timeline in the science chamber.** **a**, The second evaporative cooling stage happens in the science chamber when the transport is ramped down in two seconds in the cross trap. After this, the cross power is reduced so as to trap atoms in the light-sheet dimple beam. **b**, A spillout of the dimple is performed (see text) and the atoms are loaded into a single plane of the z-lattice, which is ramped up in this time. **c**, Magnetic evaporation in the two dimensional plane is accomplished by applying a large Feshbach field (with a scattering length of $a_S = +353a_B$) which places the atoms of both states in the Paschen-Back regime.

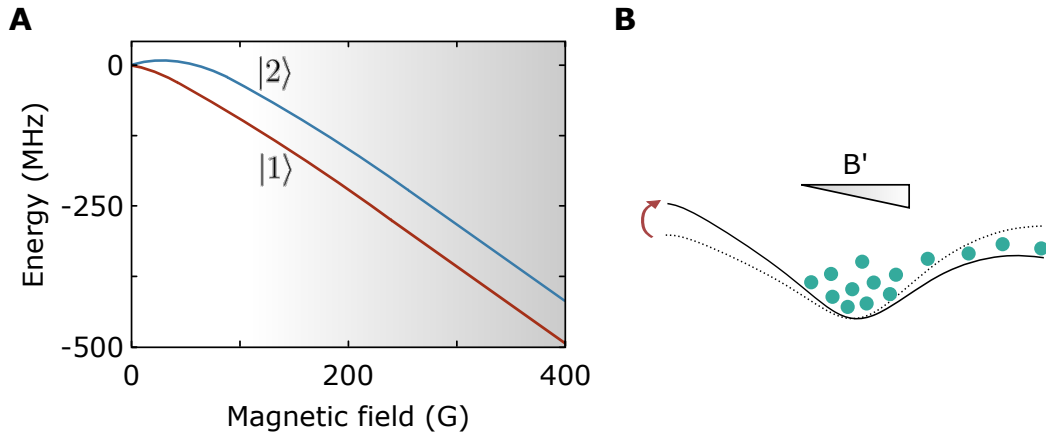


FIGURE 3.5: **In-plane evaporative cooling with a gradient field.** **A**, At offset fields greater than 100G, both spin states are in the Paschen-Back regime (grey shaded region). A schematic of the tilt introduced by the gradient field is shown in **(b)**.

3.3 Optical lattices

For all the experiments described in this thesis, we make use of three sets of optical lattices. The first two are the “physics” lattice and superlattice in which the physical processes of interest given by the Hubbard model such as tunneling and spin-exchange events occur. The third set of lattices are used exclusively for imaging in which the atoms are frozen in place and no dynamics occur. This sections will describe the working of the physics lattice and superlattice setups and how we use them to prepare one- and two-dimensional Fermi-Hubbard systems following the stages of cooling described in the previous section. The pinning lattice will be described in more detail in Sec. 3.4.1.

The standard techniques used to generate a square optical lattice involve either interfering counter-propagating beams or by retro-reflecting single beams to produce a standing wave with lattice spacing $a_L = \lambda/2$. However, in our case, we make use of the interference of two (or four) beams under an angle ϕ to generate one-(or two-) dimensional optical lattices with lattice spacing $a_L = \frac{\lambda}{2 \sin(\frac{\phi}{2})}$. Setting ϕ to 180° recovers $a_L = \lambda/2$ expected for counter-propagating beams. The beams are angled towards one another by the use of a lens. In our experiment, the x - and y -lattices use the objective lens of our quantum gas microscope whereas the z -lattice uses an external lens.

A schematic of the lattice generation technique is shown in Fig. 3.6. A superlattice is easily generated by adding beams which are half the distance (leading to twice the lattice spacing) closer to the principle axis of the lens. The frequency of the superlattice beams are kept slightly different to avoid cross interference. The lattice constant is directly tunable by shifting the position of the beams with respect to the principle axis of the lens. However, for all the experiments reported here, the beams are kept at a fixed distance from the principle axis, providing a lattice spacing of $a_x = a_y = 2.3\mu\text{m}$ with only the lattice beams and $a_x = a_y = 1.15\mu\text{m}$ with the superlattice beams. In this way, we project 8 parallel beams onto the objective to generate our xy -lattices and superlattices. These 8 parallel beams are prepared interferometrically and is described in detail in the masters thesis of M. Lohse.

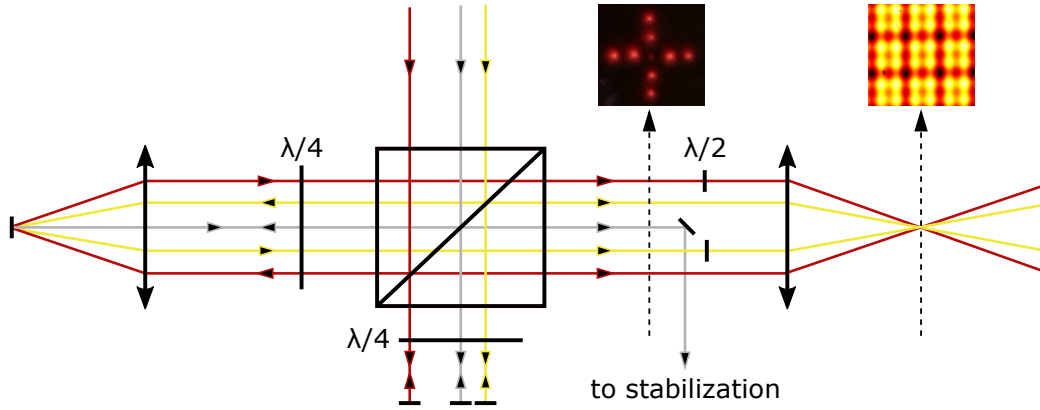


FIGURE 3.6: **Generation of optical lattices.** Two pairs of beams, one twice as far from the principle axis as the other, are used interferometrically to produce parallel beams. On focusing these beams through a lens, standing wave patterns with two different lattice spacings are generated.

As we shall see in Sec. 3.4.3, the relative phase fluctuations between the lattice and the superlattice beams needs to be minimized for efficient spin resolved imaging. To obtain good phase stability, we use a beam (in grey in Fig. 3.6), which runs along the optical axis. It is split into two by the beam splitter and the two orthogonally polarized beams coming from either paths are recombined. This stabilization beam is then picked out, its polarization rotated and made to interfere on a photodiode, which generates an error signal that is sent to a lock-in detector. Based on this signal, the mirror on the long arm (left-most mirror in Fig. 3.6) is continuously adjusted by a piezo controller.

In addition to these 8 beams which make up the xy -lattice, two more parallel beams are used to generate the z -lattice with lattice spacing of $a_z = 3.12\mu\text{m}$ which was briefly mentioned in the previous section. These beams are also prepared interferometrically and are sent into the science chamber through an aspheric lens. The dimple trap is aligned with the z -lattice in such a way that only one plane of the z -lattice is loaded with atoms before ramping up the xy -lattices.

By tuning the relative intensities of the x - and y -lattice beams, Fermi-Hubbard systems in one-, two- and quasi-one-dimensions can be prepared and results pertaining to each of these scenarios will be described in this thesis.

3.4 Single site resolved imaging

The triumph of quantum gas microscopes lies in their ability to obtain information about the density at the level of a single site, thereby enabling the extraction of nearest-neighbour as well as multi-point correlations in the snapshot of a single experimental realization.

Our experiment is unique in that it has the ability to resolve both the density and the spin of atoms at the level of a single lattice site. This allows us to evaluate space-resolved multi-point density as well as spin correlations in a single snapshot which is at the heart of the results presented in Chapters 4, 5 and 6. Additionally,

our experiment overcomes the problem of parity projection due to light assisted collisions and enables us to uniquely identify holes and doublons.

In this section, the imaging technique we use to generate snapshots with single-site density and spin resolution is described.

3.4.1 Raman sideband cooling in a pinning lattice

When it comes to imaging, the advantage of using ${}^6\text{Li}$ is also its biggest disadvantage - it has a light mass. The fluorescent photons at 671 nm scattered from imaging beams impart a considerably large recoil energy onto the ${}^6\text{Li}$ atoms: $E_{\text{rec}} = \frac{h^2}{2m\lambda^2} \approx h \cdot 74 \text{ kHz}$. To collect the several hundred photons requires getting a good signal-to-noise ratio without kicking the atom out of the lattice site, and consequently an efficient cooling mechanism in a deep lattice is a necessity.

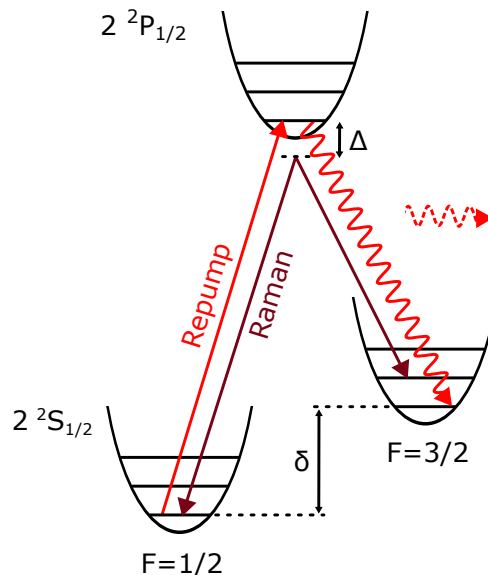


FIGURE 3.7: **Raman sideband cooling scheme.** Dark and bright red arrows are the Raman and repumper beam respectively. The dashed bright red line represents the fluorescent photon which is sent to a camera. The hyperfine splitting energy is denoted by δ and the detuning of the Raman beams by Δ . With every cooling cycle, the atoms are pumped to a lower vibrational energy level and a fluorescent photon is generated. The Raman beams are sent to the atoms for 500ms, during which the cycle is repeated a few hundred times.

Cooling mechanisms such as optical molasses and EIT cooling do not work for ${}^6\text{Li}$ due to the small hyperfine splittings in the excited state which do not allow for cycling transitions. We instead use the technique of Raman sideband cooling for our imaging. A deep lattice for imaging could in principle be achieved by either ramping up the power of the physics lattice or by focussing it to a smaller waist. However, there is not sufficient optical power available in our physics lattice beams and reducing the waist implies a stronger confinement which would result in smaller systems sizes.

Hence, we instead trap the atoms in an additional set of high power lattices called the “pinning lattice”, which has a lattice spacing of 532 nm while collecting fluorescence photons. The small spacing of the pinning lattice also contributes to the on-site trapping frequency of each lattice site during the imaging. Using such a pinning lattice has the added benefit of decoupling the physics from the imaging as well as avoiding parity projection, as we shall see.

To perform Raman sideband cooling, we use a pair of beams at 671 nm to couple the lowest two hyperfine states $|2S_{1/2}, F = 3/2, \nu\rangle$ and $|2S_{1/2}, F = 1/2, \nu - 1\rangle$. Once in the lower energy vibrational state, the atoms are pumped back into the $|2S_{1/2}, F = 3/2\rangle$ manifold. However, by optically pumping using a repumper on the $|2S_{1/2}, F = 1/2\rangle \rightarrow |2P_{1/2}, F = 3/2\rangle$ line, the atoms are pumped into a level with lower vibrational energy $|2S_{1/2}, F = 3/2, \nu - 1\rangle$, along with the emission of a fluorescent photon, as shown in Fig. 3.7.

In the end, the atoms are in the $|2S_{1/2}, F = 3/2, 0\rangle$ state which does not couple anymore to the Raman beam in principle. But there is still sufficient off-resonant scattering the Raman and repumper beams to produce more fluorescent photons. An EMCCD camera with a quantum efficiency of 95% is then used to collect the fluorescent photons over a period of 500 ms.

The 3D pinning lattice, with lattice spacings of 532 nm, are formed by retro-reflecting three high power (> 20 W per axis) laser beams at 1064 nm, each produced by a Nufern fiber amplifier. Due to the smaller spacing of the pinning lattice with respect to the physics lattice, each physics lattice point is oversampled by multiple pinning lattice sites. In this way, the working of the pinning lattice is decoupled from the geometry of the underlying physics lattice.

The oversampling allows multiple atoms in a single physics lattice site to fall into different pinning lattice sites for imaging, thereby avoiding light-assisted collisions, enabling the parity-projection-free detection of holes and doublons, as we shall see in the next section. A site with a doublon would then simply show a higher fluorescence count from the area of a single physics lattice site.

3.4.2 Single site density resolution

It is the ability of our experiment to obtain density and spin resolution at the single site level in a single shot that enables use to evaluate multi-point charge and spin correlation functions which is the basis of the results presented in this thesis. The previous section on Raman sideband cooling in a pinning lattice already provides the framework as to how we achieve single-site resolution.

The fluorescent photons from the Raman sideband cooling process are collected by the high resolution objective (which is our “microscope”, with a numerical aperture $NA = 0.5$ and focal length $f = 28.1$ mm). These photons are then imaged onto an EMCCD camera with a lens of focal length $f = 1700$ mm.

With our superlattice, the smallest lattice spacing we work with is $a_x = a_y = 1.15 \mu\text{m}$. The microscopic objective was independently tested to have a resolution of $\sim 1 \mu\text{m}$, directly indicating that it is possible to distinguish atoms on neighboring lattice sites.

A typical experimental run takes around 500 ms to perform the imaging during which ~ 300 photons per lattice site are collected on the camera to obtain a snapshot

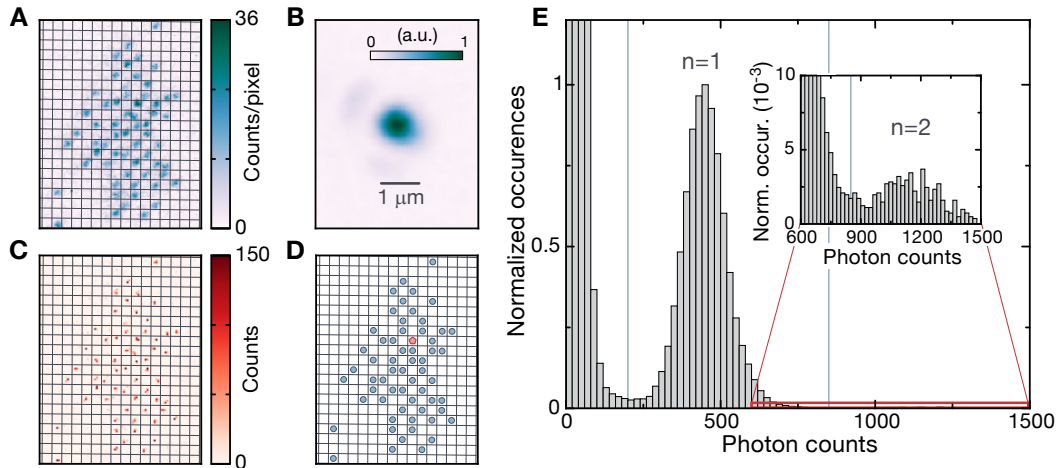


FIGURE 3.8: **Single site charge resolution.** **A**, A single shot of the experiment which shows the fluorescent photons from the Raman sideband cooling of the atoms. **B**, Point-spread-function of the imaging system. The Gaussian widths are $\sigma_1 = 314$ nm and $\sigma_2 = 363$ nm along the principal axes. **C**, A deconvolution algorithm (Richardson-Lucy algorithm [130]) uses the PSF from (B) to reconstruct the occupation in the lattice. The color scale represents the counts per pixel after this deconvolution. **D**, Reconstructed image indicating the occupation in every lattice sites (empty sites, singly occupied ones (blue) and doublons (red)). **E**, Histogram of photon counts per lattice site normalized to the $n = 1$ peak. Vertical lines are thresholds for determining occupation. Image is taken from taken from [129].

with good signal to noise ratio. The lattice occupations are reconstructed using a deconvolution algorithm which uses the measured point-spread function as input (see Fig. 3.8). To extract the exact occupation per lattice site, we look at a histogram of the photon counts and fit a Gaussian to the peaks of the distribution. The readout fidelities are obtained by calculating the overlap of the Gaussians corresponding to $n = 0, n = 1$ and $n = 2$ atom numbers per site to be 99% for singly occupied sites and 95% for doubly occupied sites.

The pinning lattice used in the imaging process consists of high power 1064 nm beams used to generate a deep lattice to suppress tunneling events during imaging. The lattice depth provided by the pinning lattice beams is in the end a limiting factor for the tunneling and at the moment, there are no reasonable alternatives with higher output powers in the market.

As mentioned in the previous section, the pinning lattice has a spacing of 532 nm and it completely oversamples the physics lattice sites with a spacing of $a_x = a_y = 1.15 \mu\text{m}$. Directly imaging a lattice site with two atoms leads to light induced collisions that kicks both atoms out of the site, resulting in a site whose collected fluorescence signal is identical to that of a site with no atoms. Decoupling the physics from the imaging process by the use of two independent sets of lattices with different spacings allows us to prevent light assisted collisions that lead to parity projection and thereby the ability to uniquely identify holes from doublons.

For a spin-balanced Fermi gas in a lattice, sites with two atoms usually contain atoms in the two different spin states (due to Pauli blocking) and slowly ramping up the pinning lattice in the presence of repulsive interactions is sufficient to make the

atoms fall into different pinning lattice wells and thereby avoid the effects of parity projection during the Raman sideband cooling/imaging.

3.4.3 Single site spin resolution

Once the techniques used to obtain density-resolved images of Fermi gases in optical lattices has been established, the natural question that follows concerns how to get spin-resolved images. Some laboratories rely on imaging one spin component at a time to reconstruct the spin distribution. In such experiments, a typical “snapshot” usually consists of three images obtained from three separate experimental runs, one imaging the spin $|\uparrow\rangle$ distribution after removing the $|\downarrow\rangle$ atoms, a second imaging the spin $|\downarrow\rangle$ distribution after removing the $|\uparrow\rangle$ atoms and a third where both spin components are kept [71, 72, 131]. The clear disadvantage of such experiments is the inability to extract multi-point spin correlation functions in a single realization of the lattice gas.

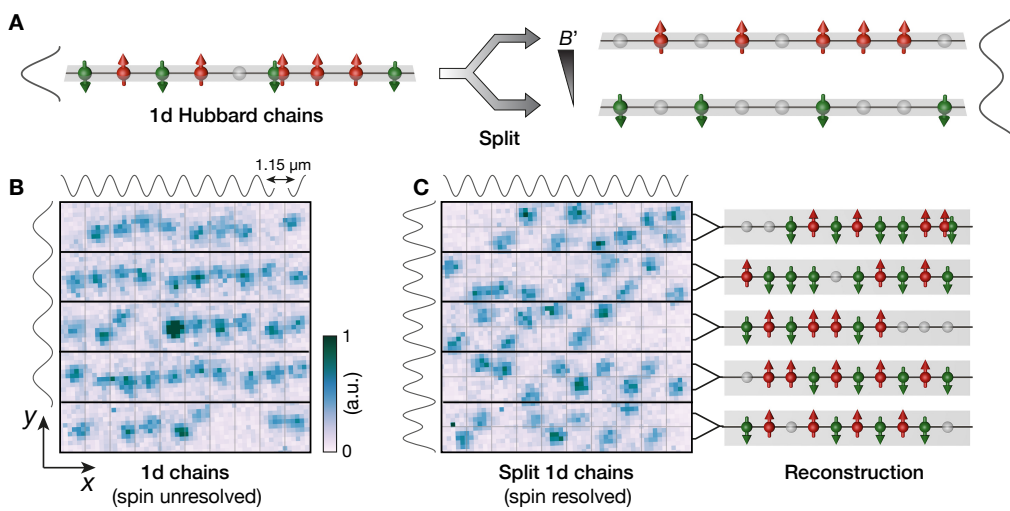


FIGURE 3.9: **Spin resolved imaging of Hubbard chains.** **A**, A cartoon schematic of the technique. **B**, Each site of the chain is split into a local double well potential by ramping up the superlattice beams. To make the splitting process spin-dependent, a magnetic field gradient B' is applied to separate the two spin components preferentially into either the upper or lower well of the local double well potential. This allows for the simultaneous detection of up spins ($|\uparrow\rangle$, red), down spins ($|\downarrow\rangle$, green), doublons (up and down spins overlapping) and holes (gray spheres) and thus for a full characterization of the Hubbard chains, as in **(C)**. From such a snapshot, it is straightforward to reconstruct the Hubbard chains. Figure taken from [73].

In our case, we overcome this problem by employing an additional set of lattices, called the superlattices, which have been described in the Sec. 3.3. First, the physics of interest is allowed to happen in a large spaced lattice ($a_y = 2.3 \mu\text{m}$) along the y -axis and a short spaced lattice ($a_x = 1.15 \mu\text{m}$) along the x -axis. The distribution of atoms is frozen in place by ramping up this physics lattice. Then the short-spaced lattice along the y -axis ($a_y = 1.15 \mu\text{m}$) is ramped up, thereby splitting every potential well in the lattice into a double well along the y -axis (see Fig. 3.9). The double well is made symmetric by tuning the relative phase between the lattice and the superlattice beams.

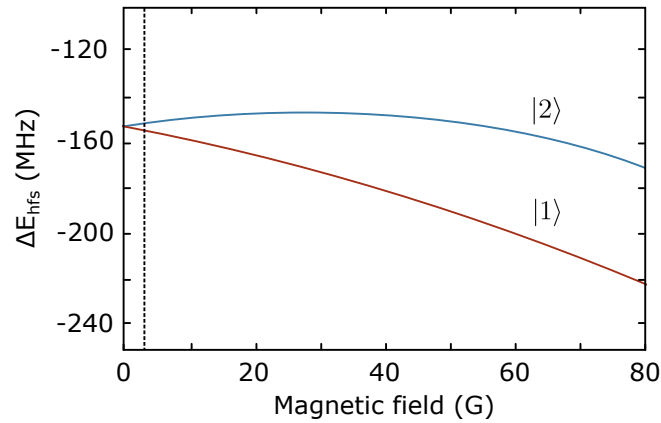


FIGURE 3.10: **Magnetic moments experienced by spin $|\uparrow\rangle$ and $|\downarrow\rangle$ as a function of external magnetic field.** At a constant applied background field of ~ 3 G (indicated by the dashed line), the magnetic moments of the two spin states have opposite signs.

Simultaneously, a magnetic field gradient is ramped up as well along the y -axis, which makes the atoms experience a spin-dependent force. This is because the magnetic moments of the two spin states have opposite signs (of similar magnitude) in the linear Zeeman regime, which is achieved by applying a constant magnetic field of ~ 3 G in addition to the gradient field (see Fig. 3.10).

The spin $|\uparrow\rangle$ and $|\downarrow\rangle$ atoms are thus transferred into separate wells of the double well potential. Since the Zeeman shifts induced by the magnetic field gradient is high compared to the relative phase fluctuations of the superlattice (see discussion in Sec. 3.4.1), the process is effective. In this way, a local Stern-Gerlach splitting occurs at every single lattice site. At the end of this step, the pinning lattice is ramped up and the fluorescent imaging process begins. Since we have the resolution to image every site of the short spaced lattice, we can directly use our superlattice splitting technique to obtain both spin- and density- resolved images.

3.5 Antiferromagnetic correlations in Hubbard chains

Understanding the microscopic mechanisms leading to the phase diagram of the Fermi-Hubbard model shown in Fig. 2.1 is at the foundation of some of the work presented in this thesis. In particular, we address such questions as what happens when a single dopant is added in an antiferromagnet, and how is it different in one and two dimensions. What is the interplay between charge and spin at the most fundamental level? In order to explore the phase diagram, it is important to prepare systems at temperatures cold enough to have antiferromagnetic correlations. The onset of antiferromagnetic correlations in the Fermi-Hubbard model occurs below a critical entropy per particle of $s^* = S/Nk_B = \ln(2)$ [132–134]. With the tools and techniques described in the previous section, we are in a position to prepare Fermi-Hubbard chains of cold atoms at as low a temperature as we can and measure the spin correlations present in the system.

The operator of choice for us to measure spin correlations across the chain is the

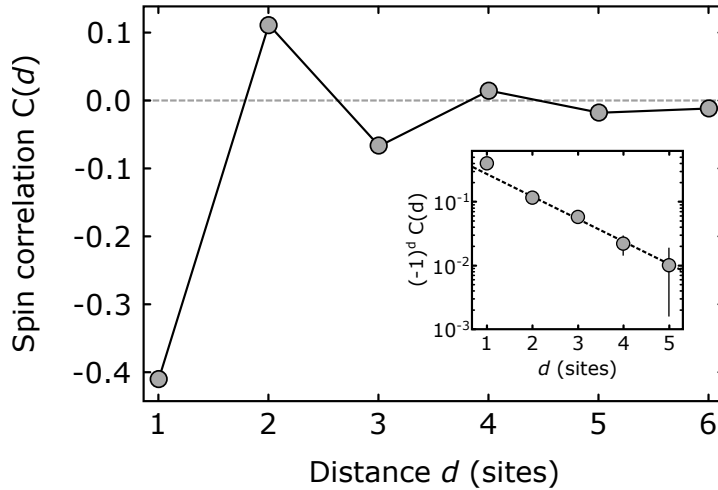


FIGURE 3.11: **Measured Spin correlations vs distance at $U/t = 8.2$.** Averaging over thousands of Mott insulating chains (density $\in [0.95, 1.05]$), we can extract the mean spin correlations in the chain as a function of distance. The alternating positive and negative values of the spin correlator $C(d)$ is a direct signature of the antiferromagnetic ordering. Correlations up to five sites are statistically significant. Solid black line is a guide to the eye. The inset shows the decay of the staggered spin correlator $C_s(d) = (-1)^d C(d)$ in a logarithmic plot together with an exponential fit $C_s(d) \propto \exp(-d/\xi)$ (indicated by dashed black line) revealing a decay length of $\xi = 1.2(1)$ sites. All error bars represent one s.e.m. Figure adapted from [76].

standard two-point spin correlator $C(d) = 4(\langle \hat{S}_i^z \hat{S}_{i+d}^z \rangle - \langle \hat{S}_i^z \rangle \langle \hat{S}_{i+d}^z \rangle)$ which computes the spin correlation between two spins separated by a distance d , where $\hat{S}_i^z = (\hat{n}_{i,\uparrow} - \hat{n}_{i,\downarrow})/2$ are the spin operators.

In one dimension, long range order is absent at all temperatures and the spin correlations are expected to follow an algebraic decay with distance [75, 134].

When we plot the spin correlations $C(d)$ as a function of distance obtained from a dataset with ~ 2000 snapshots at $U/t = 8.2$ and an average density of 1 ± 0.05 per site, a strong negative value of nearest neighbour correlation $C(1) = -0.410(5)$ is seen (see Fig. 3.11). This measured average nearest neighbour correlation is close to 70% of the value expected at zero temperature in the Heisenberg model [133, 135]. Fig. 3.11 also shows the exponential decay of the spin correlations as a function of distance.

These experiments, along with similar results in other quantum gas microscope laboratories [71, 72] are amongst the first to observe antiferromagnetic correlations with full spatial resolution. Previously, short-range antiferromagnetic correlations were observed in cold atoms experiments via singlet-triplet oscillation [32, 136, 137] and by Bragg spectroscopy measurements [33].

One-dimensional Fermi-Hubbard chains will be the basis of the results presented in Chapter 4 and 5. Here the tunneling along the y -axis is suppressed to $t_y/h = 1.2$ Hz by increasing the intensity of the y -lattice. In chapter 6, we consider the case of a single dopant in a two-dimensional antiferromagnet. The crossover from a one- to two-dimensional antiferromagnet is performed by simply varying the relative intensities of the x - and y -lattice beams while keeping U/t constant.

Chapter 4

Real-space observation of incommensurate magnetism

The description of quantum systems based on free quasiparticles, valid in higher dimensions, is absent in one dimension. In 1D quantum systems, the physics is instead described by collective excitations, leading to phenomena such as incommensurate magnetism and spin-charge separation. In this chapter, we will focus on experiments probing incommensurate magnetism, a phenomenon expected to occur when moving away from half filling in the Hubbard model.

The results presented in this chapter are based on “equilibrium” experiments, where optical potentials are ramped as adiabatically as possible and the final state of the lattice gas is imaged. Hubbard chains with a range of density and polarization doping are realized. Our quantum gas microscope enables us to precisely group the chains based on their doping, enabling us to independently probe effects of density doping and spin imbalance $(N_{\uparrow} - N_{\downarrow})/2$.

We will see that the density doping induces a linear change in the spin-density wavevector, in excellent agreement with predictions of Luttinger liquid theory. In the case of a spin imbalance in the chains, the spin-density wavevector is found to reduce with spin imbalance in the chain [113], and is consistent with the antiferromagnetic Heisenberg model in a magnetic field. The microscopic origin of incommensurate correlations is traced to holes, doublon and excess spins, which act as delocalized domain walls in the antiferromagnetic chains.

Discussions on incommensurate magnetism presented here form a basis for the rest of the thesis. First of all, the physics underlying incommensurate correlations in 1D systems in the presence of doping is the factorization of the electronic wavefunction into separate spin and charge sectors - the phenomenon called spin-charge separation, which is discussed in detail in Chapter 5. Secondly, a direct consequence of the breakdown of spin-charge separation as the dimensionality is increased from one to two is the formation of magnetic polarons, which is discussed in Chapter 6. In higher dimensions, incommensurate spin-density waves have been detected in certain high- T_c superconductors [138], possibly due to the formation of stripes as domain walls in the antiferromagnet.

The main results of this chapter are published in:

“Direct observation of incommensurate magnetism in Hubbard chains”

Guillaume Salomon, Joannis Koepsell, Jayadev Vijayan, Timon A. Hilker, Jacopo Nespolo, Lode Pollet, Immanuel Bloch and Christian Gross

Nature **565**, 56–60 (2019)

4.1 Experimentally probing incommensurate magnetism

The preparation of Fermi-Hubbard chains with antiferromagnetic correlations was described in the previous chapter. These Hubbard chains are an ideal platform to probe the phenomenon of incommensurate magnetism. By preparing chains with densities away from half-filling ($n = 1$) and polarization away from balanced ($m = 0$), we can use take snapshots with site-resolved spin and density information, to investigate in real space the dependence of the spin-density wavevector on doping. Here, polarization m is defined as $m = S^z/N_s$, where N_s is the number of singly occupied sites.

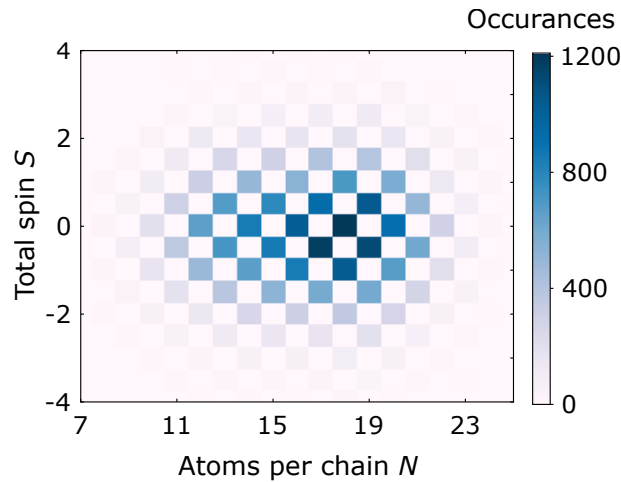


FIGURE 4.1: **Data statistics.** Chain length and total spin histograms of a typical dataset consisting of ~ 5000 snapshots used in the analysis.

For the results described in this chapter, chains are prepared with an interaction energy of $U/t_x = 7$, obtained by tuning U using the broad Feshbach resonance at 834.1 G. The corresponding tunneling rate is $t_x = h \times 400$ Hz and spin exchange rate is $J_x = h \times 220$ Hz. The total magnetization $S^z = (N_\uparrow - N_\downarrow)/2$ and total atom number $N = N_\uparrow + N_\downarrow$ of individual Hubbard chains are conserved quantities of the Hamiltonian for each experimental run. However, they fluctuate for different experimental realizations.

The chain statistics for a typical dataset is shown in Fig. 4.1. It shows that although the highest contributions to our snapshots are from chains with zero spin imbalance and chain length of 17 sites, the spread is large enough for us to explore the correlations away from $m = 0$ and $n = 1$. Chains of length up to 23 sites are used in the analysis.

The fluctuations in chain preparation, combined with the ability to precisely calculate the level of doping and magnetization in the chain, can be taken advantage of to explore the effects of doping and polarization by sorting the data, as shown in see Fig. 4.2.

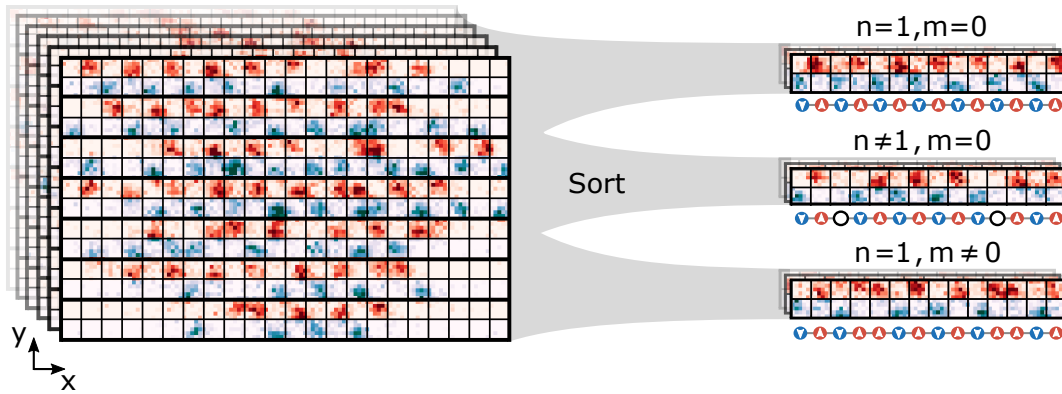


FIGURE 4.2: **Sorting data based on chain properties.** Each snapshot from an experimental run contains ~ 7 independent Hubbard chains along y (separated by thick lines) where spins \uparrow (\downarrow) are represented in red (blue). For the analysis, chain statistics of every chain in every snapshot are calculated and the chains are grouped by magnetization and density doping.

Grouping each chain data by $\{j, N, S^z\}$, where j is the coordinate of the Hubbard chain in the y -direction, allows us to explore different filling and spin sectors. In the analysis, we can selectively look at spin balanced chains away from half-filling to study the effect of hole doping on the antiferromagnetic order or we can alternatively look at chains at half-filling but with a spin imbalance to study the effect of excess spins on the antiferromagnetic order.

4.2 Effect of doping on spin correlations

As we saw in Section 2.3, from Luttinger liquid theory, the wavevector of the spin density wave is expected to be $k_{\text{SDW}} = 2k_{\text{F}} = \pi n$, defining the Fermi wave vector k_{F} . Here n is the density, defined as the mean occupation calculated over the sites connecting i and $i+x$ for each value of N . Evaluated over singly occupied sites, the corresponding variation of the spatial spin correlations with density, at finite temperatures and large distances $x > k_{\text{F}}^{-1}$, is of the form:

$$C(x) \approx A e^{-x/\zeta} \cos(\pi n x) \quad (4.1)$$

where A is a non-universal constant and ζ is the temperature-dependent correlation length that varies weakly with density n .

To extract the values of A and ζ , we first look at the case of half-filling ($n = 1$). The subset of the data corresponding to the case in which chains have $m = 0$ and $n = 1$ is used for this purpose.

The spin correlations in the chain are obtained using the same two-point correlator described in Section 3.4 – $C(x) = 4 \langle S_i^z S_{i+x}^z \rangle_{\bullet_i \bullet_{i+x}}$, which quantifies the spin correlation between sites i and $i+x$, conditioned on both being occupied (indicated by filled circles). A plot of $C(x)$ as a function of distance for half-filling is shown in Fig. 4.3 (blue curve) for up to 6 sites. An exponential fit to the curve is used to extract the Luttinger liquid parameters, giving $A = 0.49(4)$ and $\zeta = 1.6(1)$.

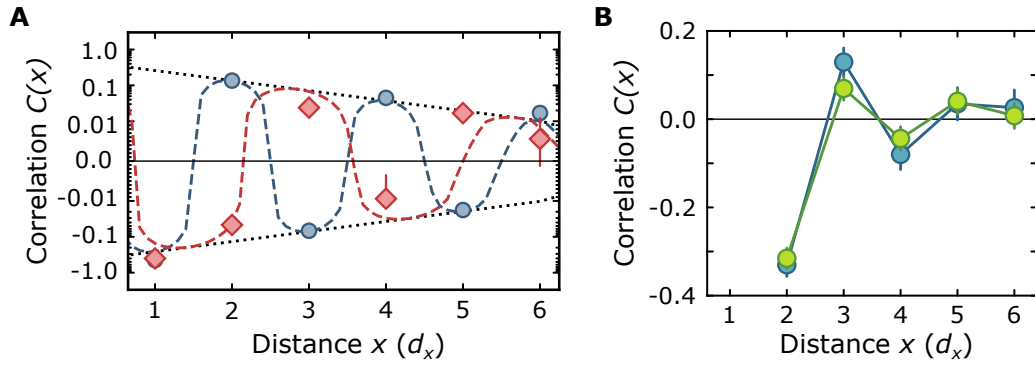


FIGURE 4.3: **Spin correlation $C(x)$ as a function of distance.** **A**, Spin correlations at $n = 1$ (blue) and at $n = 0.7$ (red). The dotted lines show the decay obtained from an exponential fit of the spin correlations at $n = 1$. The dashed lines are the Luttinger liquid predictions using the amplitude and decay length obtained from a fit of the $n = 1$ experimental data. **B**, Antiferromagnetic spin correlations conditioned on having a hole (green) and doublon (blue) at $x = 1$. Error bars denote one standard error of the mean.

Now, to study the effect of density doping, we go away from half-filling by analysing the subset of data in which chains have $n \neq 1$ and $m = 0$. In this way, the effects arising from magnetized chains (chains with excess spins) can be decoupled from the effects arising from density doping. The observable of our choice while going away from half-filling is the Fourier transform of the rescaled spin correlation $C(k) = \mathcal{F}\{A^{-1}e^{x/\xi}C(x)\}$. A linear increase of the spin density wavevector is observed for the case of both hole doping ($n < 1$) and doublon doping ($n > 1$), as shown in Fig. 4.4. The Luttinger liquid expectation $k_{SDW} = \pi n$ is also indicated, and is in agreement with the linear increase measured experimentally.

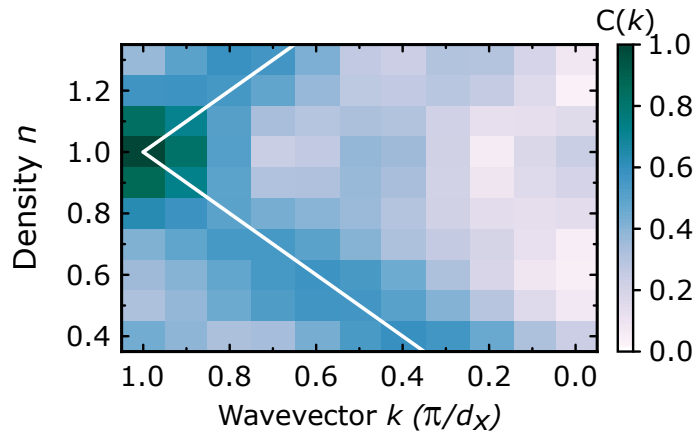


FIGURE 4.4: **Normalized Fourier transform of the spin correlations $C(k)$.** Moving away from half filling, the spin density wavevector decreases linearly with both hole and doublon doping. The stretching of the antiferromagnetic correlations is a direct consequence of the linear decrease of the wavevector. The white line is the Luttinger liquid result $k_{SDW} = \pi n$.

For comparison to the case of half-filling, spin correlations as a function of distance for $n = 0.7$ is also shown in Fig. 4.3 (red curve). One can directly see the

“stretching out” of the antiferromagnetic correlations with distance. Whereas in the half-filled case, the correlator flips sign for $d = 1$ site, in the case of $n = 0.7$, the sign flip happens at $d > 2$ sites. The stretching effect is more pronounced as the density of the dopants is increased.

The effect of holes and doublon doping is identical as shown in Fig. 4.3 (right). When post-selected on having a hole or doublon at position $x = 1$, the antiferromagnetic correlation signal is shifted by one site due to the presence of the dopant. This effect is at the heart of the microscopic picture of incommensurate magnetism away from half-filling in the spin-balanced case.

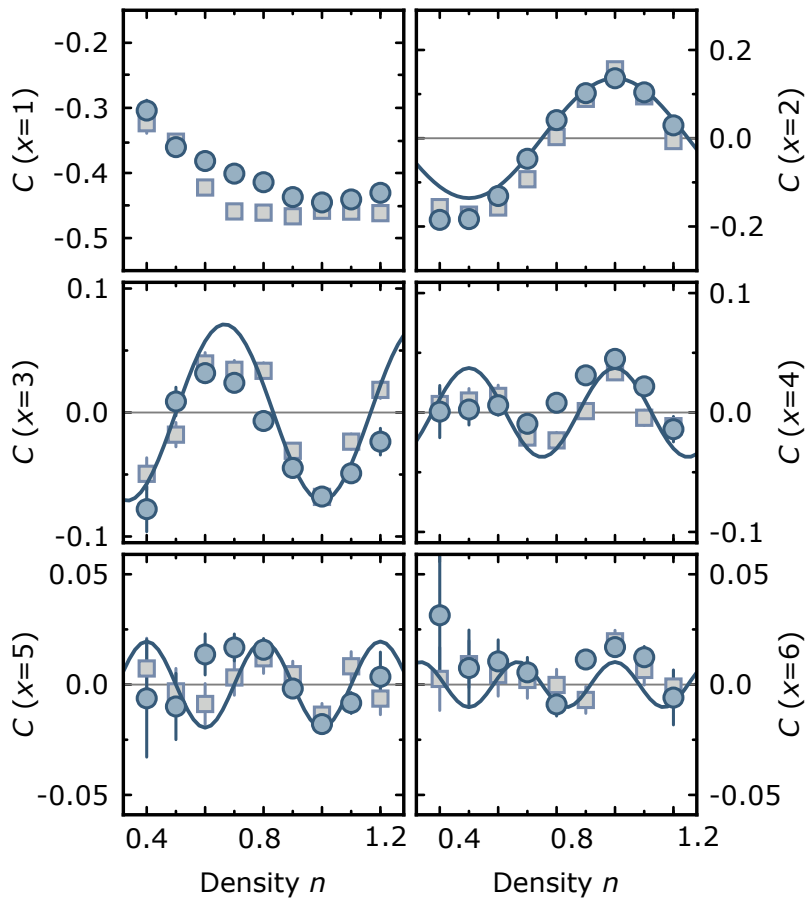


FIGURE 4.5: **Fixed-distance spin correlations vs density.** Spin correlations $C(x)$ vs density at different distances in the chain (blue dots) compared to QMC calculations at $T = 0.29t_x$ (gray squares). The measured densities are binned in intervals of 0.1. Blue lines are the Luttinger liquid prediction with wave vectors πn using the amplitude and decay length extracted from the fit in (a). Errorbars denote one standard error of the mean.

Spin correlations $C(x)$ at different distances are shown as a function of the density (binned in intervals of 0.1) in Fig. 4.5. This allows a quantitative comparison to theory – Quantum Monte-Carlo (QMC) calculations for a homogeneous systems at a finite temperature of $T = 0.29t_x$ are plotted alongside the data. The luttinger liquid predictions based with wavevectors πn obtained from Fig. 4.3 are also shown. The measured spin correlations oscillate with density with a periodicity as predicted

by the Luttinger liquid theory. These oscillations are most pronounced around the region of unity-filling where they are visible up to distances of $x = 6$.

The microscopic origin of this effect is attributed to the delocalization of holes and doublons that act as domain walls which separate π -shifted antiferromagnetic domains [139, 140].

4.3 Effect of magnetization on spin correlations

Density doping by holes or doublons is not the only way to achieve incommensurate spin correlations. However, as discussed in Section 2.2.1, another manifestation of incommensurate magnetic order is by introducing a spin imbalance in the chain. Similar to the effect of density dopants, the presence of excess spins leads to the stretching out of the antiferromagnetic correlations.

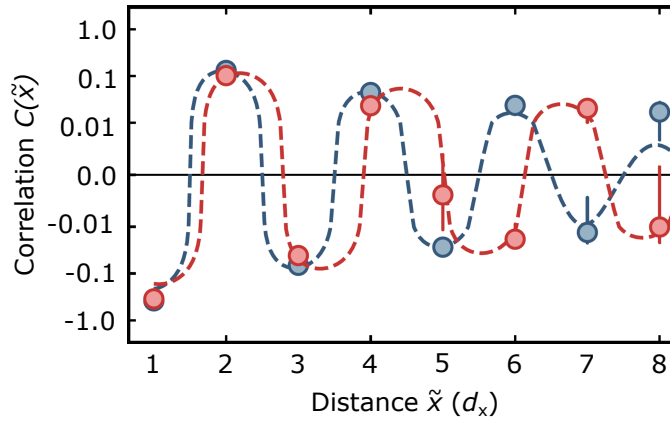


FIGURE 4.6: **Spin correlation** $C(\tilde{x})$ **as a function of distance** for $m = 0$ (blue) and $m = 0.08$ (red). The change of the spin-density wavelength and the consequent sign change at distance $\tilde{x} > 5$ shows the emergence of incommensurate correlations away from $m = 0$. Dotted lines are fits to the Luttinger liquid expectation.

At large U/t_x , the system in the absence of density doping is described by a spin-1/2 antiferromagnetic Heisenberg model. From Luttinger liquid theory, the wavevector of the spin density wave emerging from spin imbalance for a Heisenberg chain is expected to be $k_{SDW} = \pi(1 + 2m)$. Here, m is the magnetization of the chain, defined as $m = S^z/N_s$, where N_s is the number of singly occupied sites. The corresponding variation in the spatial spin correlations is:

$$C(\tilde{x}) \approx A_m e^{-\tilde{x}/\xi_m} \cos(\pi(1 + 2m)\tilde{x}) \quad (4.2)$$

where A_m, ξ_m are the spin imbalance- and temperature dependent amplitude and correlation length respectively. The analysis for this section is performed in squeezed space (denoted by \tilde{x}) obtained by removing holes and doublons from the analysis [116, 117, 139, 140], in order to isolate the effect of magnetization from the influence of density doping. In squeezed space, the two-point correlator has the form $C(\tilde{x}) = 4\langle S_i^z S_{i+\tilde{x}}^z \rangle$.

In Fig. 4.6, the spatial variation of the spin correlations are shown for $m = 0$ and $m = 0.08$. The spin correlations flip sign at every site, as expected, for the

unmagnetized case. However, for $m > 0$ (and $m < 0$, symmetrically), the spin-density wavelength is expected to increase linearly with $|m|$. At $m = 0.08$, the spin correlations stretch out spatially compared to the unmagnetized case and a sign flip is visible at distances $\tilde{x} > 5$, consistent with the theory predictions.

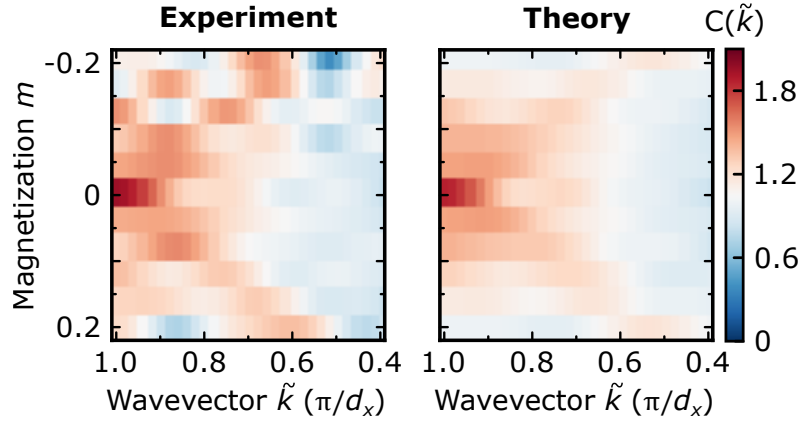


FIGURE 4.7: **Normalized Fourier transform $C(\tilde{k})$ of $C(\tilde{x})$.** The presence of excess spins in the chain, the wavevector decreases linearly with magnetization. The two branches departing from $k = \pi$ as $m \neq 0$ are in good agreement with exact diagonalization calculations of the Heisenberg chain (right). Binning of the magnetization is in intervals of 0.04.

In a method similar to the density doping case, the variation of the spin-density wavevector is studied as a function of spin imbalance by calculating the Fourier transform of the rescaled spin correlations in space, $C(\tilde{k}) = F\{C(\tilde{x})/|C(1)|\}$, for different amounts of spin imbalance.

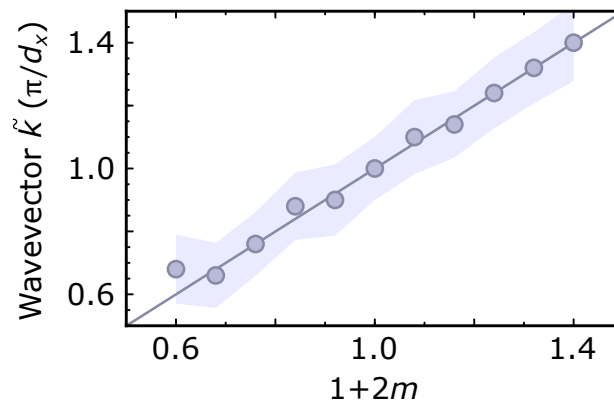


FIGURE 4.8: **Linear fit of wavevector \tilde{k} .** A linear fit of the branches in Fig. 4.7 enables the extraction of the spin-density wavevector $k_{SDW} = 1.0(1) \times (1 + 2m)\pi$. The shaded region denotes the Fourier-limited systematic error.

The dependence of the wavevector on polarization m is shown in Fig. 4.7. Away from $m = 0$, spin imbalance either with excess up spins or down spins, the spin-density wavevector decreases and consequently, the wavelength increases, consistent with the example in Fig. 4.6. The experimental results are compared to results of exact diagonalization of the Heisenberg chain at $T = 0.7J_x$, averaged over the experimental distributions $\{S^z, N_s\}$. A linear fit of the branches emerging in 4.7 away

from zero magnetization shows the linear dependence of the spin-density wavevector on the magnetization (see Fig. 4.8) $k_{\text{SDW}} = 1.0(1) \times (1 + 2m)\pi$, in excellent agreement with the Luttinger liquid predictions.

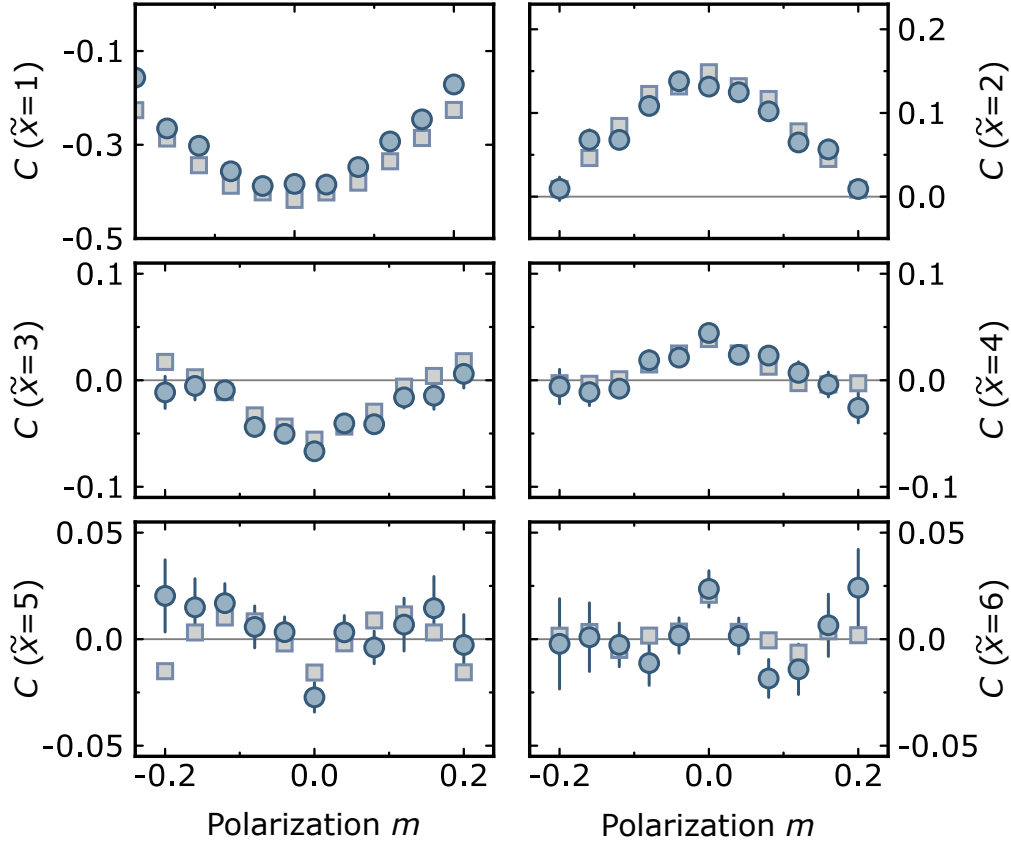


FIGURE 4.9: **Fixed-distance spin correlations vs magnetization.** Experimentally measured spin correlations in squeezed space $C(\tilde{x})$ as a function of magnetization m for different distances in the chain (blue dots) compared to exact diagonalization calculations of Heisenberg chains (grey squares) at $T/J_x = 0.7$ averaged over the experimental $\{S^z, N_s\}$ distributions. Errorbars denote one standard error of the mean.

A quantitative comparison of the experimentally obtained fixed-distance spin correlations $C(\tilde{x})$ to exact diagonalization calculations of the Heisenberg model is shown in Fig. 4.9. Even at distances as large as $\tilde{x} > 5$, there is an agreement with theory and experiment, validating the use of squeezed space analysis away from zero magnetization.

Finally, we investigate the microscopic origin of incommensurate correlations due to spin imbalance. To reveal the effect of excess spins on the magnetic order, we can look at the correlations around majority and minority spins:

$$C_{\text{maj}}(\tilde{x}) = 4 \langle S_i^z S_{i+\tilde{x}}^z \rangle_{S^z \sigma_{i+1} > 0} \quad (4.3)$$

$$C_{\text{min}}(\tilde{x}) = 4 \langle S_i^z S_{i+\tilde{x}}^z \rangle_{S^z \sigma_{i+1} < 0} \quad (4.4)$$

where $S^z \sigma_{i+1}^z > 0$ ($S^z \sigma_{i+1}^z < 0$) indicates that the spin σ_{i+1}^z on site $i+1$ is parallel (antiparallel) to the chain polarization S^z . Plotting these conditional correlators in squeezed space for distances $\tilde{x} \geq 2$ reveals a phase shift of π in the spin order of $C_{\text{maj}}(\tilde{x})$ relative to the unpolarized case (see Fig. 4.10). In comparison, $C_{\text{min}}(\tilde{x})$ remains in phase with respect to the unpolarized case.

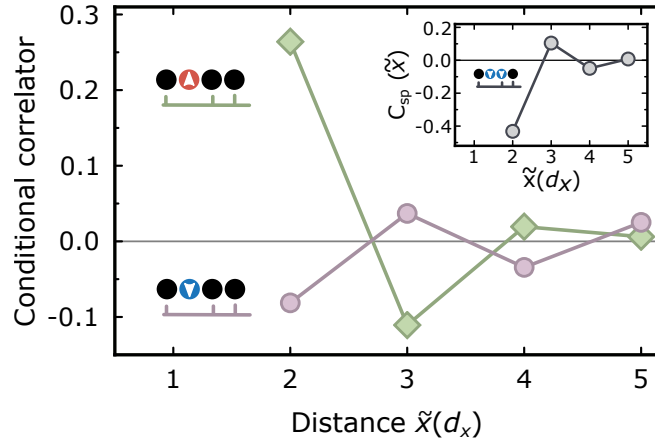


FIGURE 4.10: **Evaluating conditional correlators.** Conditional spin correlations across majority $C_{\text{maj}}(\tilde{x})$ (violet circles) and minority $C_{\text{min}}(\tilde{x})$ (green diamonds) spins for $m = -0.12$. A π phase shift is visible for the spin correlations across majority spins. The inset shows the conditional spin correlations across pairs of parallel spins $C_{\text{sp}}(\tilde{x})$. The strong antiferromagnetic correlations at a distance of two sites reveals the domain wall nature in squeezed space. Errorbars denote one standard error of the mean.

The microscopic implication of the phase shift is that the excess spins form pairs of parallel majority spins, which act as domain walls in squeezed space. This can be further confirmed by directly evaluating the spin correlations across pairs of parallel spins, which shows strong antiferromagnetic correlations, flipped in parity with respect to the unpolarized case (see Fig. 4.10, inset).

4.4 Conclusion

In this chapter, we looked at the spatial variation of the spin correlations in the presence of density- and excess spin-doping. With the ability to directly and simultaneously measure both density and spin in a single snapshot, we could group the dataset into exclusive subsets to study the unique effects of density and magnetization on incommensurate spin-density waves.

The origin of these incommensurate correlations was seen to be the delocalization of domain walls (holes/doublons in case of density doping and parallel majority spins in case of spin polarization) in the antiferromagnetic chain. Our results on a dynamical experiment to probe the phenomenon of delocalized dopants in 1D, is discussed in detail in Chapter 5.

An extension of the work presented in this chapter is to observe the effect of moving to higher dimensions, where at low temperatures, the formation of domain walls is expected to manifest as a binding of dopants to form stripes.

Chapter 5

Spin-charge dynamics in one dimension

We have seen the formation of incommensurate spin-density waves in one dimension by preparing doped antiferromagnetic chains in their ground state and imaging them at equilibrium. The origin of incommensurate correlations was attributed to the independence of the spin and charge modes within the chain. Would it be possible to perform an experiment where we could observe the dynamics of the spin and charge modes with time and space resolution to probe the absence of binding between them and their different propagation velocities? In this chapter, we will explore precisely this phenomenon, considered a hallmark of one-dimensional materials - spin-charge separation - where the spin and charge modes completely decouple, leading to a variety of exotic properties, including incommensurate magnetism. This is in direct contrast to two dimensional materials, where the breakdown of spin-charge separation leads to the formation of magnetic polarons, as we shall see in Chapter 6.

In 1D materials with spin-charge separation, individual constituents such as the electron with properties of charge e and spin $1/2$, are not relevant to the description of the system anymore. Instead, the resultant many-body interaction leads to the emergence of decoupled modes, characterized by independent charge and spin quasiparticles, called holon and spinon respectively. An important consequence of the independence of the quasiparticles is the lack of binding between them, allowing them to propagate at arbitrarily different velocities in the chain [141].

Signatures of spin-charge separation have been observed previously using spectroscopic techniques, such as angle-resolved photoemission spectroscopy (ARPES) [39–41] and conductance measurements in metallic quantum wires [44–46]. Previous results from our own laboratory have seen indirect evidences of spin-charge separation through equilibrium measurements [139, 142].

For the results presented in this chapter, we dynamically probe the phenomenon of spin-charge separation. Starting from a 1D Heisenberg antiferromagnet, we quench the system by removing a single particle, and track the dynamics of the emerging quasiparticles [114, 143]. The tracking of the holon and spinon excitations are done with both space- and time-resolution, meaning that we use the quantum microscope to spatially locate the excitations through their characteristic signatures in spin and charge and take snapshots at different times after the quench to locate them temporally.

Strikingly different velocities are observed for the two quasiparticle excitations,

demonstrating the phenomenon of spin-charge separation. Further, by using multi-point correlators such as the spin correlation across the propagating hole, we will see the absence of binding between the holon and spinon excitations. We will also connect these results to “fractionalization”, where a electron-like quench breaks up into a charge excitation carrying charge e and a spin excitation carrying spin $1/2$ exactly.

In the last section of this chapter, we will consider the effect of changing the tunneling t_x and spin exchange amplitude J_x on the extracted quasiparticle velocities. We will see that the velocities are in fact directly proportional to the timescales of t_x and J_x in the regime that we probe.

The main results presented in this chapter are published in the following:

“Time-Resolved Observation of Spin-Charge Deconfinement in Fermionic Hubbard Chains”

Jayadev Vijayan, Pimonpan Sompert, Guillaume Salomon, Joannis Koepsell, Sarah Hirthe, Annabelle Bohrdt, Fabian Grusdt, Immanuel Bloch and Christian Gross

Science **367**, 186–189 (2020)

5.1 Quenching one dimensional antiferromagnets

The experimental sequence for this dynamical experiment begins similar to what was described in Chapter 4, where 1D chains were prepared to study incommensurate magnetism. A spin-balanced mixture of ^6Li atoms is loaded into several independent 1D tubes by ramping up the x-lattice to $7E_r^x$ and y-lattice to $27E_r^y$, resulting in a tunneling of 250 Hz along x and 1.3 Hz along y - effectively 1D chains.

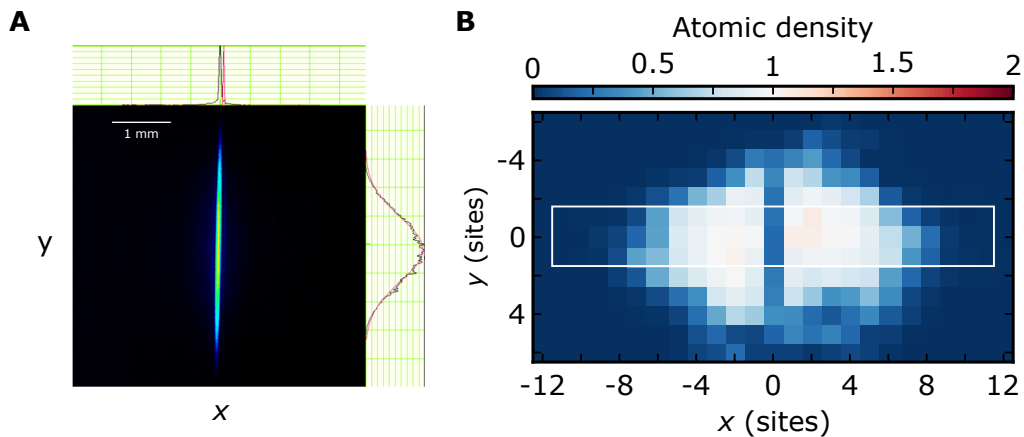


FIGURE 5.1: **Pushout beam profile.** **A**, The pushout beam as imaged onto a camera in a test setup. A high aspect ratio is achieved by slicing the beam with a rectangular aperture before sending it through the objective lens. **B**, Averaged image of the density profile of the cloud (several independent 1D chains along x -axis) in the presence of the pushout beam. A good fidelity of atom-removal is achieved in the central three chains of the cloud (indicated by white box).

During the ramping up of the x - and y -lattices, the scattering length is tuned from $230a_B$ to $2150a_B$, to get an interaction of $U/h = 3.75$ kHz and $U/t = 15$. The corresponding spin exchange amplitude is $J = 4t^2/U = h \times 65$ Hz.

5.1.1 Pushout beam

The dynamics of the quasiparticles is initiated by a quench which removes a single fermion from the chain. Since we prepare many independent 1D chains, we use an elliptical pushout beam (see Fig. 5.1) to remove an atom from each chain.

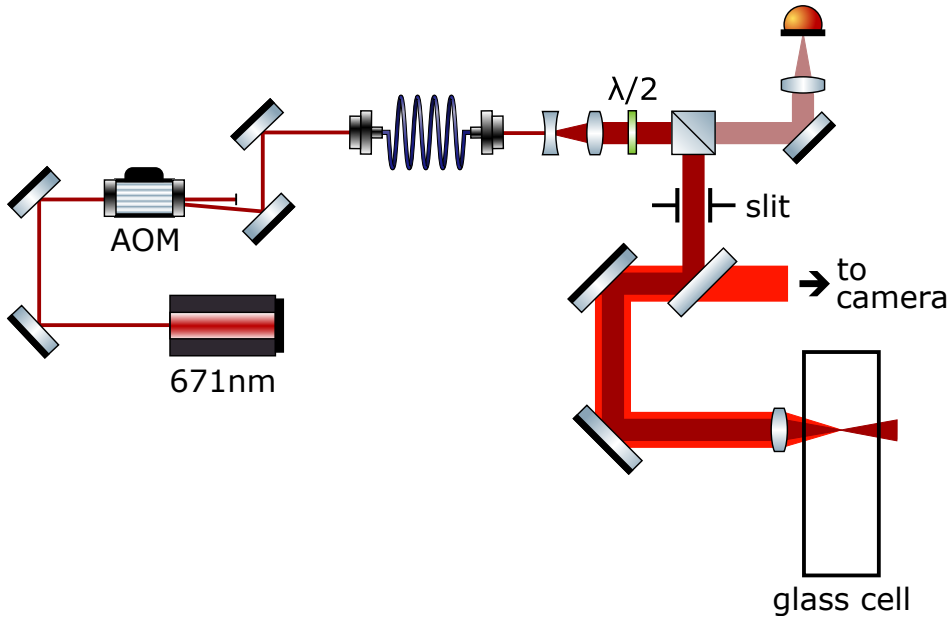


FIGURE 5.2: **Simplified schematic for generation of pushout beam.** The resonant pushout beam is a beam at 671 nm which is sent into an AOM for amplitude and timing control before being coupled into a fiber. At the other end of the fiber, the beam is enlarged to an area similar to the aperture of the objective. A rectangular slit then slices the beam into a highly elliptical beam which has the same waist as before along one axis but a much narrower waist along the other axis. The pushout beam is then directed onto the atoms, where it addresses an entire column of atoms. A photodiode collects part of the light which is then used for amplitude control with the AOM. The fluorescent light collected from the atoms (bright red beam) through the objective is separated from the tweezer beam path and sent to a camera with a dichroic mirror.

The pushout beam is a near-resonant beam at 671 nm and it is focussed to a waist of $\sim 0.5\mu\text{m}$ along its narrow direction. The optical path followed by the pushout beam is shown in Fig. 5.2. Light at 671nm is coupled into a fiber and expanded to the size of the aperture of the microscopic objective so that the waist at the focus at the atoms is of the order of a single lattice site. The exact frequency of the beam is chosen to address both spin components effectively, and is discussed in section 5.1.2.

A rectangular slit then slices the pushout beam such that the resulting focus at the atoms is highly elliptical, as shown in Fig. 5.1. Along one axis, the waist is of

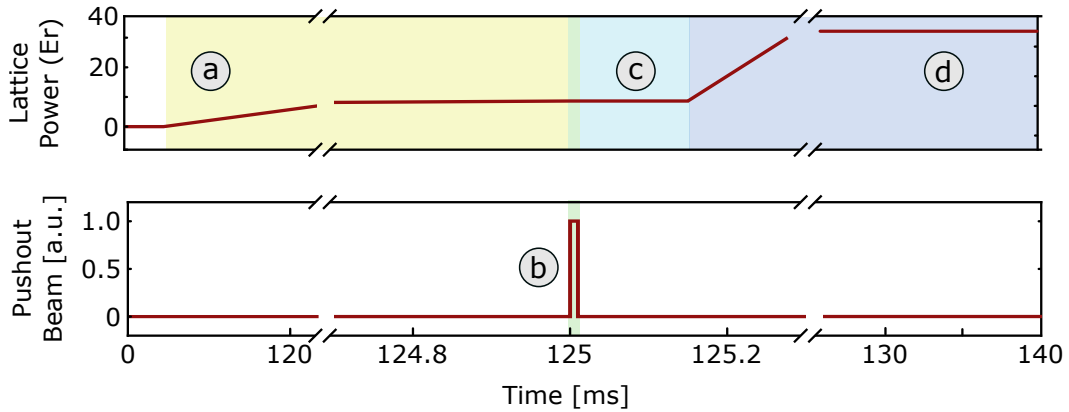


FIGURE 5.3: **Timeline of the optical tweezer stage.** **a**, The physics x - and y - lattices are ramped up adiabatically to prepare the Mott-insulating Fermi-Hubbard chains. **b**, At the end of the lattice ramp up, the pushout beam is pulsed on for $20\mu\text{s}$. **c**, After the pushout, the system is allowed to evolve for a variable period of time. **d**, After the dynamical evolution, the atoms are frozen in place by ramping up the lattices to a large value.

the order of a single lattice site whereas along the other axis, it addresses the entire cloud.

With the right intensity and alignment, the removal of an atom from the addressed can be as high as $\langle n_i^h \rangle = 78\%$ while keeping the probability of removal of an atom from the neighbouring site to be $\langle n_{i+1}^h \rangle \approx \langle n_{i-1}^h \rangle = 14\%$. The ratio $\langle n_i^h \rangle / (\langle n_{i-1}^h \rangle + \langle n_{i+1}^h \rangle)$ is monitored periodically and kept to a value ≥ 2 for the central three chains throughout the experimental data taking process.

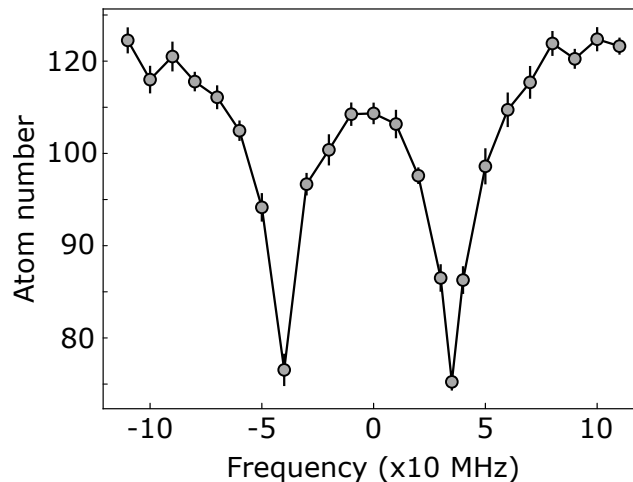


FIGURE 5.4: **Frequency scan of pushout beam.** By tuning the frequency of the pushout beam, we can address either of the two spin states (indicated by dips in atom number). In the experiments that follow, we fix the frequency to a value that ensures spin-independent removal of the atom (indicated by 0 on the x-axis).

In the analysis, we consider only the central three chains in order to avoid averaging results over varying density profiles due to the harmonic confinement. We further post-select on chains which have only a single hole in the central 9 sites. This

boosts $\langle n_i^h \rangle \sim 81\%$ and reduces $\langle n_{i+1}^h \rangle \approx \langle n_{i-1}^h \rangle \sim 5\%$. The overall probability to have a single hole in the chain immediately after the quench is thus $\sim 91\%$.

At the end of the ramp up of the physics lattice, the pushout beam is pulsed on for $20\mu\text{s}$ addressing the central atoms of the chains. After the pulse, the system is allowed to evolve for a variable time before the lattices are frozen and the imaging process begins (see Fig. 5.3).

Tuning the frequency of the pushout beam enables us to selectively address (and remove) the two different spin states $|\uparrow\rangle$ and $|\downarrow\rangle$. However, for the purpose of our experiment, we want to have spin-independent removal atoms and we set the frequency inbetween the two dips seen in Fig. 5.4, indicated by 0 detuning on the x-axis.

5.1.2 System preparation

In order to prepare undoped chains with a large unity-filled region, the total number of atoms in the harmonically confined cloud was fixed between 60 and 90 with a peak around 75 atoms by choosing the appropriate parameters of evaporative cooling. This enabled the preparation of at least three 1D chains with a mean length of 13 atoms, each with a unity filled region of 9 sites.

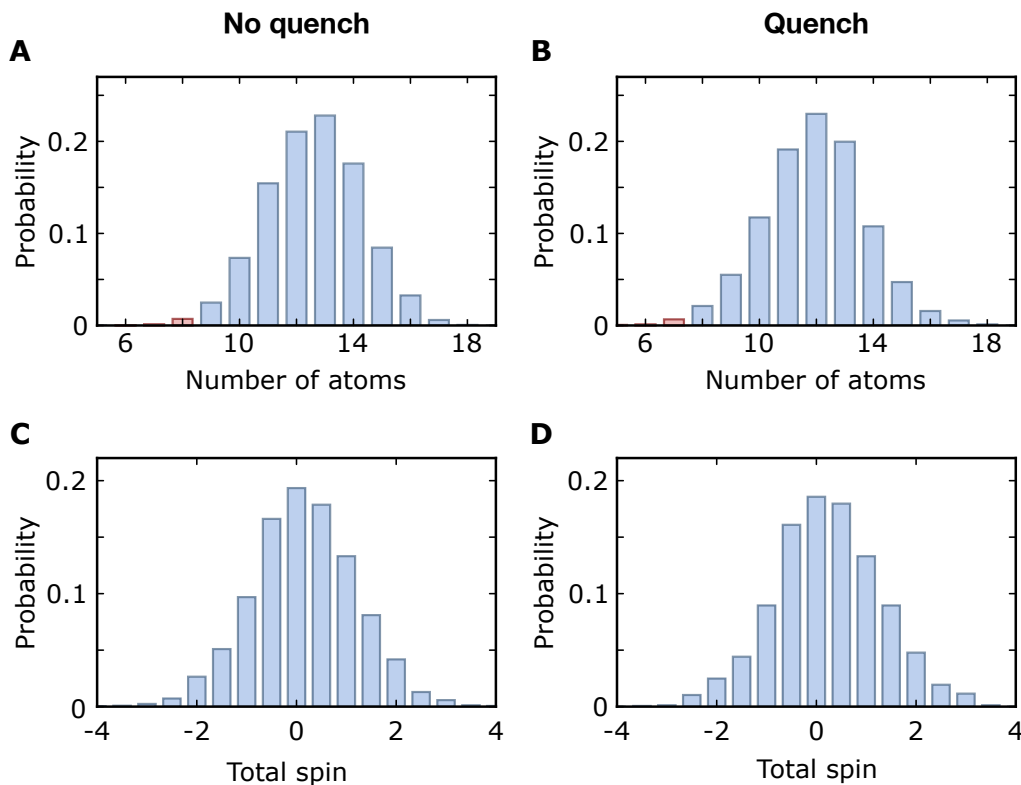


FIGURE 5.5: **Density and spin statistics for the datasets analyzed.** **a**, Atom number distribution per chain without (left) and **b**, after (right) the quench. Red bars indicate data which was excluded from the analysis. **c**, Magnetization $\sum_i \hat{S}_i^z$ of the analyzed chains without (left) and **d** after (right) the quench.

A histogram of the length and magnetization of the chains is shown in Fig. 5.5 with and without the quench, for the central three chains of each cloud. Since the

analysis is performed on chains with a unity-filled region of nine sites, chains with fewer than 9 atoms are not included in the analysis. It represents statistics from > 13000 snapshots. The quench reduces the number of atoms by one but leaves the magnetization unchanged.

It must be noted that the local quench as described here is a relatively high-energy quench, meaning that we excite a large number of momentum modes of the quasiparticles. This means that we do not probe the Luttinger liquid regime, which describes low energy excitations, anymore. This places us in a unique position to probe the regime inbetween the low-energy Luttinger liquid description and the spin-incoherent Luttinger liquid for which the temperature is on the order of or exceeds the magnetic energy ([144] and Sec. 2.3.

5.2 Dynamics of holons and spinons

Now that the ingredients required to perform a dynamical spin-charge separation experiment have been described, we can go ahead and discuss the results. Starting with a 1D Fermi-Hubbard chain with short-range antiferromagnetic correlations, we perform the quench with the pushout beam.

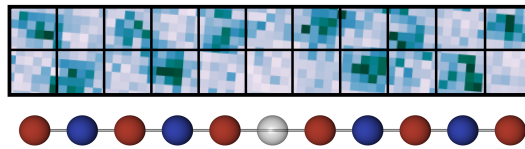


FIGURE 5.6: **Example snapshot of initial state.** A spin and charge resolved image of a sample snapshot showing our starting point of a quenched site in an antiferromagnetic background.

The beam removes a single fermion, with density (charge) 1 and spin $1/2$ from the chain (see Fig. 5.6). When the system is allowed to evolve, two domain walls in the antiferromagnetic chain emerge which propagate outwards from the quenched site (see Fig. 5.7). These two domain walls, which are the spinon and the holon, are characterized by adjacent parallel spins in an antiferromagnetic background and a hole in the unity-filled region respectively.

The experiment is performed for different hold-times after the quench before imaging the distribution. Our quantum gas microscope reveals both the spin and density distributions of the chain, which enables us to locate the position of adjacent parallel spins and holes, which are the signatures of the quasiparticle excitations. To collect statistics, the experiment is repeated several thousand times for a given evolution time.

5.2.1 Holon dynamics

The characteristic signature of a holon propagating in a 1D chain is simply an empty site in an otherwise unity-filled region. Hence, to track the dynamics of holons, we observe the hole density $\langle \hat{n}_i^h \rangle$ distribution (i labels the lattice sites) as a function

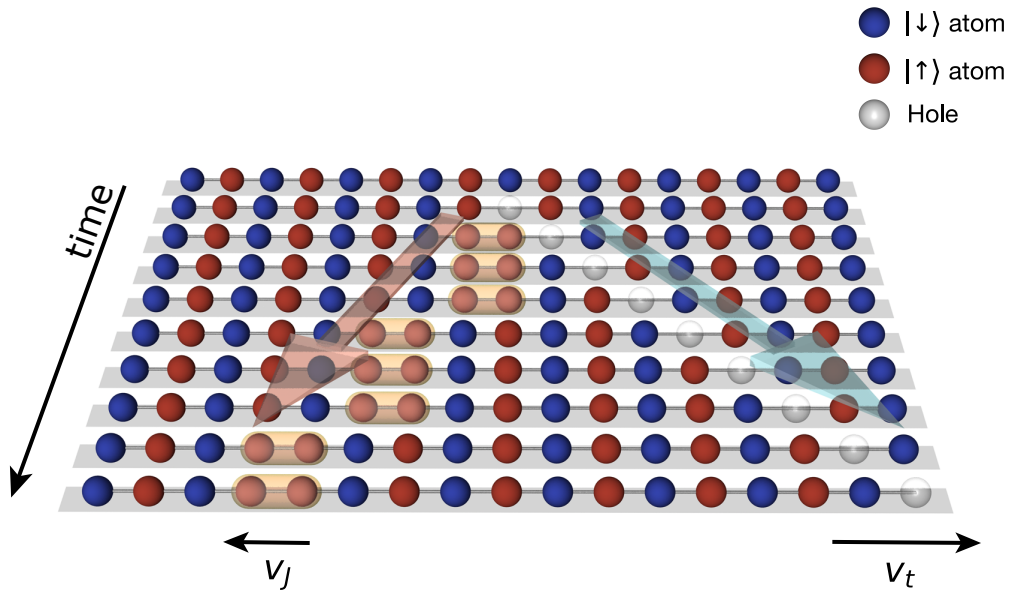


FIGURE 5.7: **Probing spin-charge separation.** The sketch shows the scenario of spin-charge separation as performed in our experiment. The quench creates spin and charge excitations characterized by adjacent parallel spins and a hole respectively, which act as domain walls in the antiferromagnet. These quasiparticle excitations propagate outwards from the site of the quench with velocities v_t for holons and v_j for spinons.

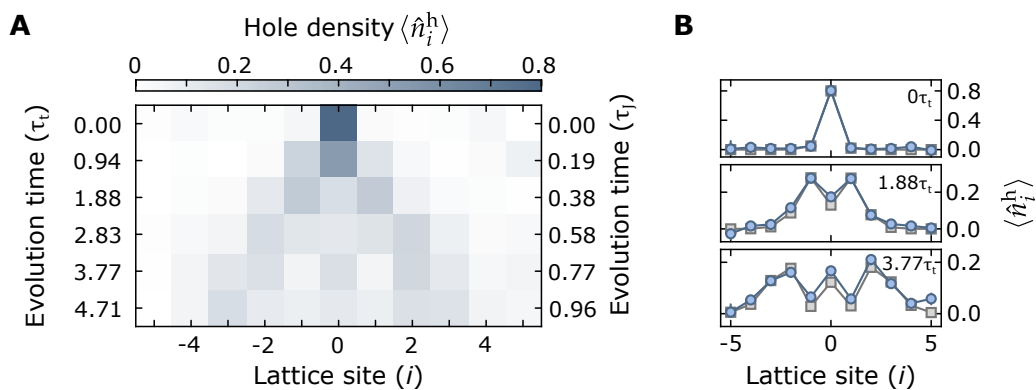


FIGURE 5.8: **Charge excitation dynamics.** **A**, Light-cone-like expansion of hole distribution. Starting at the central site, the distribution broadens until it reaches the edge of the unity-filled region of the chain. **B**, One-dimensional cuts of the hole distribution at different times of evolution and comparison to a single particle quantum walk (grey). Strong interference effects indicative of the coherent dynamics are visible.

of time after the quench, in steps of $300\mu\text{s}$, which is of the order of the tunneling timescale $t_x = 250\text{ Hz}$.

Immediately after the quench, the distribution is peaked at the central site of the chain where the pushout beam is focused to, as expected (see Fig. 5.8). The distribution expands with time and a light-cone-like propagation of the hole density wavefront is visible. It starts from the addressed site and reaches the edge of the unity-filled region of the chain in $5\tau_t$, where $\tau_t = \hbar \times (4\pi t)^{-1} = 0.32\text{ ms}$ is the time it takes for a hole propagating at the theoretically expected maximum group velocity $v_t^{max} = a_x / \tau_t$, to move by one site.

Fig. 5.8 also shows the one-dimensional cuts of the hole density distributions at three different evolution times. The experimental data is compared to a theoretical simulation of the quantum walk of a single particle in a lattice. The excellent agreements indicates that the holon behaves as a particle undergoing a quantum walk independent of the spin environment, as one would expect in a spin-charge separated system. Another interesting feature to note are the interference effects seen in the light cone as well as in the one-dimensional cuts, pointing to the coherent evolution of the holon.

5.2.2 Extraction of holon velocity

Given a light-cone-like propagation of the wavefront, it is straightforward to extract a velocity of the holon. In our case, we monitor the spatial width of the hole density distribution as a function of time. In particular, we use the full width at 30% of maxima of the distributions to quantify the spatial width.

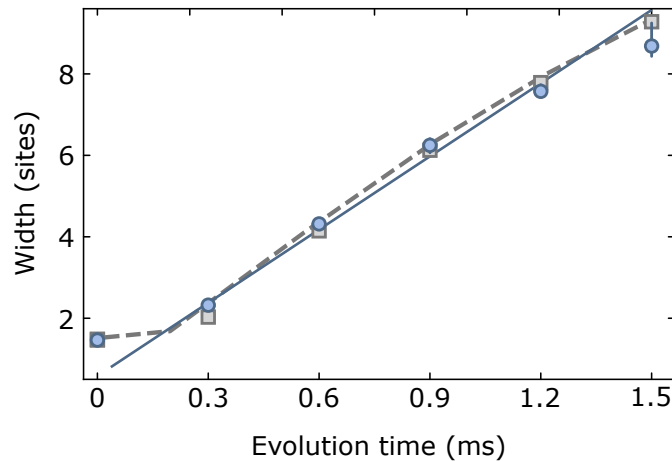


FIGURE 5.9: **Velocity extraction for the charge excitation.** Spatial widths of the hole density distribution as quantified by the full width at 30% of the maxima (blue circles) plotted out as a function of time. The results are compared to a simulation of a single particle quantum walk (grey squares) and predictions of an extended $t - J$ model (grey dashed lines, see text).

The width shows a linear relation to the time of evolution and we use the slope of a linear fit to determine the velocity of the holon (see Fig. 5.9). The holon reaches the edge of the unity-filled region in about 1.5ms. The velocity obtained by this procedure for the holon is then 3.08 ± 0.09 sites/ms.

In addition to the single particle quantum walk, the experimental results are also compared to theoretical simulations of the extended $t - J$ model (see Section 5.3.1) and both are found to be in excellent agreement with our results.

5.2.3 Spinon dynamics

Next we study the dynamics of the spinon, which is characterized by adjacent parallel spins in an antiferromagnetic background. A good observable to detect adjacent spins is the nearest neighbour spin correlator along the chain. We perform the analysis in squeezed space [139, 142] (denoted by \sim), where sites with holes and doublons are removed from the analysis. The nearest neighbour spin correlator in squeezed space is defined as $C_{\tilde{i}}(\tilde{x} = 1) = 4(\langle \hat{S}_{\tilde{i}}^z \hat{S}_{\tilde{i}+1}^z \rangle - \langle \hat{S}_{\tilde{i}}^z \rangle \langle \hat{S}_{\tilde{i}+1}^z \rangle)$. The $C_{\tilde{i}}(\tilde{x} = 1)$ distribution is tracked as a function of time after the quench, in steps of 1.2ms, which is of the order of the spin exchange timescale $J_x = 65\text{Hz}$.

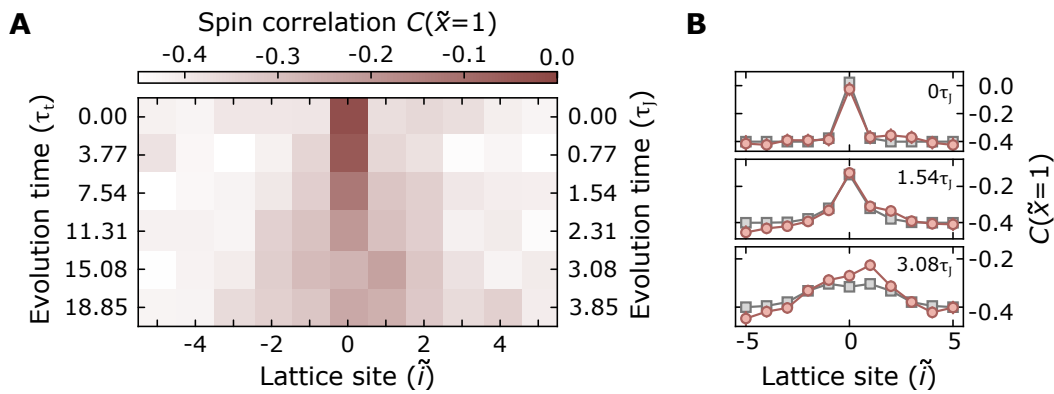


FIGURE 5.10: **Spin excitation dynamics.** **A**, Light-cone-like expansion of $C_{\tilde{i}}(\tilde{x} = 1)$ distribution. Starting in the centre of the chain, the distribution broadens until it reaches the edge of the unity-filled region of the chain in a time of $\tau_J = 3.85$. **B**, One-dimensional cuts of the $C_{\tilde{i}}(\tilde{x} = 1)$ distribution at different times of evolution and comparison to a theoretical simulation of the Heisenberg model (grey).

Immediately after the quench, a strong reduction in the antiferromagnetic correlations is seen in the centre of the chain where the quench was performed (see Fig. 5.10). A reduction in antiferromagnetic correlations is indicative of an enhanced probability of finding adjacent parallel spins characteristic of spinons at that position. The reduced antiferromagnetic correlations spread outwards as a function of time, once again with a light-cone-like propagation of the wavefront. Starting from the centre, the wavefront reaches the edge of the unity-filled region of the chain in $4\tau_J$, where $\tau_J = h \times (\pi^2 J)^{-1} = 1.56\text{ms}$ is the time it takes for a spinon propagating at the theoretically expected maximum group velocity $v_J^{\text{max}} = a_x/\tau_J$, to move by one site.

For the strong interactions $U/t = 15$ in our system, the spin dynamics in squeezed space is expected to be captured by an antiferromagnetic Heisenberg model [117, 145]. In the one-dimensional cuts of the $C_{\tilde{i}}(\tilde{x} = 1)$ distribution, the experimental results are compared to a theoretical simulation of the Heisenberg model.

The highly coherent evolution in the case of the holon is absent in the case of the spinon. This can be explained from the finite temperature of our system $k_B T/J \sim$

0.75 at which the entropy in the spin sector is much higher than in the charge sector. However, even at such “high” temperatures, the Heisenberg model still predicts the observed ballistic wavefront [146, 147]

5.2.4 Extraction of spinon velocity

To extract a velocity for the spinon, we use a similar approach as for the holon. The spatial width of the $C_{\tilde{i}}(\tilde{x} = 1)$ distribution quantified by the full width at 30% maxima is calculated and plotted out as a function of time (See Fig. 5.11). The relation is linear and the slope of a linear fit gives the velocity of the spinon to be 0.58 ± 0.04 sites/ms.

At $k_B T > J$, one expects the spinon to propagate diffusively. However, at our temperature of $k_B T / J \sim 0.75$, the background correlations are strong enough that the ballistic nature (implying a linear expansion of the distribution with time) of the propagation is visible at the wavefronts of the distribution.

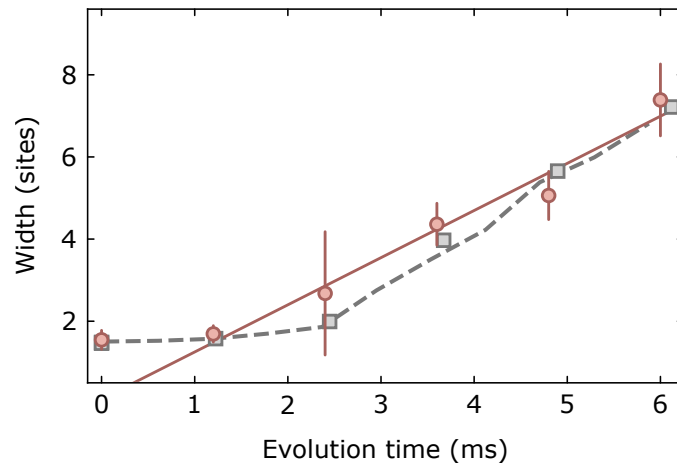


FIGURE 5.11: **Velocity extraction for the spin excitation.** Spatial widths of the nearest neighbour spin correlation $C_{\tilde{i}}(\tilde{x} = 1)$ distribution as quantified by the full width at 30% of the maxima (red circles) plotted out as a function of time. The results are compared to a simulation of the Heisenberg model (grey squares) and predictions of an extended $t - J$ model (grey dashed lines).

The experimental results are also compared to theoretical simulations of the Heisenberg model (see Section 5.3.2) and exact diagonalization calculations of the extended $t - J$ model (see Section 5.3.1) performed at conditions similar to the experimentally realized chains. Despite the finite non-zero temperature in our system, the theoretical simulations agree well with the obtained results.

The measured ratio of the holon and spinon velocities in our experiments is 5.31 ± 0.43 , indicating a vast difference in velocities of the two quasiparticle excitations which emerged from the quench. At the level of a single particle quench, the measured difference in velocities of the spin and charge excitations is a strong indication for spin-charge separation in the chains.

It must, however, be noted that both in the Luttinger liquid regime and beyond, the velocity of a holon need not correspond to a free quantum walk and the velocity of the holon is not always larger than the spinon velocity [75]. As discussed in

Sec. 2.3.3, the velocities of the spin and charge excitations depend on where on the dispersion relation the Fermi level lies. Since the position of the Fermi level depends on the amount of hole doping in the chain and the value of the interaction strength, these parameters can be used to tune the velocities of the excitations.

However, in the timescales we probe in the experiment, the excellent agreement of our results with that of a free quantum walk shows that the wavefunction factorization predicted at $T = 0$ and asymptotically true for $U/t = \infty$ by Woynarovich-Ogata-Shiba [116, 117], is sufficient to capture the essence of our experimental observations at $U/t = 15$.

5.3 Theoretical extraction of velocities

The essential physics of spin-charge separation as observed in our experiments can be captured with relatively simple theoretical methods. We use a modified and extended version of the $t - J$ model discussed in Section 2.1.2 for the analysis. Additionally, for the spinons, we also compare the experimental results to the dynamics expected from the Heisenberg model, which is described in this section.

Regardless of the underlying theoretical model, the extraction of velocities of the holon and spinon quasiparticles in the simulations is done with the same analysis as in the experiment - by calculating the full width at 30% of maxima at different evolution times of the respective distributions, plotting it out as a function of time and extracting the slope.

The extracted velocities agree well with the experimental observations, indicating that there is no need to perform finite temperature DMRG or full Fermi-Hubbard simulations, and the simpler models considered capture the dynamics of the quasiparticles. Nevertheless, we compare the extended $t - J$ simulation results also with simulations of the full Fermi-Hubbard model for 8-site systems and show that the dynamics is almost identical until finite size effects start becoming relevant.

5.3.1 Extended $t - J$ model

The experimental results shown in Fig. 5.9 and Fig. 5.11 are compared to simulations of the extended $t - J$ model (grey dashed lines). The extended $t - J$ model is an approximation of the Fermi-Hubbard model in leading order of t/U , below half-filling [99],

$$\hat{H}_{t-J^*} = \mathcal{P} \left[-t \sum_{\langle i,j \rangle, \sigma} \hat{c}_{i,\sigma}^\dagger \hat{c}_{j,\sigma} + J \sum_j \left(\hat{S}_{j+1} \cdot \hat{S}_j - \frac{\hat{n}_{j+1} \hat{n}_j}{4} \right) - \frac{J}{8} \sum_{\langle i,j,r \rangle, \sigma}^{i \neq r} \left(\hat{c}_{i,\sigma}^\dagger \hat{c}_{r,\sigma j} - \sum_{\sigma', \tau, \tau'} \hat{c}_{i,\sigma}^\dagger \vec{\sigma}_{\sigma, \sigma'} \hat{c}_{r, \sigma'} \cdot \hat{c}_{j, \tau}^\dagger \vec{\sigma}_{\tau, \tau'} \hat{c}_{j, \tau'} \right) \right] \mathcal{P}. \quad (5.1)$$

Here, \mathcal{P} denotes the projection operator on the subspace without double occupancy, and $\langle i, j, r \rangle$ is a sequence of neighbouring sites. The operator $_{j,\sigma}$ creates a

fermion with spin σ on site j and $j = \sum_{\sigma} \hat{c}_{j,\sigma}^{\dagger} \hat{c}_{j,\sigma}$ is the corresponding density operator. The spin operators are defined by $\hat{S}_j = \frac{1}{2} \sum_{\sigma,\sigma'} \hat{c}_{j,\sigma}^{\dagger} \vec{\sigma}_{\sigma,\sigma'} \hat{c}_{j,\sigma'}$, where $\vec{\sigma}$ are the Pauli matrices.

The first two terms define the $t - J$ model as discussed in Section 2.1.2 with a tunneling amplitude t and spin-exchange amplitude $J = 4t^2/U$. For a single hole, the term $\hat{n}_{j+1}\hat{n}_j$ leads to a constant shift in energy.

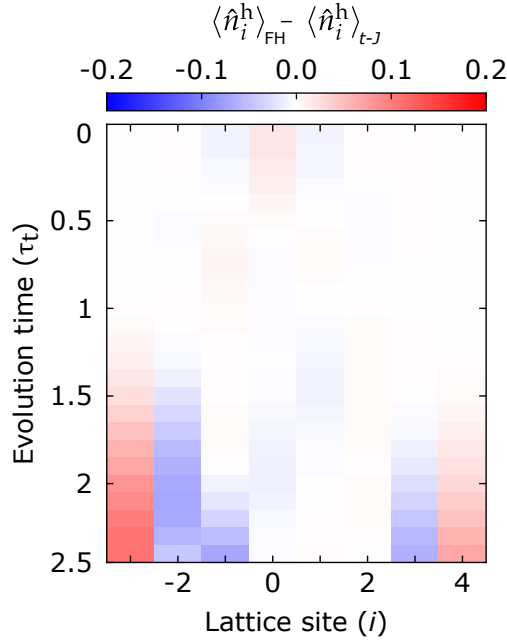


FIGURE 5.12: **Comparison of dynamics in the Fermi-Hubbard and extended $t - J$ model.** The simulation is performed on an 8-site system at $U/t = 15$ following a quench in the central site. The differences are less than 5% until edge effects start to matter. Theory simulations by A. Bohrdt.

The extended $t - J$ model additionally includes a third term, which describes next-nearest neighbour tunneling of holes correlated with spin-exchange interactions.

Furthermore, a confining harmonic confinement for the fermions is included to simulate closer the experimental conditions. This is given by the term:

$$\hat{H}_{\text{pot}} = V \sum_i (x_i/a)^2 \hat{n}_i, \quad (5.2)$$

where x_i is the distance of site i from the center of the chain and $V/J = 0.46$.

The experimental results presented in this chapter are compared to exact diagonalization calculations of the extended $t - J$ model with a single hole. The conservation of the z component of the total spin is used to obtain a block diagonal Hamiltonian.

Later in the chapter, we use multi-point correlators to further demonstrate the spatial separation of the spin and charge excitations. The comparison to these results (shown in Fig. 5.21) are evaluated by numerically generating snapshots with probabilities given by the time evolved density matrix.

To show the validity of the extended $t - J$ model, we directly compare the light cones generated with the extended $t - J$ model to a full Fermi-Hubbard simulation of 8 sites at $U/t = 15$ after quenching the central site. In the comparison, shown in Fig. 5.12, the difference in the dynamics of the holon is less than 5% in the initial dynamics until the finite size effects start to matter. Since the velocity extraction of the quasiparticles is based on their initial dynamics, it is no surprise that the extended $t - J$ model is sufficient to explain our results.

5.3.2 Heisenberg model for the spinons

In the case of the spinon, the quasiparticle velocity is extracted numerically by measuring the width of the nearest neighbour correlator light-cone at 30% of the maximum value, the technique identical to the description earlier for the experimental results.

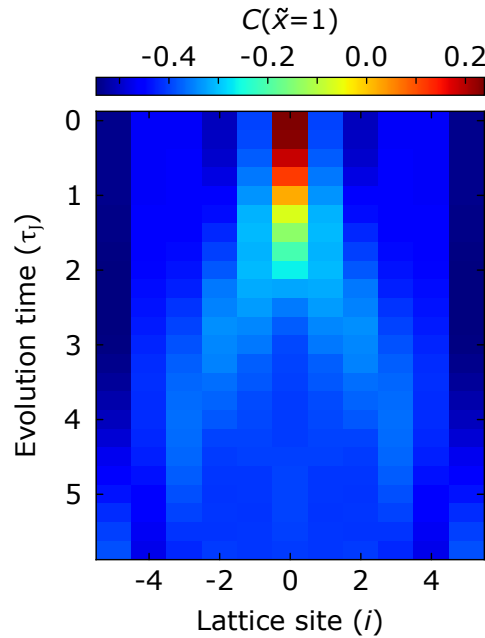


FIGURE 5.13: **Light cone of spinon propagation with open boundary conditions for the spin.** Open boundary conditions for the spin lead to strong boundary effects which make it difficult to extract a quasiparticle velocity reliably. Theory simulations by A. Bohrdt.

However, for temperatures $T \leq J$, the open boundary conditions have a strong effect on the squeezed space nearest neighbour correlator $C(\tilde{x} = 1)$. The spin at the boundary is only coupled to one other spin, such that the corresponding correlations are stronger on every second bond in the vicinity of the edge. This boundary effect is visible throughout the spin chain in squeezed space, as shown in Fig. 5.13. This makes the extraction of a spinon velocity with the method described above challenging.

We therefore use periodic boundary conditions for the spins in the simulation, whereas the hole is still subject to open boundary conditions and the harmonic potential described above. This leads to a smooth behavior of the squeezed space

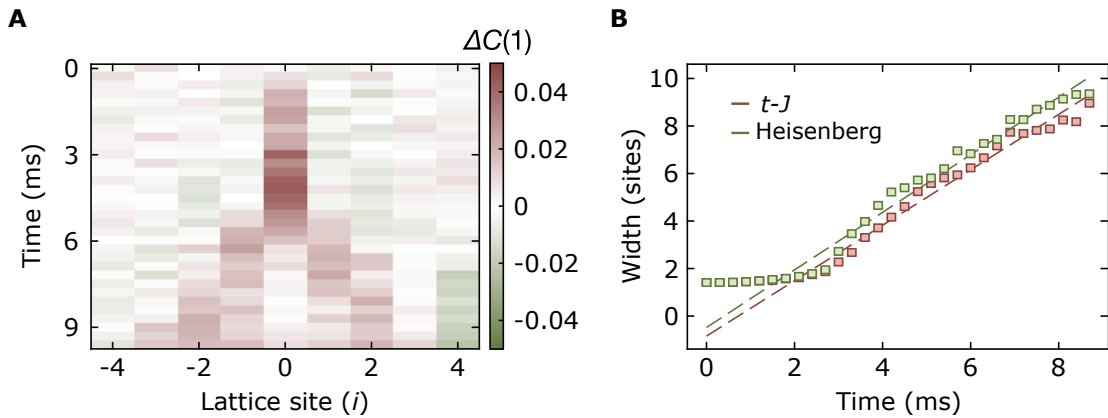


FIGURE 5.14: **Comparison between the extended $t - J$ and Heisenberg models for $t/J = 3.8$, $T/J = 0.7$ and $V/J = 0.456$.** **A**, Difference between the squeezed space nearest neighbour correlator distribution in the extended $t - J$ model and the Heisenberg model $\Delta C(1)$. **B**, Velocity extraction for the spinon in the simulation of the extended $t - J$ model (red squares) and the Heisenberg model (green squares). The extracted velocities of 0.58 ± 0.04 sites/ms for the extended $t - J$ model and 0.61 ± 0.05 sites/ms for the Heisenberg model are obtained by fitting a straight line to the points (dashed lines).

$C(\tilde{x} = 1)$ correlator and therefore enables the extraction of the spinon velocity, which we use in Fig. 5.10 (grey).

The spin dynamics in the extended $t - J$ model after the creation of a hole can be directly compared to a Heisenberg spin chain, where initially one site is removed. Since in the latter case no hole is involved, the comparison between the two simulations directly yields insights into the effect of the hole on the spin dynamics.

In Fig. 5.14, the relative difference between the squeezed space $C(\tilde{x} = 1)$ correlations for the extended $t - J$ and Heisenberg model are shown. Apart from the initial dynamics on the central bond, the relative difference is below 8% during the entire time evolution, showing how similar the spinon dynamics are in the two simulations.

5.4 Spatial separation of spin and charge excitations

An important consequence of spin-charge separation is the absence of any bound states between the holons and the spinons. Having shown that these two quasiparticle excitations propagate at different velocities, is there a way to prove the absence of binding between them?

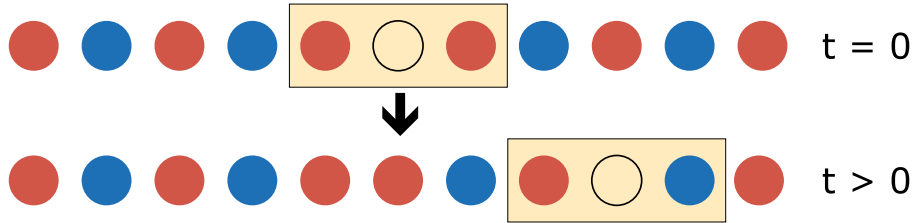


FIGURE 5.15: **Decoupling of spin and charge excitations.** Binding between the spin and charge degrees of freedom would lead to the holon dragging the spinon with it. However, in a truly spin-charge separated system, as depicted in the cartoon above, at any finite time in the evolution after the quench, the holon gets rid of the spinon and becomes surrounded by opposite spins.

In this section, we make use of the ability of our quantum gas microscope to evaluate multi-point correlators in a single snapshot to prove the spatial separation of the holons and spinons.

In particular, we will measure the spin correlations across a hole and track it as a function of time, to show the absence of binding at the level of the nearest neighbour. We will then use the normalized deviation from the mean nearest neighbour correlator to show the absence of binding at any distance in the chain, beyond the immediate vicinity of the holon.

5.4.1 Tracking spin correlations across a hole

In chains exhibiting Néel order the hole at the quenched site would be surrounded by parallel spins immediately after quench, as illustrated in Fig. 5.15.

In case of binding between spinons and holons, the holon would drag the spinon with it as it propagates through the chain. However, in a spin-charge separated system, the dynamics of the holon is completely independent of the spinon. In such systems, after a propagation time of a few tunneling timescales, one would expect the holon to have gotten rid of the spinon and be surrounded by opposite spins instead.

In our Fermi-Hubbard chains at a finite temperature of $k_B T / J \sim 0.75$, we would expect the correlations across the hole to actually approach the background mean nearest neighbour correlations of the system in the absence of a quench, after longer times of evolution.

Access to multi-point correlators in every single shot enables us to measure precisely the correlation across a hole in our Fermi-Hubbard chains. We use the spin-hole-spin correlator $C_{\text{SHS}}(2) = 4 \langle \hat{S}_i^z \hat{n}_{i+1}^h \hat{S}_{i+2}^z \rangle$, which measures the spin correlation between two atoms at sites i and $i+2$ conditioned on having a hole in between them at site $i+1$.

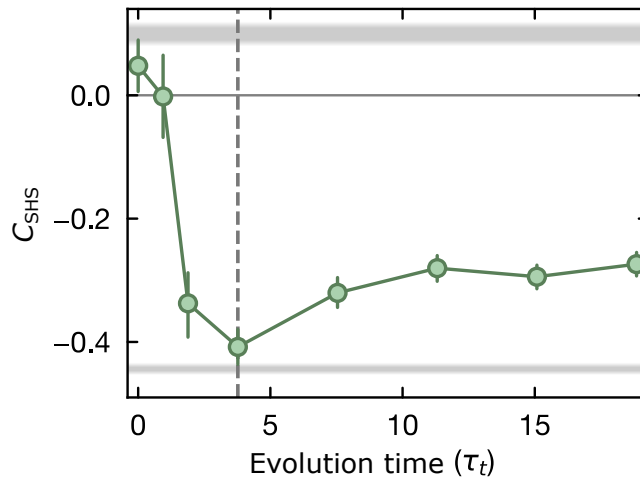


FIGURE 5.16: **Spatial separation of spin and charge excitations.** Spin-hole-spin correlations (C_{SHS}) averaged over the entire chain as a function of time after the quench. The correlator starts with a positive value consistent with the next-nearest neighbour spin correlations $C(2)$ in the absence of the quench (top grey shaded region) and turns negative, approaching the nearest neighbour spin correlations $C(1)$ without the quench (bottom grey shaded region) by $4\tau_t$. The vertical dashed line indicates the time at which the hole and parallel adjacent spin distributions are maximally separated. At longer evolution times, the correlator shows reduced antiferromagnetic correlations due to the oscillating dynamics of the hole in our finite size system (see text and Fig. 5.17).

Immediately after the quench ($\tau_t = 0$), the hole is likely to be surrounded by parallel spins and C_{SHS} retains a positive value, as shown in Fig. 5.16. The measured spin correlations are consistent with the next-nearest-neighbour correlations $C(2) = 4(\langle \hat{S}_i^z \hat{S}_{i+2}^z \rangle - \langle \hat{S}_i^z \rangle \langle \hat{S}_{i+2}^z \rangle)$ in the absence of the quench.

As the hole propagates, the sign of C_{SHS} becomes negative and by $4\tau_t$, approaches the nearest neighbour correlations $C(1) = 4(\langle \hat{S}_i^z \hat{S}_{i+1}^z \rangle - \langle \hat{S}_i^z \rangle \langle \hat{S}_{i+1}^z \rangle)$ without the quench. This indicates the absence of binding between the two quasiparticles in the vicinity of the holon.

At longer times of evolution, the correlations across the hole rise to become more ferromagnetic. The origin of this effect is the finite size of our chains due to the harmonic confinements which leads to an artificial overlap of the holon and spinon distributions, as we shall see in the next section.

5.4.2 Overlap of holon and spinon distributions

The effect by which C_{SHS} becomes less antiferromagnetic after longer evolution times is attributed to the holon oscillating in the chain due to the harmonic confinement present in our system and hence to the changing overlap of the spin and charge distributions. Fig. 5.17 shows the longer time-dynamics of the holon and its overlap with the spinon distribution.

At the time of the quench, both the hole density distribution and the nearest neighbour correlation distributions are peaked at the center of the chain. However,

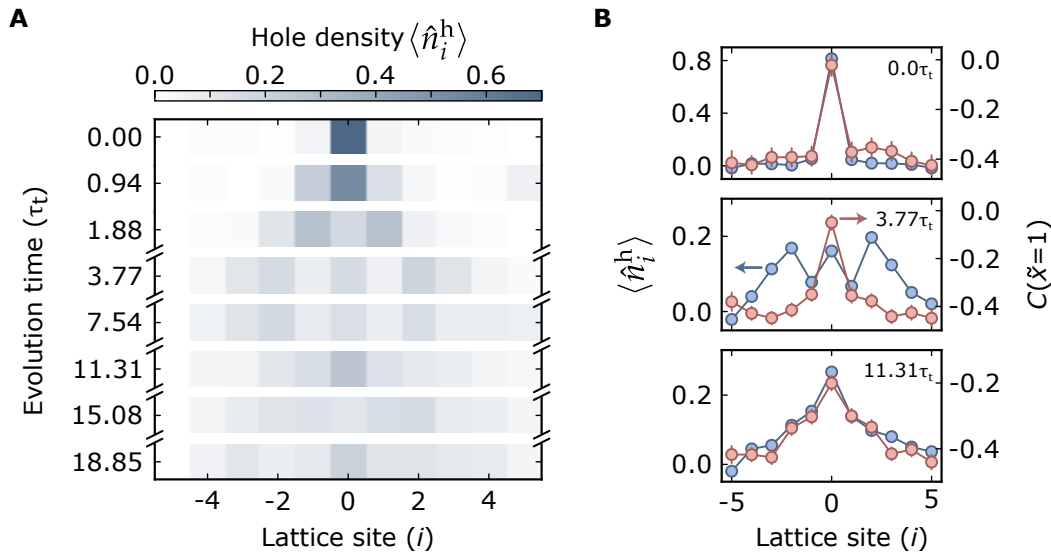


FIGURE 5.17: **Effect of harmonic confinement on hole dynamics.** **A**, Hole density $\langle \hat{n}_i^h \rangle$ distribution at longer evolution times than it takes to reach the edge of the chain. The hole distribution spreads out and then oscillates back to the center of the chain after $11.31 \tau_t$ and later again after $18.85 \tau_t$ owing to the harmonic confinement in our system. **B**, The oscillatory behaviour of the holon changes the overlap of the hole distribution (blue) with the nearest neighbour spin correlation $C(\tilde{x} = 1)$ distribution (red), shown for three different time slices. The arrows indicate the respective y -coordinates. Error bars denote 1 s.e.m.

after a few tunneling events, the holon reaches the edge of the chain whereas the nearest neighbour correlation distribution is still peaked at the center, leading to a maximal separation between the two distributions.

In its longer-time dynamics, the holon does not leave the chain, but rather bounces back to the centre of the chain. Two such “revivals” can be seen in the duration in which we probe the dynamics. This introduces an artificial overlap of the hole density and nearest neighbour correlator distributions.

Consequently, there is an increased probability of instances where parallel spins appear across the hole, leading to an increased ferromagnetic signal away from the mean $C(1)$ across the hole at longer times.

5.4.3 Absence of binding beyond the nearest neighbor

Evaluating the spin-hole-spin correlator at different times showed that the charge excitation does not drag the spin excitation with it upto the nearest neighbour. To prove the absence of binding beyond the immediate vicinity of the hole, we have to show that the spin correlations between two sites remains unchanged, independent of the position of the hole in the chain. This would imply that the dynamics of the holon is completely decoupled from the spin environment - a direct consequence of spin-charge separation.

To this end, we calculate the normalized deviation from the mean nearest neighbour correlations, defined as:

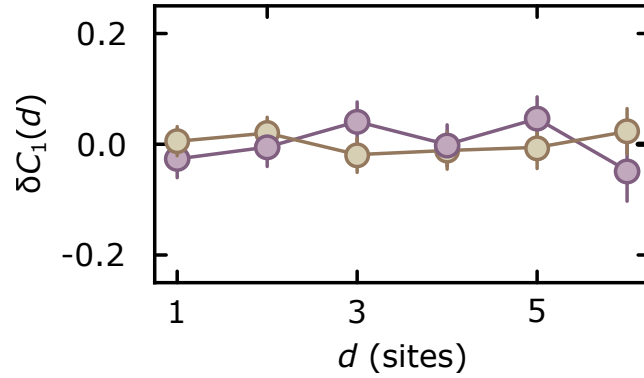


FIGURE 5.18: **Fluctuations in $C(1)$ at longer distances.** The lack of dependence of the normalized deviation from the mean nearest neighbour correlations δC_1 on the distance d from the hole at times $\sim 4\tau_t$ (purple) and $\sim 19\tau_t$ (yellow). Error bars denote 1 s.e.m.

$$\delta C_1(d) = \left\langle \frac{\hat{S}_i^z \hat{S}_{i+1}^z}{\langle \hat{S}_i^z \hat{S}_{i+1}^z \rangle} - 1 \right\rangle_{\bullet_i \bullet_{i+1} \circ_{i+1+d} \vee i-d} \quad (5.3)$$

where d is the distance of the hole from the closest of sites i and $i+1$, full circles representing single atoms and empty circle representing the hole. The deviation is zero when the spin correlations between any two sites, conditioned on detecting a hole at a distance from the closest of the two sites, is the same as the mean nearest neighbour correlator at that site.

As can be seen from Fig. 5.18, the normalized deviation does not show any dependence on d , for data analyzed at two different times ($t = 4\tau_t$ and $t = 19\tau_t$). The flatness of the lines indicate the lack of influence of the holon on the spinon even at longer distances beyond the nearest neighbour in the chain.

5.5 Connection to spin-charge fractionalization

Assuming a perfect quench (100% probability to remove an atom from the targeted site without affecting the neighbouring sites), the amount of excess density or charge carried by the holon is exactly equal to 1 (in units of e). Similarly, the amount of excess spin carried by the spinon should be exactly equal to 0.5.

This is the picture of spin-charge fractionalization, where an electron-like quench in the chain fractionalizes into a holon carrying charge $1 e$ and a spinon carrying spin 0.5. However, as we shall discuss in this section, this picture of fractionalization is valid only at zero temperature. At higher temperatures, fluctuations in the charge and spin sectors lead to a reduction in the measured value of charge (spin) carried by the holon (spinon).

Starting with an cartoon example depicting fractionalization at zero-temperature, the tool we use to quantify the spin excitation in or chains - an envelope function that captures the location and magnitude of spin of the spinon - will be described. We will then look at the scenario more relevant to our experiment - fractionalization at non-zero temperature - and see how the temperature plays a key role in the observed signal for the excess spin carried by the spinon.

5.5.1 Fractionalization at zero temperature

Before quantifying the spin excitation in our finite non-zero temperature chains, it is helpful to discuss the zero temperature scenario, in the absence of charge or spin fluctuations. Such chains, as visualized in the cartoon in Fig. 5.19A, have alternating up and down spins. There are no domain walls such as parallel spins or empty sites, which are characteristic of spinons and holons, in this chain.

However, as soon as a perfect electron-like quench is performed, two domain walls emerge and separate after a few tunneling events (as in Fig. 5.19B) - the spinon and the holon. Now, there is a spinon in the system which carries the excess spin from the quench.

To quantify this excess spin, we use an envelope function which measures the spin fluctuations locally:

$$\hat{\Sigma}_{\tilde{j}}^2 = \left(\sum_{\tilde{i}} \hat{S}_{\tilde{i}}^z f_{\tilde{j}}^{\sigma}(\tilde{i}) \right)^2 \quad (5.4)$$

where $f_{\tilde{j}}^{\sigma}(\tilde{i}) = e^{-\frac{(\tilde{i}-\tilde{j})^2}{2\sigma^2}}$ is a smooth window function centered at lattice site \tilde{j} with a characteristic size of σ . This operator, which sums up the spins within the envelope and squares the result, is expected to capture local fractional quantum number at zero temperature [148].

In the absence of a quench, when there are no spinons present, the operator is zero everywhere in the chain. However, when evaluated across the chain after a quench, $\langle \hat{\Sigma}_{\tilde{j}}^2 \rangle$ increases to a value of $\Delta_{T=0} = 0.25$ at the site where a single spinon is located, provided that the mean distance between thermal spin fluctuations is larger than σ .

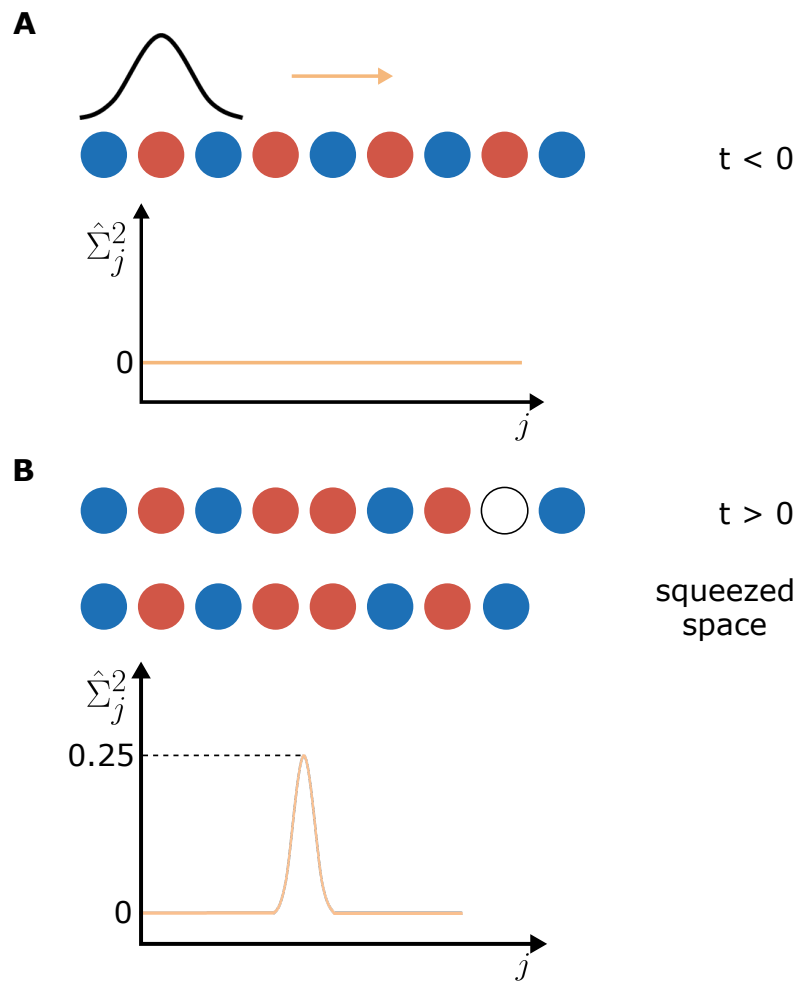


FIGURE 5.19: **Quantifying the spin excitation in the absence of fluctuations.** **A**, An envelope function (defined in text), evaluated continuously across the chain, would give a value of zero in a chain of alternating spins. **B**, If a fermion were to be removed from a chain as in (A), it would lead to the formation of a spinon and a holon. In squeezed space, the envelope, evaluated across the chain, would peak to a value of 0.25 at the location of the spinon.

5.5.2 Fractionalization at non-zero temperature

With the working of the operator and the expected results at zero temperature in mind, we can now look at the result obtained at a finite temperature of $k_B T/J = 0.75$ in our system.

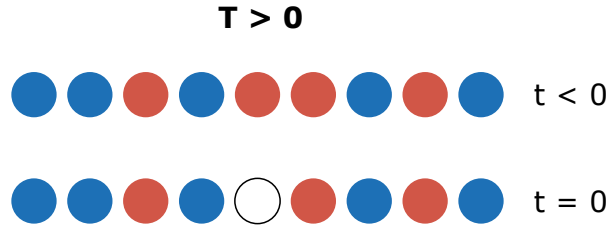


FIGURE 5.20: **Thermal spin fluctuations reduce the efficiency of local spinon creation.** At finite non-zero temperature, a background density of thermal spinons gives rise to scenarios where the quench does not create a local spinon.

The main effect of temperature on the system is the introduction of thermal fluctuations in both the spin and the charge sector. At our temperatures, where we prepare Mott insulators, the fluctuations in density (charge) are highly suppressed and most of the entropy lies in the spin sector. This means that even though we prepare chains with close to unity filling per site, the spin distribution is far from the perfect antiferromagnetic ordering assumed in the discussion in the previous section.

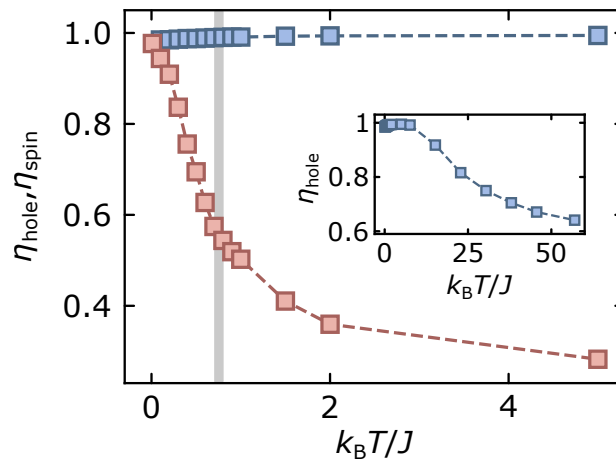


FIGURE 5.21: **A, Local creation efficiency of the quasiparticles** Efficiency of initially creating at the central site a single local spinon η_{spin} with $\sigma = 1.5$ sites (orange) and holon η_{hole} (blue) after an ideal quench as a function of temperature as predicted from theoretical calculations. Our experimental temperature of $k_B T/J = 0.75$ is indicated by the grey shaded region. The local creation efficiency of the spinon rapidly decreases with temperature and is about 56% at the temperatures realized in our experiments. The local creation efficiency of the holon is close to unity until $\sim 10k_B T/J$, after which it starts decreasing (see inset).

Due to these thermal spin fluctuations, there are many realizations of chains where there already are spinons present prior to the quench (see Fig. 5.20), which could be randomly distributed throughout the chain. Hence, performing a quench need not necessarily lead to the formation of spinons.

Therefore, the efficiency of creating a local holon, defined as $\eta_{\text{hole}} = 1 - \langle (\hat{n}_{i=0} - 1)^2 \rangle$, and a local spinon, defined as $\eta_{\text{spin}} = 4(\langle \hat{\Sigma}_{\tilde{j}=0}^2 \rangle - \langle \hat{\Sigma}_{\tilde{j}=0}^2 \rangle_{\text{BG}})$ at the quenched site is dependent on temperature. Here, *BG* refers to the corresponding values in a dataset where no quench is performed.

Fig. 5.21 shows precisely the dependence of the holon and spinon creation efficiency as a function of temperature. It is based on a theoretical simulation of the Hubbard model for the holon and exact diagonalization calculations of the Heisenberg model for the spinon.

At our temperature, the efficiency of creating a holon is close to unity due to the highly suppressed density fluctuations whereas the efficiency of creating a spinon is rather low at $\sim 56\%$. This means that in close to 44% of our experimental runs, no spin excitation is created by the quench. At higher temperatures, the effect of the thermal fluctuations on the density sector also becomes apparent (5.21, inset).

The reduced efficiency of spinon creation in our experiments has a direct consequence on the measured excess spin carried by the spinon. Once again, the envelope function $\langle \hat{\Sigma}_{\tilde{j}}^2 \rangle$ as defined earlier is used.

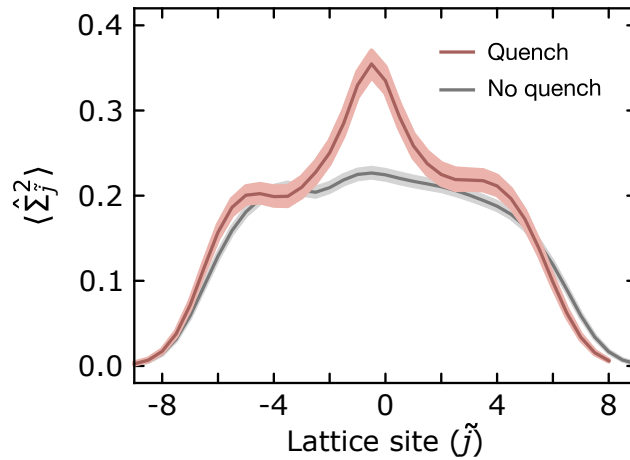


FIGURE 5.22: **Envelope analysis.** Spatially resolved magnetization fluctuations $\langle \hat{\Sigma}_{\tilde{j}}^2 \rangle$ in sub-regions of the chain with (red) and without (grey) the quench at $3.77\tau_t$.

When evaluated across the chain at $t = 3.77\tau_t$ and averaged over the dataset, the spatial dependence of $\langle \hat{\Sigma}_{\tilde{j}}^2 \rangle$ is shown in Fig 5.22. Unlike the case at zero temperature, the most apparent difference is the presence of strong background fluctuations. These background fluctuations, denoted by $\langle \hat{\Sigma}_{\tilde{j}}^2 \rangle_{\text{BG}}$, are due to quantum and thermal fluctuations in our chain.

In the absence of a quench, the background fluctuation value has a plateau that stretches across the unity-filled region of the chains. The signature of the spinon created by the quench is seen from the peak in the central sites of the chain, when the envelope function is evaluated over a dataset in which the quench was performed.

The first point to note is that this analysis was performed at an evolution time of $t = 3.77\tau_t$, and only chains which had a single hole that was located outside the central three sites were chosen.

At $t = 3.77\tau_t$, such chains occur in a majority of experimental runs as the holon probability is peaked at the edges of the unity-filled region of the chain (see Fig. 5.8). The resulting peak in the excess spin in 5.22 is a direct consequence of spin-charge separation - the peak in the distribution of the excess spin carried by the spinon is spatially separated from the peak in the distribution of the excess density (charge) carried by the holon.

The second and more important point in relation to fractionalization is the difference in amplitude of the envelope operator in the presence and absence of the quench. This difference, $\langle \hat{\Sigma}_{\tilde{j}}^2 \rangle - \langle \hat{\Sigma}_{\tilde{j}}^2 \rangle_{\text{BG}}$, is nothing but the excess spin carried by the spinon.

Whereas at zero temperature, we saw that this value is $\Delta_{T=0} = 0.25$, here we measure a value of $\Delta_{T=0.75J} = 0.13 \pm 0.01$. This measured value of $\Delta_{T=0.75J}$, which is about half of $\Delta_{T=0}$ is consistent with the spinon creation efficiency of 56%.

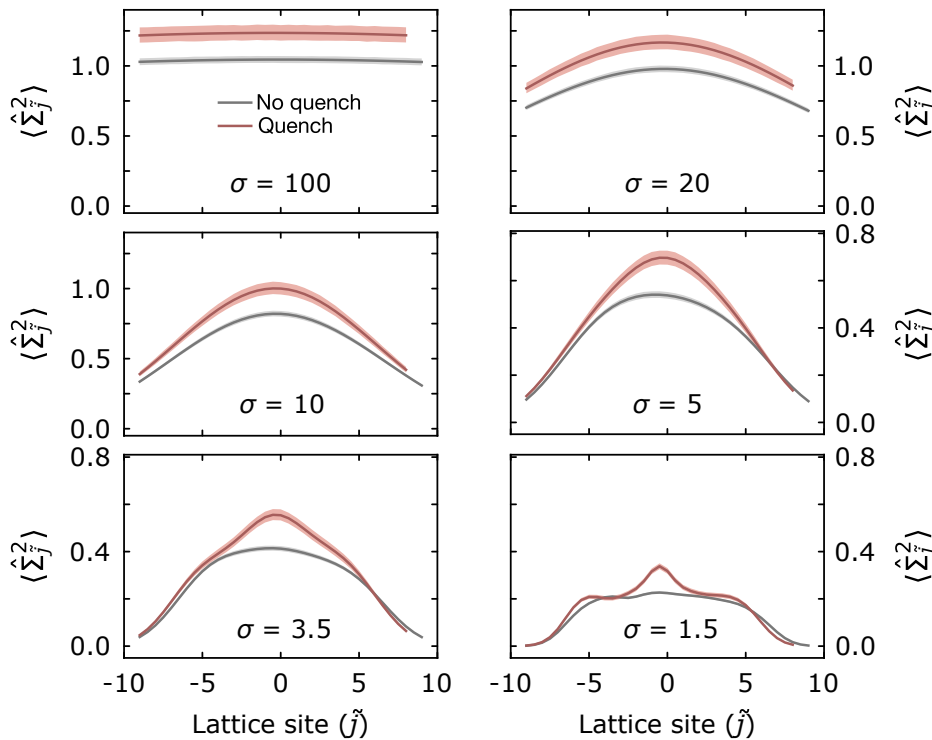


FIGURE 5.23: **Evaluation of spatially resolved magnetization fluctuations $\hat{\Sigma}_{\tilde{j}}^2$ centered at $\tilde{j} = 0$ for different envelope sizes σ .** By comparing datasets with (red) and without (grey) the quench, a large σ can be used to extract the total magnetization fluctuation in the chain and a small σ can be used to determine the spatial extent of the spin excitation. Grey and red shades indicate 1 s.e.m. without and after the quench respectively.

Regardless of whether the quench creates a local spinon or not, it still removes a

fermion with density (charge) 1 (e) and spin 1/2, creating charge and spin excitations. These spin excitations are local around the target site of the quench in case the spinon was created locally. However, in the case of a spinon already being present at the target site at the moment of the quench due to thermal spin fluctuations, the spin excitations are created non-locally somewhere in the chain.

Hence, in principle, by increasing the width of the envelope function to cover the entire chain, we should be able to recover the excess spin value of 1/2, which would correspond to $\langle \hat{\Sigma}_{\tilde{j}}^2 \rangle = 0.25$. The dependence of the envelope width on the measured value of $\langle \hat{\Sigma}_{\tilde{j}}^2 \rangle$ is shown in Fig. 5.23.

When σ is larger than the system size, the operator yields the total magnetization fluctuations in the chain. As σ is reduced, the spatial extent of the spin fluctuations can be located with better resolution.

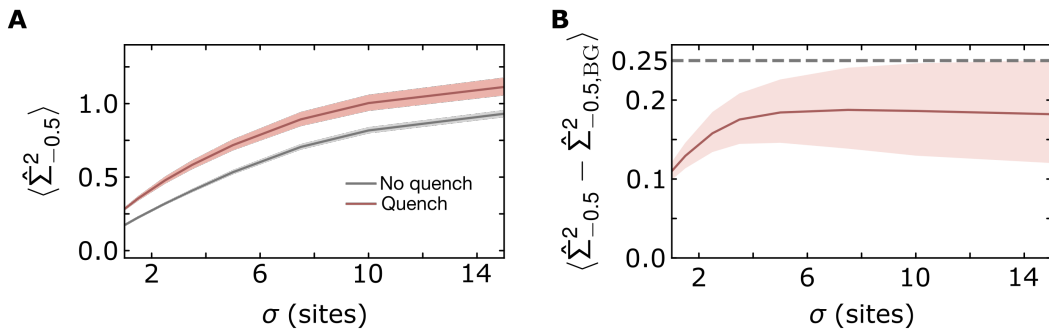


FIGURE 5.24: **Extraction of excess spin carried by the spin excitation.** **A**, The maximum value of $\hat{\Sigma}^2$ evaluated at $\tilde{j} = -0.5$ as a function of σ with (red) and without (grey) the quench. **C**, Maximum deviation $\hat{\Sigma}_{-0.5}^2 - \hat{\Sigma}_{-0.5, BG}^2$ obtained by subtracting the two curves in **B**. At σ larger than system size, the measured deviation approaches 0.19 ± 0.06 . Grey and red shades indicate 1 s.e.m. without and after the quench respectively.

The exact value of the magnetization fluctuations caused by the spin excitation from the quench is given by the difference between the values of $\langle \hat{\Sigma}_{\tilde{j}}^2 \rangle$ obtained in the presence and absence of the quench $\langle \hat{\Sigma}_{\tilde{j}}^2 \rangle - \langle \hat{\Sigma}_{\tilde{j}}^2 \rangle_{BG}$. Plotted in Fig. 5.24, the difference between the values increases as a function of σ and approaches a value of 0.19 ± 0.06 for an envelope size larger than the chain length.

The reason for the increase in the value of the magnetization fluctuations caused by the spin excitation with the envelope width is that a larger envelope captures spinons that were not created locally during the quench. This is why values greater than 0.13 ± 0.01 can be obtained with larger σ , even though the efficiency of creating local spinon from the quench is only 56%.

In principle, once the envelope width is increased to cover the system size, if we really do remove a single fermion with spin 1/2 in every run of the experiment, we expect to measure the excess spin of 0.25. However, our quench is imperfect and the measured deviation of 0.19 ± 0.06 is in agreement with the ideally expected value of 0.25 when taking into account the fidelity of our experimental quench.

5.6 Extracted velocity dependence on t and J

All the results described in this chapter so far were based on chains prepared at $U/t_x = 15$, with $t_x/h = 250\text{Hz}$ and $J_x/h = 65\text{Hz}$. We saw that the velocities extracted for the quasiparticles can be related to the maximum expected group velocities of $v_t^{max} = \pi^2 J a_x / h = a_x / \tau_t$ for the holon and $v_J^{max} = 4\pi t a_x = a_x / \tau_J$ for the spinon. In this section, we will investigate how the extracted velocities depend on the inherent timescales in the system defined by the lattice parameters.

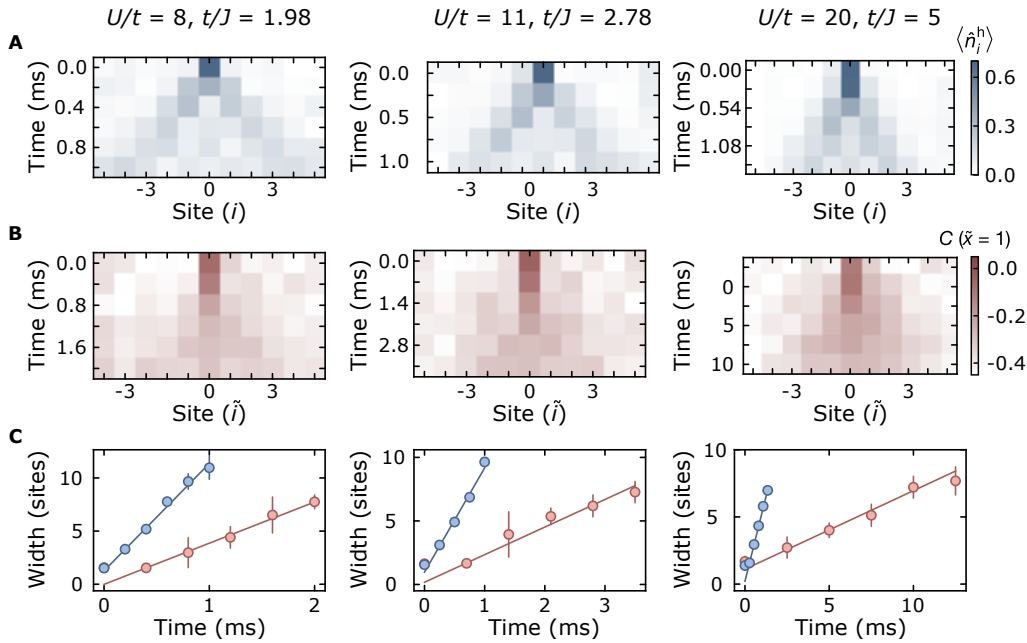


FIGURE 5.25: **Spin and charge dynamics at different lattice depths.** **A**, The time-resolved hole density $\langle \hat{n}_i^h \rangle$ distributions (top), **B**, nearest neighbour spin correlation $C(\tilde{x} = 1)$ distributions and **C**, their spread as a function of time at $U/t = 8$ (left), $U/t = 11$ (middle) and $U/t = 20$ (right). Slope of solid blue (red) lines gives the velocity of the holon (spinon). Error bars denote 1 s.e.m.

To study the scaling of the quasiparticle velocities with the inherent tunneling and spin exchange timescales, we now prepare systems with different U/t_x . By ramping up the x -lattice to $[5 E_R, 6 E_R \text{ and } 8 E_R]$, we prepare chains with $t_x = h \times [410 \text{ Hz}, 320 \text{ Hz and } 190 \text{ Hz}]$, $J_x = h \times [207 \text{ Hz}, 115 \text{ Hz and } 38 \text{ Hz}]$ and $U/t = [8, 11 \text{ and } 20]$. A total of 15497 snapshots are used in the analysis at $U/t = 8$, 11806 at $U/t = 11$ and 9848 at $U/t = 20$.

The same analysis as for the case of $U/t = 15$ as described earlier in the chapter is used to extract the velocities of the quasiparticles in these different scenarios. The hole and nearest neighbour spin correlation distributions in squeezed space are imaged after appropriate times of evolution. For the squeezed space analysis, sites with holes or doublons in the central nine sites are removed, except for nearest neighbour doublon-hole pairs.

Light-cone-like propagation of the holon and spinon wavefronts are visible, as shown in Fig. 5.25. The full width at 30% of maxima of these distributions are calculated and plotted out as a function of time. The slope to a linear fit of these datapoints gives the velocity of the quasiparticles.

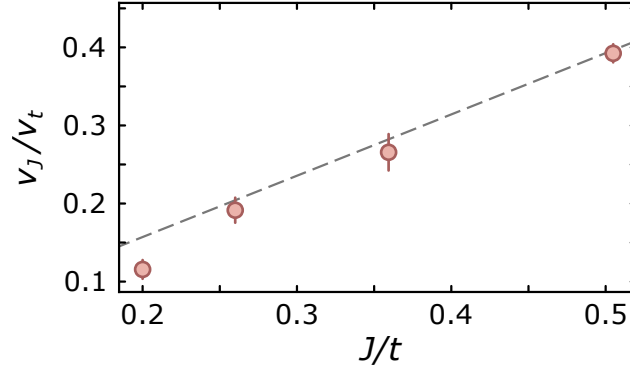


FIGURE 5.26: **Ratio of quasiparticle velocities as a function of J/t .** The extracted ratio of velocities at $J/t = 0.2, 0.26, 0.36$ and 0.5 corresponding to $U/t = 20, 15, 11$ and 8 respectively increase linearly with J/t . Grey dashed line shows the dependence of the ratio v_J^{\max}/v_t^{\max} on J/t . Grey shade indicates an uncertainty in the estimation of t of 5%. Error bars denote 1 s.e.m.

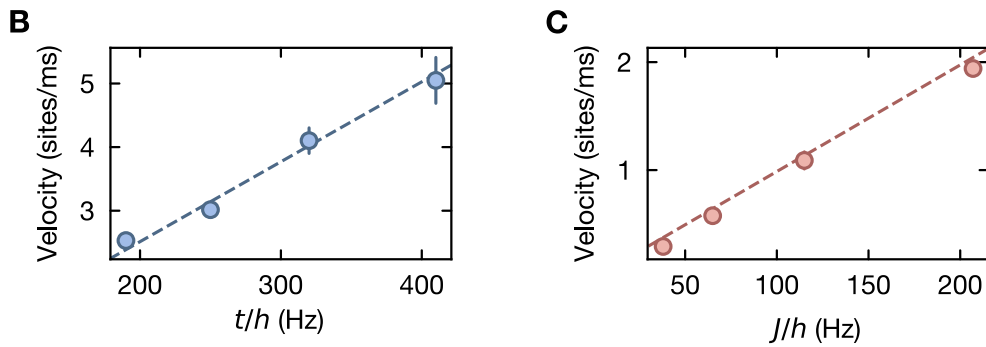


FIGURE 5.27: **Quasiparticle excitation velocities as a function of t/h and J/h .** **B**, Holon velocities as a function of t/h . The velocities of the holon (blue circles) increase linearly with the tunneling rate in the chain, consistent with $v_t^{\max} = 4\pi t a_x/h$ sites/ms (blue dashed line). **C**, Spin excitation velocities as a function of J/h . The velocities of the spin excitation (red circles) increase linearly with the spin-exchange coupling in the chain, consistent with $v_J^{\max} = \pi^2 J a_x/h$ sites/ms (red dashed line). Error bars denote 1 s.e.m.

In each case, we see a difference in velocity between the holon and the spinon. This difference in the ratio of quasiparticle velocities is linked to the ratio of t_x and J_x in the system. In Fig. 5.26, the ratio of spinon and holon velocities v_J/v_t is plotted as a function of J/t and it shows the linear relation between the two quantities.

We further look at the scaling of the measured holon velocities as a function of the tunneling timescales and the measured spinon velocities as a function of the spin exchange timescales. In the entire range of lattice parameters we probe, a linear relation between the holon velocity and t_x and the spinon velocity and J_x is observed, as shown in Fig. 5.27. This is because we track the wavefront of the distributions which corresponds to the fastest mode of the excitations. The fastest modes move at the maximum group velocities of $v_t^{\max} = \pi^2 J a_x / h = a_x / \tau_t$ (holon) and $v_J^{\max} = 4\pi t a_x = a_x / \tau_J$ (spinon), which share a linear relation with t_x and J_x .

5.7 Conclusion

The results presented in this chapter correspond to the first time- and space-resolved observation of the dynamics of spin and charge excitations in the (one-dimensional) doped Fermi-Hubbard model. They demonstrate the curious phenomenon of spin-charge separation following a local quench.

The emergent quasiparticles are tracked with our quantum gas microscope and their velocities are measured and found to be significantly different, leading to their spatial separation after a few tunneling times.

We also discuss the meaning of fractionalization in systems at finite non-zero temperatures. A similar dynamical protocol can be extended to 2D systems as well, to study the time-resolved dynamics of a dopant in a 2D Fermi-Hubbard antiferromagnet. The resultant dynamics is expected to be strikingly different in dimensions greater than one, where a breakdown of spin-charge separation is expected.

Chapter 6

Crossing over from one to two dimensions

In the results for 1D Fermi-Hubbard chains from the previous chapters, we saw that the charge and spin modes are decoupled and can move through the system with independent velocities, the spin-charge interplay changes dramatically as the dimensionality is changed. Whereas there is no competition between dopants and the magnetic environment in 1D, their interplay in 2D is at the heart of many exotic and poorly understood phases including the pseudogap and the superconducting phases. A simple description of the lattice structure of these 2D materials and consequently their interesting physics, whose phase diagram is shown in Fig. 2.1, are believed to be captured by the Fermi-Hubbard model. Interesting phases begin to emerge when antiferromagnets are doped away from half-filling, and an understanding of their underlying mechanisms is still open to debate, leading to wide range of theoretical approaches [43, 149–151].

The most fundamental “unit” of such an interplay between spin and charge is the effect of a single dopant on a 2D antiferromagnet - or asked another way, how does the spin background affect the dynamics of a single charge impurity? As we saw in Section 2.4, a single dopant in a 2D antiferromagnet cannot move without altering the spin order in the system, and consequently leaves behind a series of flipped spins at an energy cost. In this chapter, we will see equilibrium signatures of such a process - the spin correlations across the dopant differing dramatically from the 1D case and the dopant getting dressed by a spin cloud [119–122, 152].

In our quantum simulator for the Fermi-Hubbard model, imaging such dressed dopants - called magnetic polarons - is achieved by preparing a two-dimensional Fermi-Hubbard systems with antiferromagnetic correlations in such a way that there is a high probability to find a doublon impurity in the system. The effect of the spin background on the charge is visualized from the reference frame of the doublon by observing a distorted spin cloud of radius ~ 1 lattice site surrounding it. The first section will cover experiments performed in the crossover from 1D to 2D, which show preliminary signs of the spin-charge interplay. The second section will summarize experiments carried out in 2D showing striking evidence for the existence of polarons.

The main results of this chapter are published in:

“Direct observation of incommensurate magnetism in Hubbard chains”

Guillaume Salomon, Joannis Koepsell, Jayadev Vijayan, Timon A. Hilker, Jacopo Nespolo, Lode Pollet, Immanuel Bloch and Christian Gross

Nature **565**, 56–60 (2019)

“Imaging magnetic polarons in the doped Fermi–Hubbard model”

Joannis Koepsell, Jayadev Vijayan, Pimonpan Sompert, Fabian Grusdt, Timon A. Hilker, Eugene Demler, Guillaume Salomon, Immanuel Bloch and Christian Gross

Nature **572**, 358–362 (2019)

6.1 Development of correlations in two dimensions

In previous chapters, we saw the formation of incommensurate spin-density waves and spin-charge separation in 1D Fermi-Hubbard chains. The mechanism underlying these phenomena is the decoupling between the spin and charge modes in 1D materials, where the fermionic atoms necessarily have to pass through one another to move along the chain. However, this is no longer the case when the atoms are free to also move along the second dimension.

In a fully two-dimensional material, one expects the interplay between charge and spin to manifest itself in the form of a breakdown of spin-charge separation and in particular, the reduction of antiferromagnetic correlations across a dopant.

To investigate this effect, we first prepare systems with variable dimensionality between one and two dimensions [109]. Then, using our density and spin resolved quantum gas microscope, we observe the spin correlations across the detected dopants.

6.1.1 Preparing two dimensional systems

An advantage of the platform of using ultracold atoms in optical lattices is that the optical lattices are produced by external laser beams and are in a sense “independent” of the physics that happens in them. This is different from real condensed matter systems where there would be no lattice in the absence of material.

In our case, the direct control we have over the laser beams implies that we can arbitrarily make changes to the optical lattice with little effort. We use the knob of laser intensity to smoothly transition from 1D to 2D Fermi-Hubbard systems - the intensities of the laser and consequently the depth of the x- and y-lattices are tuned relative to each other. In this way, we can change the ratio between the tunneling amplitude along the x- and y- axes t_x/t_y while keeping the interaction U/t_x constant.

For the experiment described in this section, degenerate Fermi gases of about $70\ ^6\text{Li}$ atoms in the physics lattice are prepared with a $U/t_x = 14$. The ratio t_y/t_x is then varied from 0 to 1 while keeping the interaction energy U/t_x fixed, by changing the laser intensities.

At t_y/t_x close to 0 (one dimensional chains along the x-axis), one expects to reproduce results similar to what was described in Section 3.4. Indeed, the measured nearest neighbour correlator along the x-axis $C(1)_x$ has an absolute value > 0.4 and

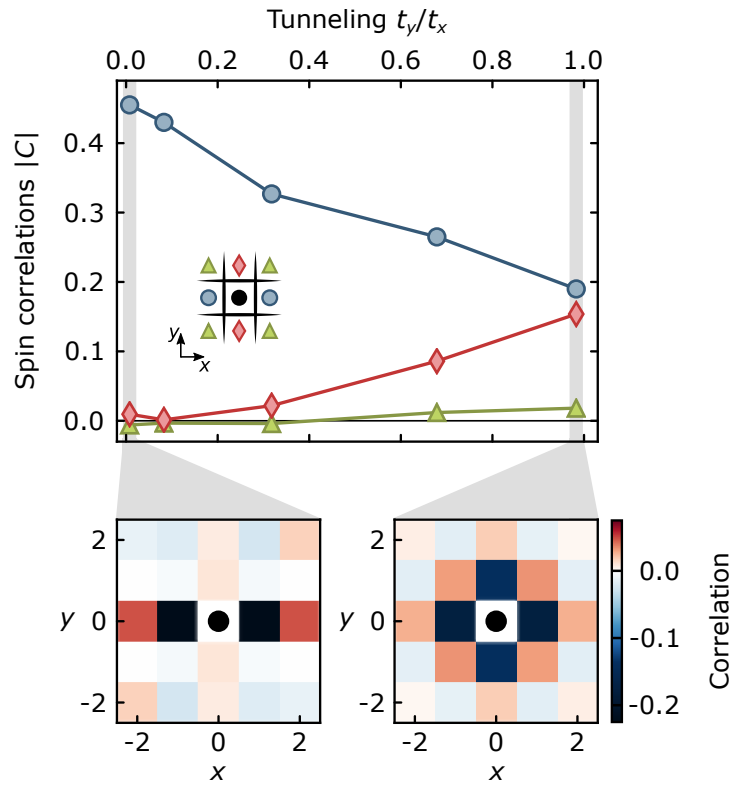


FIGURE 6.1: **Spin correlations in the crossover from one to two dimensions.** Spin correlations are plotted for different dimensionalities defined by the ratio of tunneling in the y - and x - directions t_y/t_x . The different curves correspond to nearest neighbour spin correlations along the x -axis (blue circles), the y -axis (red diamonds) and the diagonal spin correlations (green triangles), all at $U/t_x = 14$. The spin correlations decrease along x and increase along y until a symmetric point is reached at $t_x = t_y$. The maps below show the 2D spin correlations amplitudes $C(x, y)$ in the 1D limit ($t_y/t_x = 0$) (left) and 2D limit ($t_y/t_x = 1$) (right) as a function of distance in x and y . The checkerboard pattern of alternating spins (with correlation strength decaying radially) in 2D is an indication of the formation of 2D Fermi-Hubbard systems with antiferromagnetic correlations.

the nearest neighbour correlator along the y -axis $C(1)_y$ is zero (see Fig. 6.1), indicating the formation of a Heisenberg antiferromagnetic chain (see left inset, Fig. 6.1). Technically, a value of $C(1)_x = 0.6$ is predicted for a Heisenberg antiferromagnet at zero temperature.

However, as t_y/t_x is increased to 1 (two dimensional system), the nearest neighbour correlator along both x - and y - axis, $C(1)_x$ and $C(1)_y$ respectively, approach one another. A decrease in the absolute value of $C(1)_x$ during the crossover is also seen. This effect is also expected at zero temperature (from -0.6 in 1D to -0.36 in 2D) due to a higher coordination number in the two dimensions, which modifies the quantum fluctuations [72].

There is also a rise in the value of the diagonal spin correlator from a value of zero in one dimension. The emergence of the two-dimensional antiferromagnetic correlations is also evident in the checkerboard-like pattern seen in the spin correlation map (see right inset, Fig. 6.1).

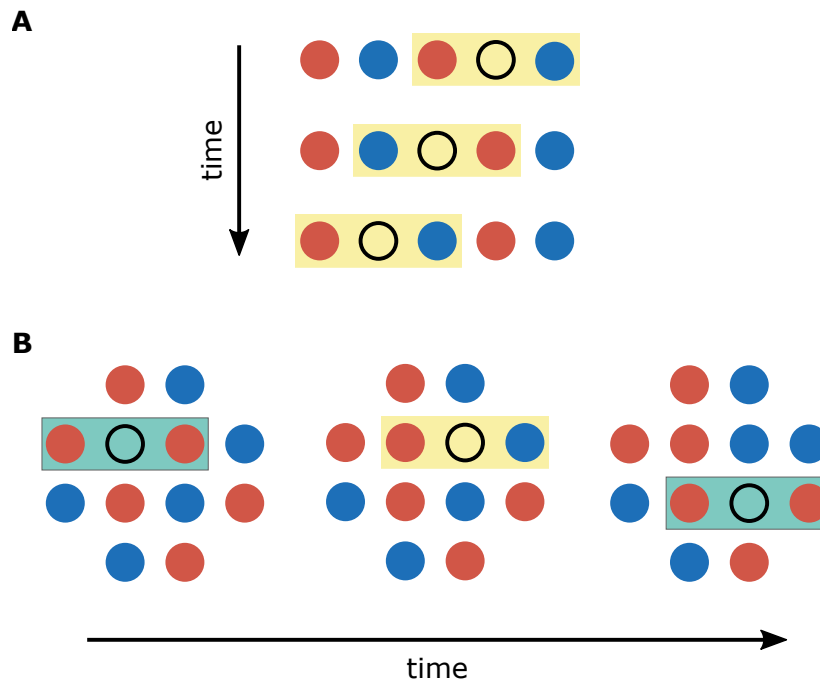


FIGURE 6.2: **Spin correlations across dopants in the dimensional crossover.** **A**, In 1D, a dopant surrounded by opposite spins (yellow bonds) can move around without changing the spin configuration across it. Even in the case the dopant is surrounded by parallel spins, it quickly rids itself of such a configuration and gets surrounded by opposite spins (see Sec. 5.4.1). The result is the presence of strong antiferromagnetic correlations across the dopant. **B**, In 2D, however, as the dopant moves, it is alternately surrounded by parallel spins (green bonds) and opposite spins (yellow bonds) with every tunneling event. The result is that the antiferromagnetic correlations present in 1D get washed out during the crossover.

6.1.2 Spin correlations across dopants

As mentioned earlier in the chapter, a convenient observable to investigate the effect of the spin background on the charge impurity is to look at the spin correlations surrounding a dopant:

$$C_{SD}(x, y) = 4 \langle \hat{S}_{i,j}^z \hat{S}_{i+x,j+y}^z \rangle_{\bullet_{i,j} \circ_{i+1,j} \bullet_{i+x,j+y}} \quad (6.1)$$

where filled circles denote a single atom located at sites (i, j) and $(i + x, j + y)$ and the empty circle denotes a doublon located at site $(i + 1, j)$.

The underlying principle behind spin-charge separation is that the motion of the dopant is independent of the spin background. Thereby, the spin correlations across the dopant in 1D is expected to be strongly antiferromagnetic (see Fig. 6.2), because the two spins involved spend most of the time as nearest neighbours, just not at the moment when the lattice is frozen, when the dopant was inbetween them.

However, once the dimensionality is increased, the dopant is not allowed to tunnel around independent of the spin background anymore and the antiferromagnetic correlations get washed out.

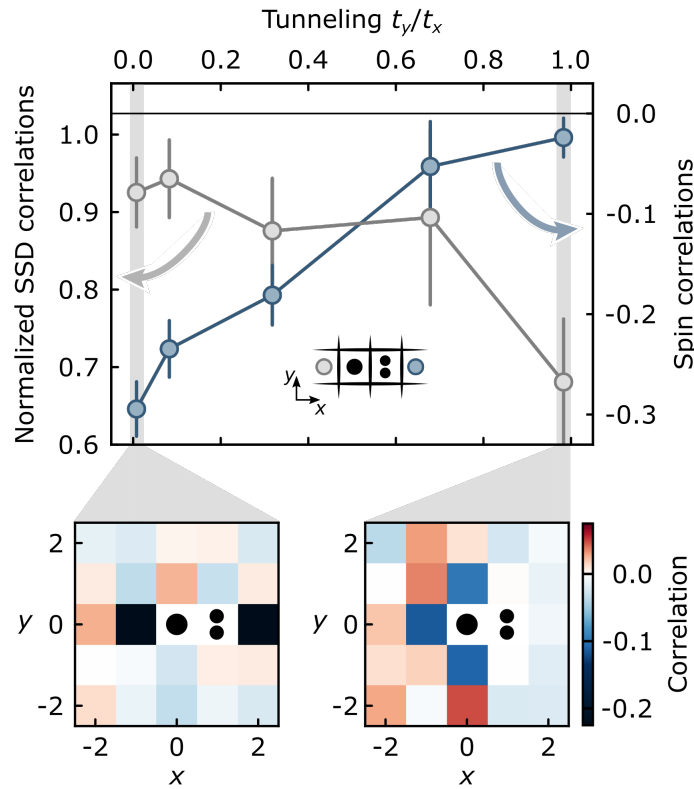


FIGURE 6.3: **Spin correlations conditioned on distance from dopant in the crossover from 1D to 2D.** Spin correlations between adjacent sites $C_{SD}(-1,0)/C(-1,0)$ (gray) and across doublons $C_{SD}(2,0)$ (blue) along the x direction. The strong antiferromagnetic correlations across doublons in 1D are reduced in 2D, which is a signature of the formation of a polaron. Figures below show the spin correlations $C_{SD}(x,y)$ between sites $(0,0)$ and (x,y) conditioned on finding a doublon on site $(1,0)$ in the 1D (left) and 2D (right) case.

The spin correlations directly across a doublon, given by $C_{SD}(2,0)$, is calculated for the same crossover dataset which was used in Fig. 6.1. The result is shown in Fig. 6.3.

At $t_y/t_x = 0$, the chains are essentially one dimensional (along the x -axis). As we know from previous chapters, in 1D chains, the spin and charge sectors are decoupled, meaning that the strength of the (antiferro-)magnetic correlations are unaffected by the presence of doublon. The underlying mechanism is the delocalized nature of the dopant, which does not stay between the same two atoms for extended periods of time. The result of such decoupling of spin and charge sectors is that the spin correlation across the doublon $C_{SD}(2,0)$ has an amplitude identical to the mean nearest neighbour spin correlator $C_x(1)$.

However, the situation is very different as t_y/t_x approaches 1, when fully two-dimensional systems start being formed. In the 2D limit, the antiferromagnetic correlations across the doublon is clearly reduced in comparison to the 1D case. The nearest neighbour correlations in the immediate vicinity of the doublon is reduced to about 70% of the undoped case.

This strong suppression of the antiferromagnetic correlations across the dopant

from -0.3 to almost zero (favouring neither ferromagnetic nor antiferromagnetic) in the crossover from 1D to 2D is strong indication that the nature of the competition between charge delocalization and the magnetic environment is dependent on the dimensionality.

The emergence of a competition or interplay between spin background and the motional degrees of freedom of the dopant is in turn a result of the breakdown of spin-charge separation. The dopant is no longer unaffected by the spin background and in fact seems to be surrounded by a region of distorted spins around it. Such a quasiparticle, comprising of a dopant dressed by a local spin cloud, is precisely what a magnetic polaron as discussed in Sec. 2.4 is.

6.2 Single dopant in a two dimensional antiferromagnet

The lack of a clear understanding of the competition between the antiferromagnetic correlations and charge delocalization, possibly leading to the formation of magnetic polarons, instigated us to perform a dedicated set of experiments to characterize in detail the effect of the interplay of spin and charge in two dimensions. This section describes the results of these experiments which led us to confirm the formation of polarons in two dimensional Fermi-Hubbard systems.

We adiabatically prepare 2D Fermi-Hubbard systems at a temperature of $T \sim 1.4J$ with a very high probability of having a doublon dopant somewhere in the central region of the system. Then, using our quantum gas microscope, we map out the spin correlations between different sites in the system. Since we can identify the precise location of doublons in the system, we can look at local disturbances in the spin background in the immediate vicinity of the doublon and contrast it to the rest of the cloud.

In the case of polaron formation, we would expect to see a disturbance in the spin background that is localized around the doublon (see discussion in Sec. 2.4). In case there is no polaron formed, we would expect to see an overall reduction in the antiferromagnetic correlations across the entire system, due to the delocalization of the doublon independent of the spin background.

A summary of the results pertaining to the formation of a polaron at the level of a single dopant in a 2D Fermi-Hubbard system is presented in this section. A more detailed discussion of the study will be available in the thesis of Joannis Koepsell.

6.2.1 Formation of magnetic polarons

This section describes the spin correlations present in 2D Fermi-Hubbard systems adiabatically prepared with mobile dopants. The experimental sequence is similar to the one described in Section 5.1, where a degenerate Fermi gas of ~ 70 ${}^6\text{Li}$ atoms is loaded into the 2D physics lattice with an onsite interaction energy of $U/t_x = 14$. The tunneling amplitude along the x- and y-axis are $t_x/h \approx t_y/h = 170$ Hz and a superexchange amplitude of $J/h = 50$ Hz.

A spin filter of $|S_{\text{tot}}^z| \leq 3.5$ is applied to avoid experimental runs where strongly magnetized clouds were prepared. To prevent contribution from doublon-hole fluctuations in our system, we use a filter to remove doublons with holes as nearest neighbours.

The dopant we consider could in principle be either a hole or a doublon. We choose doublon doping in this experiment because they are trapped by our confining harmonic potential and are likely to be found in the centre of the cloud rather than at the wings. If we had worked with holes, the signal-to-noise ratio would be decreased by the presence of holes created during the detection.

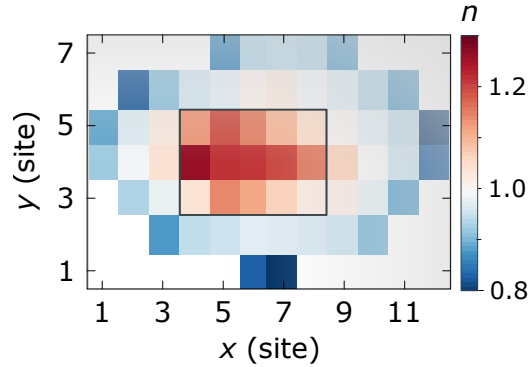


FIGURE 6.4: **Average density profile of prepared 2D systems.** The chemical potential in the 2D system is fixed such that there is a high probability of finding one or two doublons in cloud. These doublons are likely to be located in the central region within an area of 3×5 sites (black box), due to the confining potential of our traps.

To realize doped systems, we create clouds with an average of $1.95(1)$ doublons in the central 15 sites of the cloud (see black box, Fig. 6.4), by setting an appropriate chemical potential that can be tuned by varying the end point of our evaporative cooling technique. The number of doublons in our system can be controlled precisely with this technique. In clouds of $\sim 70 - 75$ atoms, we achieve our desired doping.

The average density distribution in the cloud is shown in Fig. 6.4. The central region, indicated by the black box, is the region where the delocalized dopant doublons arising from an increased chemical potential are likely to be located. The probability of finding the doublon outside this region is reduced due to the harmonic confinement provided by the lattice, with a trapping frequency of about $w/(2\pi) = 250$ Hz.

In this section, the spin correlation or “bond strength” between two atoms (indicated by filled circles) located at positions r_1 and r_2 will be defined by:

$$C(\mathbf{r}_1, \mathbf{r}_2) = 4 \langle S_{\mathbf{r}_1}^z S_{\mathbf{r}_2}^z \rangle_{\bullet_{\mathbf{r}_1} \bullet_{\mathbf{r}_2}}. \quad (6.2)$$

In this notation, we can define a three-point correlator which gives the bond strength between two sites at positions r_1 and r_2 conditioned on having a doublon at position r_0 :

$$C(\mathbf{r}_0; \mathbf{r}_1, \mathbf{r}_2) = 4 \langle S_{\mathbf{r}_1}^z S_{\mathbf{r}_2}^z \rangle_{\bullet_{\mathbf{r}_0} \bullet_{\mathbf{r}_1} \bullet_{\mathbf{r}_2}} \equiv C(\mathbf{r}_0; \mathbf{r}, \mathbf{d}) = 4 \langle S_{\mathbf{r}_0 + \mathbf{r} - \frac{\mathbf{d}}{2}}^z S_{\mathbf{r}_0 + \mathbf{r} + \frac{\mathbf{d}}{2}}^z \rangle_{\bullet_{\mathbf{r}_0} \bullet_{\mathbf{r}_0 + \mathbf{r} - \frac{\mathbf{d}}{2}} \bullet_{\mathbf{r}_0 + \mathbf{r} + \frac{\mathbf{d}}{2}}}. \quad (6.3)$$

Here, $\mathbf{d} = \mathbf{r}_2 - \mathbf{r}_1$ and $\mathbf{r} = (\mathbf{r}_1 + \mathbf{r}_2)/2 - \mathbf{r}_0$ are the bond length and the distance of

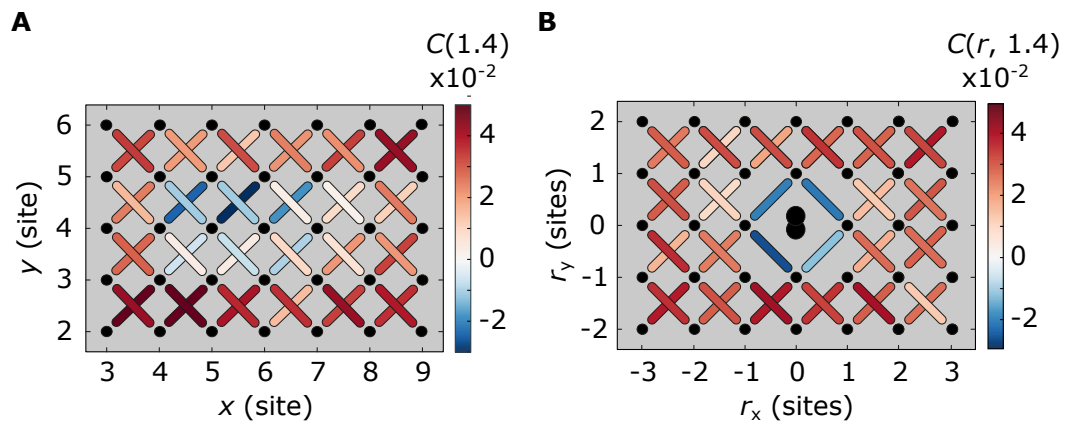


FIGURE 6.5: **Map of diagonal spin correlations in the system.** **A**, Bonds indicating diagonal spin correlation strengths in the cloud. Black dots represent positions of atoms in the lattice. In an area of ~ 15 sites corresponding to the area with the highest doublon density, a change in sign of the correlations is seen. **B**, Diagonal spin correlations from the reference frame of the doublon. In the immediate vicinity of the doublon, the bond strengths are negative, whereas the background correlations have a positive value. This confirms the picture of a polaron as a doublon dressed by a locally distorted spin cloud.

the bond from the doublon respectively. This three-point correlator is a natural observable to map out the spin correlations in the system in the presence of a doublon. In particular, we can look at the spin correlations as a function of the bond distance \mathbf{r} from the doublon, in order to investigate local effects of the doublon on the spin background.

The effect of the interplay between the delocalized doublon and the spin background is most pronounced in the immediate vicinity of the doublon and this is also where we expect to see the maximum distortion of the spin background. The four spin bonds closest to the doublon by distance are the diagonal bonds ($|\mathbf{d}| = 1.4$) which connect the four atoms closest (nearest neighbours) to the doublon.

When the diagonal bonds and their strengths are mapped out (see Fig. 6.5, left), we see a region of spin distortion (indicated by reduced antiferromagnetic correlations) in the centre of the cloud. This region, around 5×3 sites, is exactly the same region where there is a high probability of finding the doublon (see black box, Fig. 6.4), indicating that the spin distortion is correlated to the position of the doublon.

Our analysis enables us to average the three-point correlator over all positions and obtain the average spin correlations in the reference frame of a single doublon $C(\mathbf{r}, \mathbf{d})$ (see Fig. 6.5, right). In this frame, the deviation of the spin correlations in the immediate vicinity of the doublon from the antiferromagnetic background is clear to see. Whereas far away from the doublon, there are strong antiferromagnetic correlations in the system, these correlations change sign and become ferromagnetic in a small region around the doublon.

6.3 Conclusion

In this chapter, we moved away from 1D chains and towards 2D systems with antiferromagnetic correlations by tuning the ratio of the lattice depths in the x - and y - directions. The spin correlations across dopants in the dimensional crossover was seen to depend strongly on the dimensionality of the system, with the correlations vanishing in fully 2D systems. This indicated the breakdown of spin-charge separation and the formation of a polaron.

The results discussed in this chapter represent a first microscopic characterization of magnetic polarons in real space. They show that the dressing of the doublons by a local spin distortion has its origins in the competition between kinetic and magnetic energy in the system, which is absent one dimension.

Polarons are the “building blocks” of many complex many-body phases and they emerge already at the level of a single dopant. Future studies in this direction will focus on the nature of the interaction between multiple polarons and the formation of a stripe phase in the presence of multiple dopants.

A major limitation at the time of these measurements was the system size which, due to the harmonic confinement of the trap, put a bound on the number of mobile doublons we could have in the system. Current upgrades in the laboratory will see significant improvements in system sizes and achievable temperatures in the prepared two dimensional Fermi-Hubbard systems. Implementation of larger and colder [74, 153, 154] systems will no doubt lead to a lot more insight into the nature of the interplay between spin and charge in doped 2D Fermi-Hubbard systems.

Chapter 7

Summary and outlook

Throughout this thesis, we have seen how microscopy of ultracold fermions in optical lattices has enabled the confirmation of a variety of phenomena occurring in real condensed matter systems, which are hard to prove otherwise. This is, after all, the main aim of quantum simulators - to provide a fundamental microscopic description of strongly correlated many-body systems by using a clean and controllable analogous platform.

In particular, we were able to probe the phenomenon of incommensurate magnetism in one dimension and the formation of magnetic polarons in two dimensions with the spatial resolution of a single lattice site. Then, with the additional resolution of time, we were able to study the dynamics of a single dopant in a 1D antiferromagnetic chain, demonstrating the phenomenon of spin-charge separation.

Our ability to study these phenomena relied heavily on having both spin and charge resolution for every single lattice site. Such an imaging technique allows us to obtain full counting statistics and consequently, to analyze various complex multi-point correlation functions across the whole system.

There are several directions that our experiment can go from here. The most natural extension of the results presented here would be to study the dynamical effects of spin and charge in quasi- or fully two dimensional systems. One could imagine preparing a dopant in two dimensions and tracking its propagation in real space and time. The signatures we saw of the vastly different physics occurring in two dimensions - the formation of a polaron - could be studied with time-resolution to obtain an effective mass of the polaron [155–157]. Such experiments could also look at the crossover from 1D to 2D in order to understand how dimensionality affects the behaviour of a polaron.

Another interesting experiment would be to search for the analogue of a domain wall in two dimensions - the stripe phase [96, 138, 158, 159]. To study stripe phase formation - the ordering of multiple dopants in a 2D antiferromagnet - it is necessary to prepare more dopants and have a bigger system size than described in Chapter 5. Upgrades are being planned in both these directions - a new bichromatic optical lattice along all three axes and a digital micromirror device (DMD) capable to projecting arbitrary potentials onto the atoms - and will be implemented in the near future. An alternative way to study the behavior of stripes could be to start by preparing an ordered state of dopants and observe the resultant dynamics.

A simpler experiment that can be done with a larger system size would be to study the interaction between two polarons. An attraction between two dopants in an antiferromagnet might be observable even with the temperatures currently achievable. Such an experiment would be interesting even without time-resolution;

the attraction would be manifest in density-density correlations. However, with time-resolution, experiments which directly look at how one dopant affects the string of flipped spins left behind by another dopant would be possible.

A big challenge in any of these proposals is the ability to prepare dopants in a controlled manner. In the dynamical experiment described in Chapter 6, we prepared dopants by resonantly scattering a fermion out of the Fermi-Hubbard chain. Such a quench excites a wide spectrum of spin and charge modes and is not ideal to study, for example, the low energy quasiparticle modes. Perhaps a way to overcome this problem is not do a local quench, but rather by projecting global optical patterns with a DMD which excites only the low energy modes.

In two dimensions systems with strong repulsive interactions, even a single hole can lead to itinerant ferromagnetism and the Nagaoka effect [100, 160–163].

Over the course of the past months, a few upgrades have been incorporated into the experiment and several more have been planned.

A major limitation of our fluorescence imaging process has been the stability and output power of the pinning lattices in which we perform the Raman sideband cooling. Heating from photon scattering can lead to the system going away from the Lamb-Dicke regime, giving rise to an error in detecting the atoms of a few percent. To ensure that the atoms are cooled effectively, it is important to have low relative intensity noise (RIN) and low pointing instability.

For the results described in this thesis, we worked with three Nufern 50W fiber amplifier for the pinning lattice which took several hours of operation to stabilize. Since then, we have upgraded this setup to work with three ALS (Azur Light Systems) 50W fiber amplifiers, which have considerably better performance - less than 4% drift in output power and at low frequencies, a RIN that is 10 – 20dB lower than the Nufern and quick pointing stabilization times.

To gain space on the optical table, we made use of miniaturized mounts and breadboards for the new pinning lattice setup, which now takes up roughly half the area as before. We were also able to obtain 40% more optical power out of this setup, all of which increases the efficiency of cooling the atoms while collecting fluorescent photons.

Another major upgrade involves switching from the lattice setup described in Chapter 3 to a bichromatic lattice using light at both 1064nm and 532nm. More details of this setup can be found in the masters theses of Michael Höse and Dominik Bourgund. The main motivation for moving away from sending the lattice beams through the high-NA objective is that this technique is prone to aberrations that create inhomogenous potentials for the atoms and it poses a fundamental limit on how big the beam can be at the focus, limiting the size of our lattice gas. For example, any defect (scratch, dirt, etc.) on the beam path gets imaged onto the atoms and since the beams are off-center from the optical axis, there could be unwanted wavefront corrections.

The alternative we choose is to use mirrors to direct the lattice beams straight to the atoms. In order to have a superlattice, we then overlap two beams - one at 1064nm and the other at 532nm - and send them to the mirrors.

The bichromatic lattice along the vertical direction has already been implemented in the past months. Having the ability to split along the z -axis clears up space in the xy -plane which we needed before for spin resolution. We can now use a small scale

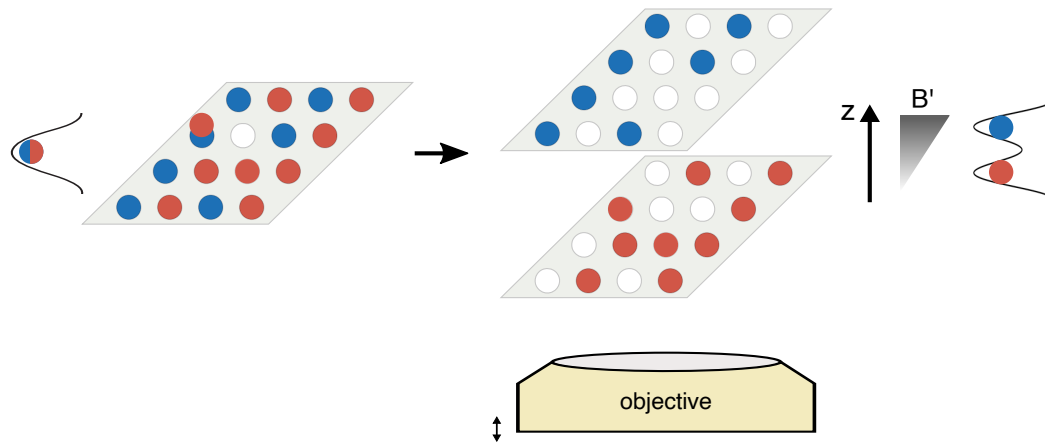


FIGURE 7.1: **Splitting along the vertical axis using a superlattice.** Obtaining spin resolution along the z -axis allows larger system sizes by using the short-short lattice in the xy -plane. The superlattice spacing is $3\mu\text{m}$. After splitting, the two planes can be pumped further away from each other. Images are taken by moving the focus of the microscope from one plane to the other with a piezo controller. The geometry and phase control of along the vertical direction also enables the preparation of bilayer systems.

lattice along both x - and y - axes and automatically gain a factor of two in atom number, and use the splitting along the vertical for spin resolution. A schematic is shown in Fig. 7.1. The physics is allowed to happen in the 2D plane and the lattices are ramped up to freeze the distribution. The superlattice is then ramped up along with a gradient field in the z -direction and the atoms are split into two different planes according to their spin states. These two planes can then be pumped away from one another by changing the relative phase between the beams at 1064nm and 532nm. Two images are then taken - one of each plane - by moving the focus of the microscopic objective from one plane to the other using a piezo controller. While one plane is being imaged, the other plane appears as a blurred background and vice versa. On reconstructing the spin distributions, full counting statistics of density and spin can once again be recovered.

A direct benefit of preparing atoms in different planes and controlling their interaction is the ability to study the physics of bilayer systems. By preparing two Fermi-Hubbard planes and tuning the ratio of intra-plane and inter-plane tunneling, many interesting phases can emerge [164–167]. For weak interaction strengths, the bilayer system is expected to undergo a transition from a Mott-insulating to metallic and then to a band-insulating phase as the inter-plane tunneling is increased. However, for strong interactions, a crossover from the Mott-insulating to the band-insulating phase is expected. Interlayer hybridization is also predicted to play a key role in the superconducting pairing mechanism [168]. Experiments studying the competition between in-plane spin ordering and the quantum fluctuations emerging from the coupling to the second layer can also be readily performed by extending the experimental scheme above to obtain spin resolved images of both planes of the bilayer system.

A research direction which has seen a lot of progress in the past few years has been in trying to achieve colder systems. To see phenomena that occur close to the critical temperature for high T_c superconductors, temperatures as low as $T_c/t \approx 0.05$

are required. One approach, pioneered by the group at Harvard, tries to redistribute the entropy of the cloud by using a dimple beam that collects the colder atoms while the hotter atoms go to the outer edges which act as a reservoir [74], and achieves temperatures as low as $T/t \approx 0.25$. With new bichromatic superlattices along x - and y - directions, we could implement a scheme where we start with a band-insulator and split it into a Mott-insulator. This approach works because the band-insulator has very low entropy per particle, and splitting it into a Mott-insulator can help in the preparation of very low entropy system.

Regardless of which direction the laboratory decides to take in the end, a lot of progress will be made in the next years towards the understanding of the interplay between spin and charge in doped antiferromagnets at the microscopic level. From experience, there is no doubt that interesting research directions will emerge seemingly out of nowhere and lead to exciting results. We are truly entering the era when ultracold atom quantum simulators are starting to provide previously inaccessible microscopic insight into strongly correlated many body systems.

Bibliography

- [1] R. P. Feynman. “Simulating physics with computers”. In: *International Journal of Theoretical Physics* 21.6 (1982), pp. 467–488. ISSN: 1572-9575. DOI: [10.1007/BF02650179](https://doi.org/10.1007/BF02650179). URL: <https://doi.org/10.1007/BF02650179> (cited on page 1).
- [2] A. Acín, I. Bloch, H. Buhrman, T. Calarco, C. Eichler, J. Eisert, D. Esteve, N. Gisin, S. J. Glaser, F. Jelezko, S. Kuhr, M. Lewenstein, M. F. Riedel, P. O. Schmidt, R. Thew, A. Wallraff, I. Walmsley, and F. K. Wilhelm. “The quantum technologies roadmap: a European community view”. In: *New Journal of Physics* 20.8 (2018), p. 080201. DOI: [10.1088/1367-2630/aad1ea](https://doi.org/10.1088/1367-2630/aad1ea). URL: <https://doi.org/10.1088/1367-2630/aad1ea> (cited on page 1).
- [3] A. Ashkin. “Atomic-Beam Deflection by Resonance-Radiation Pressure”. In: *Phys. Rev. Lett.* 25 (19 1970), pp. 1321–1324. DOI: [10.1103/PhysRevLett.25.1321](https://link.aps.org/doi/10.1103/PhysRevLett.25.1321). URL: <https://link.aps.org/doi/10.1103/PhysRevLett.25.1321> (cited on page 1).
- [4] W. D. Phillips and H. Metcalf. “Laser Deceleration of an Atomic Beam”. In: *Phys. Rev. Lett.* 48 (9 1982), pp. 596–599. DOI: [10.1103/PhysRevLett.48.596](https://link.aps.org/doi/10.1103/PhysRevLett.48.596). URL: <https://link.aps.org/doi/10.1103/PhysRevLett.48.596> (cited on page 1).
- [5] S. Chu, L. Hollberg, J. E. Bjorkholm, A. Cable, and A. Ashkin. “Three-dimensional viscous confinement and cooling of atoms by resonance radiation pressure”. In: *Phys. Rev. Lett.* 55 (1 1985), pp. 48–51. DOI: [10.1103/PhysRevLett.55.48](https://link.aps.org/doi/10.1103/PhysRevLett.55.48). URL: <https://link.aps.org/doi/10.1103/PhysRevLett.55.48> (cited on page 1).
- [6] A. Aspect, E. Arimondo, R. Kaiser, N. Vansteenkiste, and C. Cohen-Tannoudji. “Laser Cooling below the One-Photon Recoil Energy by Velocity-Selective Coherent Population Trapping”. In: *Phys. Rev. Lett.* 61 (7 1988), pp. 826–829. DOI: [10.1103/PhysRevLett.61.826](https://link.aps.org/doi/10.1103/PhysRevLett.61.826). URL: <https://link.aps.org/doi/10.1103/PhysRevLett.61.826> (cited on page 1).
- [7] P. D. Lett, R. N. Watts, C. I. Westbrook, W. D. Phillips, P. L. Gould, and H. J. Metcalf. “Observation of Atoms Laser Cooled below the Doppler Limit”. In: *Phys. Rev. Lett.* 61 (2 1988), pp. 169–172. DOI: [10.1103/PhysRevLett.61.169](https://link.aps.org/doi/10.1103/PhysRevLett.61.169). URL: <https://link.aps.org/doi/10.1103/PhysRevLett.61.169> (cited on page 1).
- [8] J. Dalibard and C. Cohen-Tannoudji. “Laser cooling below the Doppler limit by polarization gradients: simple theoretical models”. In: *J. Opt. Soc. Am. B* 6.11 (1989), pp. 2023–2045. DOI: [10.1364/JOSAB.6.002023](https://doi.org/10.1364/JOSAB.6.002023). URL: <http://josab.osa.org/abstract.cfm?URI=josab-6-11-2023> (cited on page 1).
- [9] F. Diedrich, J. C. Bergquist, Wayne M. Itano, and D. J. Wineland. “Laser Cooling to the Zero-Point Energy of Motion”. In: *Phys. Rev. Lett.* 62 (4 1989), pp. 403–406. DOI: [10.1103/PhysRevLett.62.403](https://link.aps.org/doi/10.1103/PhysRevLett.62.403). URL: <https://link.aps.org/doi/10.1103/PhysRevLett.62.403> (cited on page 1).

- [10] M. H. Anderson, J. R. Ensher, M. R. Matthews, C. E. Wieman, and E. A. Cornell. "Observation of Bose-Einstein Condensation in a Dilute Atomic Vapor". In: *Science* 269.5221 (1995), pp. 198–201. ISSN: 0036-8075. DOI: [10.1126/science.269.5221.198](https://doi.org/10.1126/science.269.5221.198). eprint: <https://science.sciencemag.org/content/269/5221/198.full.pdf>. URL: <https://science.sciencemag.org/content/269/5221/198> (cited on page 2).
- [11] K. B. Davis, M. Mewes, M. A. Joffe, M. R. Andrews, and W. Ketterle. "Evaporative Cooling of Sodium Atoms". In: *Phys. Rev. Lett.* 74 (26 1995), pp. 5202–5205. DOI: [10.1103/PhysRevLett.74.5202](https://doi.org/10.1103/PhysRevLett.74.5202). URL: <https://link.aps.org/doi/10.1103/PhysRevLett.74.5202> (cited on page 2).
- [12] C. C. Bradley, C. A. Sackett, J. J. Tollett, and R. G. Hulet. "Evidence of Bose-Einstein Condensation in an Atomic Gas with Attractive Interactions". In: *Phys. Rev. Lett.* 75 (9 1995), pp. 1687–1690. DOI: [10.1103/PhysRevLett.75.1687](https://doi.org/10.1103/PhysRevLett.75.1687). URL: <https://link.aps.org/doi/10.1103/PhysRevLett.75.1687> (cited on page 2).
- [13] B. DeMarco and D. S. Jin. "Onset of Fermi Degeneracy in a Trapped Atomic Gas". In: *Science* 285.5434 (1999), pp. 1703–1706. ISSN: 0036-8075. DOI: [10.1126/science.285.5434.1703](https://doi.org/10.1126/science.285.5434.1703). eprint: <https://science.sciencemag.org/content/285/5434/1703.full.pdf>. URL: <https://science.sciencemag.org/content/285/5434/1703> (cited on page 2).
- [14] S. R. Granade, M. E. Gehm, K. M. O'Hara, and J. E. Thomas. "All-Optical Production of a Degenerate Fermi Gas". In: *Phys. Rev. Lett.* 88 (12 2002), p. 120405. DOI: [10.1103/PhysRevLett.88.120405](https://doi.org/10.1103/PhysRevLett.88.120405). URL: <https://link.aps.org/doi/10.1103/PhysRevLett.88.120405> (cited on page 2).
- [15] A. G. Truscott, K. E. Strecker, W. I. McAlexander, G. B. Partridge, and R. G. Hulet. "Observation of Fermi Pressure in a Gas of Trapped Atoms". In: *Science* 291.5513 (2001), pp. 2570–2572. ISSN: 0036-8075. DOI: [10.1126/science.1059318](https://doi.org/10.1126/science.1059318). eprint: <https://science.sciencemag.org/content/291/5513/2570.full.pdf>. URL: <https://science.sciencemag.org/content/291/5513/2570> (cited on page 2).
- [16] F. Schreck, L. Khaykovich, K. L. Corwin, G. Ferrari, T. Bourdel, J. Cubizolles, and C. Salomon. "Quasipure Bose-Einstein Condensate Immersed in a Fermi Sea". In: *Phys. Rev. Lett.* 87 (8 2001), p. 080403. DOI: [10.1103/PhysRevLett.87.080403](https://doi.org/10.1103/PhysRevLett.87.080403). URL: <https://link.aps.org/doi/10.1103/PhysRevLett.87.080403> (cited on page 2).
- [17] Z. Hadzibabic, C. A. Stan, K. Dieckmann, S. Gupta, M. W. Zwierlein, A. Görlitz, and W. Ketterle. "Two-Species Mixture of Quantum Degenerate Bose and Fermi Gases". In: *Phys. Rev. Lett.* 88 (16 2002), p. 160401. DOI: [10.1103/PhysRevLett.88.160401](https://doi.org/10.1103/PhysRevLett.88.160401). URL: <https://link.aps.org/doi/10.1103/PhysRevLett.88.160401> (cited on page 2).
- [18] G. Roati, F. Riboli, G. Modugno, and M. Inguscio. "Fermi-Bose Quantum Degenerate ^{40}K – ^{87}Rb Mixture with Attractive Interaction". In: *Phys. Rev. Lett.* 89 (15 2002), p. 150403. DOI: [10.1103/PhysRevLett.89.150403](https://doi.org/10.1103/PhysRevLett.89.150403). URL: <https://link.aps.org/doi/10.1103/PhysRevLett.89.150403> (cited on page 2).
- [19] K. M. O'Hara, S. L. Hemmer, M. E. Gehm, S. R. Granade, and J. E. Thomas. "Observation of a Strongly Interacting Degenerate Fermi Gas of Atoms". In: *Science* 298.5601 (2002), pp. 2179–2182. ISSN: 0036-8075. DOI: [10.1126/science.1079107](https://doi.org/10.1126/science.1079107). eprint: <https://science.sciencemag.org/content/298/>

- 5601/2179.full.pdf. URL: <https://science.sciencemag.org/content/298/5601/2179> (cited on page 2).
- [20] T. Bourdel, J. Cubizolles, L. Khaykovich, K. M. F. Magalhães, S. J. J. M. F. Kokkelmans, G. V. Shlyapnikov, and C. Salomon. “Measurement of the Interaction Energy near a Feshbach Resonance in a ${}^6\text{Li}$ Fermi Gas”. In: *Phys. Rev. Lett.* 91 (2 2003), p. 020402. DOI: [10.1103/PhysRevLett.91.020402](https://doi.org/10.1103/PhysRevLett.91.020402). URL: <https://link.aps.org/doi/10.1103/PhysRevLett.91.020402> (cited on page 2).
- [21] M. Greiner, O. Mandel, T. Rom, A. Altmeyer, A. Widera, T. W. Haensch, and I. Bloch. “Quantum phase transition from a superfluid to a Mott insulator in an ultracold gas of atoms”. In: *Physica B: Condensed Matter* 329-333 (2003). Proceedings of the 23rd International Conference on Low Temperature Physics, pp. 11–12. ISSN: 0921-4526. DOI: [https://doi.org/10.1016/S0921-4526\(02\)01872-0](https://doi.org/10.1016/S0921-4526(02)01872-0). URL: <http://www.sciencedirect.com/science/article/pii/S0921452602018720> (cited on page 2).
- [22] S. Jochim, M. Bartenstein, A. Altmeyer, G. Hendl, S. Riedl, C. Chin, J. Hecker Denschlag, and R. Grimm. “Bose-Einstein Condensation of Molecules”. In: *Science* 302.5653 (2003), pp. 2101–2103. ISSN: 0036-8075. DOI: [10.1126/science.1093280](https://doi.org/10.1126/science.1093280). eprint: <https://science.sciencemag.org/content/302/5653/2101.full.pdf>. URL: <https://science.sciencemag.org/content/302/5653/2101> (cited on page 2).
- [23] M. W. Zwierlein, C. A. Stan, C. H. Schunck, S. M. F. Raupach, S. Gupta, Z. Hadzibabic, and W. Ketterle. “Observation of Bose-Einstein Condensation of Molecules”. In: *Phys. Rev. Lett.* 91 (25 2003), p. 250401. DOI: [10.1103/PhysRevLett.91.250401](https://doi.org/10.1103/PhysRevLett.91.250401). URL: <https://link.aps.org/doi/10.1103/PhysRevLett.91.250401> (cited on page 2).
- [24] C. A. Regal, M. Greiner, and D. S. Jin. “Observation of Resonance Condensation of Fermionic Atom Pairs”. In: *Phys. Rev. Lett.* 92 (4 2004), p. 040403. DOI: [10.1103/PhysRevLett.92.040403](https://doi.org/10.1103/PhysRevLett.92.040403). URL: <https://link.aps.org/doi/10.1103/PhysRevLett.92.040403> (cited on page 2).
- [25] H. T. C. Stoof, M. Houbiers, C. A. Sackett, and R. G. Hulet. “Superfluidity of Spin-Polarized ${}^6\text{Li}$ ”. In: *Phys. Rev. Lett.* 76 (1 1996), pp. 10–13. DOI: [10.1103/PhysRevLett.76.10](https://doi.org/10.1103/PhysRevLett.76.10). URL: <https://link.aps.org/doi/10.1103/PhysRevLett.76.10> (cited on page 2).
- [26] C. Chin, M. Bartenstein, A. Altmeyer, S. Riedl, S. Jochim, J. Hecker Denschlag, and R. Grimm. “Observation of the Pairing Gap in a Strongly Interacting Fermi Gas”. In: *Science* 305.5687 (2004), pp. 1128–1130. ISSN: 0036-8075. DOI: [10.1126/science.1100818](https://doi.org/10.1126/science.1100818). eprint: <https://science.sciencemag.org/content/305/5687/1128.full.pdf>. URL: <https://science.sciencemag.org/content/305/5687/1128> (cited on page 2).
- [27] M. W. Zwierlein, J. R. Abo-Shaeer, A. Schirotzek, C. H. Schunck, and W. Ketterle. “Vortices and superfluidity in a strongly interacting Fermi gas”. In: *Nature* 435 (2005). Article, 1047 EP–. URL: <https://doi.org/10.1038/nature03858> (cited on page 2).
- [28] D. Jaksch, C. Bruder, J. I. Cirac, C. W. Gardiner, and P. Zoller. “Cold Bosonic Atoms in Optical Lattices”. In: *Phys. Rev. Lett.* 81 (15 1998), pp. 3108–3111. DOI: [10.1103/PhysRevLett.81.3108](https://doi.org/10.1103/PhysRevLett.81.3108). URL: <https://link.aps.org/doi/10.1103/PhysRevLett.81.3108> (cited on page 2).

- [29] M. Köhl, H. Moritz, T. Stöferle, K. Günter, and T. Esslinger. “Fermionic Atoms in a Three Dimensional Optical Lattice: Observing Fermi Surfaces, Dynamics, and Interactions”. In: *Phys. Rev. Lett.* 94 (8 2005), p. 080403. DOI: [10.1103/PhysRevLett.94.080403](https://doi.org/10.1103/PhysRevLett.94.080403). URL: <https://link.aps.org/doi/10.1103/PhysRevLett.94.080403> (cited on page 2).
- [30] R. Jördens, N. Strohmaier, K. Günter, H. Moritz, and T. Esslinger. “A Mott insulator of fermionic atoms in an optical lattice”. In: *Nature* 455 (2008), 204 EP –. URL: <https://doi.org/10.1038/nature07244> (cited on page 2).
- [31] U. Schneider, L. Hackermüller, S. Will, Th. Best, I. Bloch, T. A. Costi, R. W. Helmes, D. Rasch, and A. Rosch. “Metallic and Insulating Phases of Repulsively Interacting Fermions in a 3D Optical Lattice”. In: *Science* 322.5907 (2008), pp. 1520–1525. ISSN: 0036-8075. DOI: [10.1126/science.1165449](https://doi.org/10.1126/science.1165449). eprint: <https://science.sciencemag.org/content/322/5907/1520.full.pdf>. URL: <https://science.sciencemag.org/content/322/5907/1520> (cited on page 2).
- [32] D. Greif, T. Uehlinger, G. Jotzu, L. Tarruell, and T. Esslinger. “Short-Range Quantum Magnetism of Ultracold Fermions in an Optical Lattice”. In: *Science* 340.6138 (2013), pp. 1307–1310. ISSN: 0036-8075. DOI: [10.1126/science.1236362](https://doi.org/10.1126/science.1236362). eprint: <https://science.sciencemag.org/content/340/6138/1307.full.pdf>. URL: <https://science.sciencemag.org/content/340/6138/1307> (cited on pages 2, 11, 37).
- [33] Russell A. Hart, Pedro M. Duarte, Tsung-Lin Yang, Xinxing Liu, Thereza Paiva, Ehsan Khatami, Richard T. Scalettar, Nandini Trivedi, David A. Huse, and Randall G. Hulet. “Observation of antiferromagnetic correlations in the Hubbard model with ultracold atoms”. In: *Nature* 519.7542 (2015), pp. 211–214. ISSN: 1476-4687. DOI: [10.1038/nature14223](https://doi.org/10.1038/nature14223). URL: <https://doi.org/10.1038/nature14223> (cited on pages 2, 37).
- [34] D. Jaksch and P. Zoller. “The cold atom Hubbard toolbox”. In: *Annals of Physics* 315.1 (2005). Special Issue, pp. 52–79. ISSN: 0003-4916. DOI: <https://doi.org/10.1016/j.aop.2004.09.010>. URL: <http://www.sciencedirect.com/science/article/pii/S0003491604001782> (cited on page 2).
- [35] M. Lewenstein, A. Sanpera, V. Ahufinger, B. Damski, A. Sen(De), and U. Sen. “Ultracold atomic gases in optical lattices: mimicking condensed matter physics and beyond”. In: *Advances in Physics* 56.2 (2007), pp. 243–379. DOI: [10.1080/00018730701223200](https://doi.org/10.1080/00018730701223200). eprint: <https://doi.org/10.1080/00018730701223200>. URL: <https://doi.org/10.1080/00018730701223200> (cited on page 2).
- [36] I. Bloch, J. Dalibard, and W. Zwerger. “Many-body physics with ultracold gases”. In: *Rev. Mod. Phys.* 80 (3 2008), pp. 885–964. DOI: [10.1103/RevModPhys.80.885](https://doi.org/10.1103/RevModPhys.80.885). URL: <https://link.aps.org/doi/10.1103/RevModPhys.80.885> (cited on page 2).
- [37] I. Bloch, J. Dalibard, and S. Nascimbène. “Quantum simulations with ultracold quantum gases”. In: *Nature Physics* 8.4 (2012), pp. 267–276. ISSN: 1745-2481. DOI: [10.1038/nphys2259](https://doi.org/10.1038/nphys2259). URL: <https://doi.org/10.1038/nphys2259> (cited on page 2).

- [38] C. Gross and I. Bloch. “Quantum simulations with ultracold atoms in optical lattices”. In: *Science* 357.6355 (2017), pp. 995–1001. ISSN: 0036-8075. DOI: [10.1126/science.aal3837](https://doi.org/10.1126/science.aal3837). eprint: <https://science.sciencemag.org/content/357/6355/995.full.pdf>. URL: <https://science.sciencemag.org/content/357/6355/995> (cited on page 2).
- [39] C. Kim, A. Y. Matsuura, Z.-X. Shen, N. Motoyama, H. Eisaki, S. Uchida, T. Tohyama, and S. Maekawa. “Observation of Spin-Charge Separation in One-Dimensional SrCuO₂”. In: *Phys. Rev. Lett.* 77.19 (1996), p. 4054. DOI: [10.1103/PhysRevLett.77.4054](https://doi.org/10.1103/PhysRevLett.77.4054). URL: <https://link.aps.org/doi/10.1103/PhysRevLett.77.4054> (cited on pages 2, 49).
- [40] P. Segovia, D. Purdie, M. Hengsberger, and Y. Baer. “Observation of Spin and Charge Collective Modes in One-dimensional Metallic Chains”. In: *Nature* 402 (1999), pp. 504–507. ISSN: 1476-4687. DOI: [10.1038/990052](https://doi.org/10.1038/990052). URL: <https://doi.org/10.1038/990052> (cited on pages 2, 49).
- [41] B. J. Kim, H. Koh, E. Rotenberg, S.-J. Oh, H. Eisaki, N. Motoyama, S. Uchida, T. Tohyama, S. Maekawa, Z.-X. Shen, and C. Kim. “Distinct spinon and holon dispersions in photoemission spectral functions from one-dimensional SrCuO₂”. In: *Nat. Phys.* 2 (2006), pp. 397–401. DOI: [10.1038/nphys316](https://doi.org/10.1038/nphys316). URL: <https://doi.org/10.1038/nphys316> (cited on pages 2, 49).
- [42] A. Damascelli, Z. Hussain, and Z. Shen. “Angle-resolved photoemission studies of the cuprate superconductors”. In: *Rev. Mod. Phys.* 75 (2 2003), pp. 473–541. DOI: [10.1103/RevModPhys.75.473](https://doi.org/10.1103/RevModPhys.75.473). URL: <https://link.aps.org/doi/10.1103/RevModPhys.75.473> (cited on page 2).
- [43] P. A. Lee, N. Nagaosa, and X.-G. Wen. “Doping a Mott insulator: Physics of high-temperature superconductivity”. In: *Rev. Mod. Phys.* 78 (1 2006), pp. 17–85. DOI: [10.1103/RevModPhys.78.17](https://doi.org/10.1103/RevModPhys.78.17). URL: <https://link.aps.org/doi/10.1103/RevModPhys.78.17> (cited on pages 2, 10, 77).
- [44] O. M. Auslaender, H. Steinberg, A. Yacoby, Y. Tserkovnyak, B. I. Halperin, K. W. Baldwin, L. N. Pfeiffer, and K. W. West. “Spin-Charge Separation and Localization in One Dimension”. In: *Science* 308.5718 (2005), pp. 88–92. ISSN: 0036-8075. DOI: [10.1126/science.1107821](https://doi.org/10.1126/science.1107821). URL: <http://science.sciencemag.org/content/308/5718/88> (cited on pages 2, 49).
- [45] Y. Jompol, C. J. B. Ford, J. P. Griffiths, I. Farrer, G. A. C. Jones, D. Anderson, D. A. Ritchie, T. W. Silk, and A. J. Schofield. “Probing Spin-Charge Separation in a Tomonaga-Luttinger Liquid”. In: *Science* 325.5940 (2009), pp. 597–601. ISSN: 0036-8075. DOI: [10.1126/science.1171769](https://doi.org/10.1126/science.1171769). URL: <http://science.sciencemag.org/content/325/5940/597> (cited on pages 2, 49).
- [46] Y. Tserkovnyak, B. I. Halperin, O. M. Auslaender, and A. Yacoby. “Interference and zero-bias anomaly in tunneling between Luttinger-liquid wires”. In: *Phys. Rev. B* 68.12 (2003), p. 125312. DOI: [10.1103/PhysRevB.68.125312](https://doi.org/10.1103/PhysRevB.68.125312). URL: <https://link.aps.org/doi/10.1103/PhysRevB.68.125312> (cited on pages 2, 49).
- [47] S. Watanabe, K. Ando, K. Kang, S. Mooser, Y. Vaynzof, H. Kurebayashi, E. Saitoh, and H. Sirringhaus. “Polaron spin current transport in organic semiconductors”. In: *Nature Physics* 10.4 (2014), pp. 308–313. ISSN: 1745-2481. DOI: [10.1038/nphys2901](https://doi.org/10.1038/nphys2901). URL: <https://doi.org/10.1038/nphys2901> (cited on page 2).

- [48] R. M. Kusters, J. Singleton, D. A. Keen, R. McGreevy, and W. Hayes. “Magnetoresistance measurements on the magnetic semiconductor $\text{Nd}_{0.5}\text{Pb}_{0.5}\text{MnO}_3$ ”. In: *Physica B: Condensed Matter* 155.1 (1989), pp. 362–365. ISSN: 0921-4526. DOI: [https://doi.org/10.1016/0921-4526\(89\)90530-9](https://doi.org/10.1016/0921-4526(89)90530-9). URL: <http://www.sciencedirect.com/science/article/pii/0921452689905309> (cited on page 2).
- [49] M. Jaime, H. T. Hardner, M. B. Salamon, M. Rubinstein, P. Dorsey, and D. Emin. “Hall-Effect Sign Anomaly and Small-Polaron Conduction in $(\text{La}_{1-x}\text{Gd}_x)_{0.67}\text{Ca}_{0.33}\text{MnO}_3$ ”. In: *Phys. Rev. Lett.* 78 (5 1997), pp. 951–954. DOI: [10.1103/PhysRevLett.78.951](https://doi.org/10.1103/PhysRevLett.78.951). URL: <https://link.aps.org/doi/10.1103/PhysRevLett.78.951> (cited on page 2).
- [50] N. D. Mathur, G. Burnell, S. P. Isaac, T. J. Jackson, B.-S. Teo, J. L. MacManus-Driscoll, L. F. Cohen, J. E. Evetts, and M. G. Blamire. “Large low-field magnetoresistance in $\text{La}_{0.7}\text{Ca}_{0.3}\text{MnO}_3$ induced by artificial grain boundaries”. In: *Nature* 387.6630 (1997), pp. 266–268. ISSN: 1476-4687. DOI: [10.1038/387266a0](https://doi.org/10.1038/387266a0). URL: <https://doi.org/10.1038/387266a0> (cited on page 2).
- [51] K. D. Nelson, L. Xiao, and D. S. Weiss. “Imaging single atoms in a three-dimensional array”. In: *Nature Physics* 3 (2007), pp. 556–560. ISSN: 1745-2473. DOI: [10.1038/nphys645](https://doi.org/10.1038/nphys645) (cited on page 2).
- [52] M. Karski, L. Förster, J. M. Choi, W. Alt, A. Widera, and D. Meschede. “Nearest-Neighbor Detection of Atoms in a 1D Optical Lattice by Fluorescence Imaging”. In: *Phys. Rev. Lett.* 102 (5 2009), p. 053001. DOI: [10.1103/PhysRevLett.102.053001](https://doi.org/10.1103/PhysRevLett.102.053001). URL: <https://link.aps.org/doi/10.1103/PhysRevLett.102.053001> (cited on page 2).
- [53] W. S. Bakr, J. I. Gillen, A. Peng, S. Fölling, and M. Greiner. “A quantum gas microscope for detecting single atoms in a Hubbard-regime optical lattice”. In: *Nature* 462.7269 (2009), pp. 74–77. ISSN: 1476-4687. DOI: [10.1038/nature08482](https://doi.org/10.1038/nature08482). URL: <https://doi.org/10.1038/nature08482> (cited on page 2).
- [54] J. F. Sherson, C. Weitenberg, M. Endres, M. Cheneau, I. Bloch, and S. Kuhr. “Single-atom-resolved fluorescence imaging of an atomic Mott insulator”. In: *Nature* 467.7311 (2010), pp. 68–72. ISSN: 1476-4687. DOI: [10.1038/nature09378](https://doi.org/10.1038/nature09378). URL: <https://doi.org/10.1038/nature09378> (cited on page 2).
- [55] N. Gemelke, X. Zhang, C.-L. Hung, and C. Chin. “In situ observation of incompressible Mott-insulating domains in ultracold atomic gases”. In: *Nature* 460.7258 (2009), pp. 995–998. ISSN: 1476-4687. DOI: [10.1038/nature08244](https://doi.org/10.1038/nature08244). URL: <https://doi.org/10.1038/nature08244> (cited on page 2).
- [56] W. S. Bakr, A. Peng, M. E. Tai, R. Ma, J. Simon, J. I. Gillen, S. Fölling, L. Pollet, and M. Greiner. “Probing the Superfluid-to-Mott Insulator Transition at the Single-Atom Level”. In: *Science* 329.5991 (2010), pp. 547–550. ISSN: 0036-8075. DOI: [10.1126/science.1192368](https://doi.org/10.1126/science.1192368). eprint: <https://science.sciencemag.org/content/329/5991/547.full.pdf>. URL: <https://science.sciencemag.org/content/329/5991/547> (cited on page 2).
- [57] M. Cheneau, P. Barmettler, D. Poletti, M. Endres, P. Schauß, T. Fukuhara, C. Gross, I. Bloch, C. Kollath, and S. Kuhr. “Light-cone-like spreading of correlations in a quantum many-body system”. In: *Nature* 481.7382 (2012), pp. 484–487. ISSN: 1476-4687. DOI: [10.1038/nature10748](https://doi.org/10.1038/nature10748). URL: <https://doi.org/10.1038/nature10748> (cited on page 2).

- [58] J. Simon, W. S. Bakr, R. Ma, M. E. Tai, P. M. Preiss, and M. Greiner. “Quantum simulation of antiferromagnetic spin chains in an optical lattice”. In: *Nature* 472.7343 (2011), pp. 307–312. ISSN: 1476-4687. DOI: [10.1038/nature09994](https://doi.org/10.1038/nature09994). URL: <https://doi.org/10.1038/nature09994> (cited on page 3).
- [59] M. Endres, M. Cheneau, T. Fukuhara, C. Weitenberg, P. Schauß, C. Gross, L. Mazza, M. C. Bañuls, L. Pollet, I. Bloch, and S. Kuhr. “Observation of Correlated Particle-Hole Pairs and String Order in Low-Dimensional Mott Insulators”. In: *Science* 334.6053 (2011), pp. 200–203. ISSN: 0036-8075. DOI: [10.1126/science.1209284](https://doi.org/10.1126/science.1209284). eprint: <https://science.sciencemag.org/content/334/6053/200.full.pdf>. URL: <https://science.sciencemag.org/content/334/6053/200> (cited on page 3).
- [60] T. Fukuhara, A. Kantian, M. Endres, M. Cheneau, P. Schauß, S. Hild, D. Bellem, U. Schollwöck, T. Giamarchi, C. Gross, I. Bloch, and S. Kuhr. “Quantum dynamics of a mobile spin impurity”. In: *Nature Physics* 9 (2013). Article, 235 EP –. URL: <https://doi.org/10.1038/nphys2561> (cited on page 3).
- [61] P. M. Preiss, R. Ma, M. E. Tai, J. Simon, and M. Greiner. “Quantum gas microscopy with spin, atom-number, and multilayer readout”. In: *Phys. Rev. A* 91 (4 2015), p. 041602. DOI: [10.1103/PhysRevA.91.041602](https://doi.org/10.1103/PhysRevA.91.041602). URL: <https://link.aps.org/doi/10.1103/PhysRevA.91.041602> (cited on page 3).
- [62] T. Fukuhara, P. Schauß, M. Endres, S. Hild, M. Cheneau, I. Bloch, and C. Gross. “Microscopic observation of magnon bound states and their dynamics”. In: *Nature* 502 (2013), 76 EP –. URL: <https://doi.org/10.1038/nature12541> (cited on page 3).
- [63] R. Islam, R. Ma, P. M. Preiss, M. Eric Tai, A. Lukin, M. Rispoli, and M. Greiner. “Measuring entanglement entropy in a quantum many-body system”. In: *Nature* 528.7580 (2015), pp. 77–83. ISSN: 1476-4687. DOI: [10.1038/nature15750](https://doi.org/10.1038/nature15750). URL: <https://doi.org/10.1038/nature15750> (cited on page 3).
- [64] E. Haller, J. Hudson, A. Kelly, D. A. Cotta, B. Peaudecerf, G. D. Bruce, and S. Kuhr. “Single-atom imaging of fermions in a quantum-gas microscope”. In: *Nature Physics* 11.9 (2015), pp. 738–742. ISSN: 1745-2481. DOI: [10.1038/nphys3403](https://doi.org/10.1038/nphys3403). URL: <https://doi.org/10.1038/nphys3403> (cited on page 3).
- [65] L. W. Cheuk, M. A. Nichols, M. Okan, T. Gersdorf, V. V. Ramasesh, W. S. Bakr, T. Lompe, and M. W. Zwierlein. “Quantum-Gas Microscope for Fermionic Atoms”. In: *Phys. Rev. Lett.* 114 (19 2015), p. 193001. DOI: [10.1103/PhysRevLett.114.193001](https://doi.org/10.1103/PhysRevLett.114.193001). URL: <https://link.aps.org/doi/10.1103/PhysRevLett.114.193001> (cited on page 3).
- [66] M. F. Parsons, F. Huber, A. Mazurenko, C. S. Chiu, W. Setiawan, K. Wooley-Brown, S. Blatt, and M. Greiner. “Site-Resolved Imaging of Fermionic ${}^6\text{Li}$ in an Optical Lattice”. In: *Phys. Rev. Lett.* 114 (21 2015), p. 213002. DOI: [10.1103/PhysRevLett.114.213002](https://doi.org/10.1103/PhysRevLett.114.213002). URL: <https://link.aps.org/doi/10.1103/PhysRevLett.114.213002> (cited on page 3).
- [67] A. Omran, M. Boll, T. A. Hilker, K. Kleinlein, G. Salomon, I. Bloch, and C. Gross. “Microscopic Observation of Pauli Blocking in Degenerate Fermionic Lattice Gases”. In: *Phys. Rev. Lett.* 115.26 (2015), p. 263001. DOI: [10.1103/PhysRevLett.115.263001](https://doi.org/10.1103/PhysRevLett.115.263001) (cited on page 3).

- [68] R. Yamamoto, J. Kobayashi, T. Kuno, K. Kato, and Y. Takahashi. “An ytterbium quantum gas microscope with narrow-line laser cooling”. In: *New J. Phys.* 18 (2 2016), p. 023016. DOI: [10.1088/1367-2630/18/2/023016](https://doi.org/10.1088/1367-2630/18/2/023016). URL: <https://iopscience.iop.org/article/10.1088/1367-2630/18/2/023016> (cited on page 3).
- [69] M. Miranda, R. Inoue, Y. Okuyama, A. Nakamoto, and M. Kozuma. “Site-resolved imaging of ytterbium atoms in a two-dimensional optical lattice”. In: *Phys. Rev. A* 91 (6 2015), p. 063414. DOI: [10.1103/PhysRevA.91.063414](https://doi.org/10.1103/PhysRevA.91.063414). URL: <https://link.aps.org/doi/10.1103/PhysRevA.91.063414> (cited on page 3).
- [70] D. Greif, M. F. Parsons, A. Mazurenko, C. S. Chiu, S. Blatt, F. Huber, G. Ji, and M. Greiner. “Site-resolved imaging of a fermionic Mott insulator”. In: *Science* 351.6276 (2016), pp. 953–957. ISSN: 0036-8075. DOI: [10.1126/science.aad9041](https://doi.org/10.1126/science.aad9041). eprint: <https://science.sciencemag.org/content/351/6276/953.full.pdf>. URL: <https://science.sciencemag.org/content/351/6276/953> (cited on page 3).
- [71] L. W. Cheuk, M. A. Nichols, K. R. Lawrence, M. Okan, H. Zhang, E. Khatami, N. Trivedi, T. Paiva, M. Rigol, and M. W. Zwierlein. “Observation of spatial charge and spin correlations in the 2D Fermi-Hubbard model”. In: *Science* 353.6305 (2016), pp. 1260–1264. ISSN: 0036-8075. DOI: [10.1126/science.aag3349](https://doi.org/10.1126/science.aag3349). URL: <http://science.sciencemag.org/content/353/6305/1260> (cited on pages 3, 35, 37).
- [72] M. F. Parsons, A. Mazurenko, C. S. Chiu, G. Ji, D. Greif, and M. Greiner. “Site-resolved measurement of the spin-correlation function in the Fermi-Hubbard model”. In: *Science* 353.6305 (2016), pp. 1253–1256. ISSN: 0036-8075. DOI: [10.1126/science.aag1430](https://doi.org/10.1126/science.aag1430). URL: <http://science.sciencemag.org/content/353/6305/1253> (cited on pages 3, 35, 37, 79).
- [73] M. Boll, T. A. Hilker, G. Salomon, A. Omran, J. Nespolo, L. Pollet, I. Bloch, and C. Gross. “Spin- and density-resolved microscopy of antiferromagnetic correlations in Fermi-Hubbard chains”. In: *Science* 353.6305 (2016), pp. 1257–1260. ISSN: 0036-8075. DOI: [10.1126/science.aag1635](https://doi.org/10.1126/science.aag1635). URL: <http://science.sciencemag.org/content/353/6305/1257> (cited on pages 3, 35).
- [74] A. Mazurenko, C. S. Chiu, G. Ji, M. F. Parsons, M. Kanász-Nagy, R. Schmidt, F. Grusdt, E. Demler, D. Greif, and M. Greiner. “A cold-atom Fermi-Hubbard antiferromagnet”. In: *Nature* 545 (2017), 462 EP –. ISSN: 1476-4687. DOI: [10.1038/nature22362](https://doi.org/10.1038/nature22362). URL: <https://doi.org/10.1038/nature22362> (cited on pages 3, 85, 90).
- [75] T. Giamarchi. *Quantum physics in one dimension*. Oxford: Clarendon, 2004. ISBN: 0198525001 (cited on pages 4, 14, 15, 22, 37, 58).
- [76] T. Hilker. “Spin-resolved microscopy of strongly correlated fermionic many-body states”. 2017. URL: <http://nbn-resolving.de/urn:nbn:de:bvb:19-216330> (cited on pages 7, 37).
- [77] M. C. Gutzwiller. “Effect of Correlation on the Ferromagnetism of Transition Metals”. In: *Phys. Rev. Lett.* 10 (5 1963), pp. 159–162. DOI: [10.1103/PhysRevLett.10.159](https://doi.org/10.1103/PhysRevLett.10.159). URL: <https://link.aps.org/doi/10.1103/PhysRevLett.10.159> (cited on page 7).

- [78] J. Hubbard. “Electron correlations in narrow energy bands”. In: *Proc. R. Soc. Lond. A* 276 (1365 1963), pp. 238–257. DOI: [10.1098/rspa.1963.0204](https://doi.org/10.1098/rspa.1963.0204). URL: <https://royalsocietypublishing.org/doi/10.1098/rspa.1963.0204> (cited on page 7).
- [79] S. A. Jafari. “Introduction to Hubbard Model and Exact Diagonalization”. In: *Iranian J. Phys. Res.* 8 (2 2008), p. 113 (cited on page 7).
- [80] B. Keimer, S. A. Kivelson, M. R. Norman, S. Uchida, and J. Zaanen. “From quantum matter to high-temperature superconductivity in copper oxides”. In: *Nature* 518.7538 (2015), pp. 179–186. ISSN: 1476-4687. DOI: [10.1038/nature14165](https://doi.org/10.1038/nature14165). URL: <https://doi.org/10.1038/nature14165> (cited on page 9).
- [81] J. M. Singer, M. H. Pedersen, T. Schneider, H. Beck, and H.-G. Matuttis. “From BCS-like superconductivity to condensation of local pairs: A numerical study of the attractive Hubbard model”. In: *Phys. Rev. B* 54 (2 1996), pp. 1286–1301. DOI: [10.1103/PhysRevB.54.1286](https://link.aps.org/doi/10.1103/PhysRevB.54.1286). URL: <https://link.aps.org/doi/10.1103/PhysRevB.54.1286> (cited on page 8).
- [82] A. F. Ho, M. A. Cazalilla, and T. Giamarchi. “Quantum simulation of the Hubbard model: The attractive route”. In: *Phys. Rev. A* 79 (3 2009), p. 033620. DOI: [10.1103/PhysRevA.79.033620](https://link.aps.org/doi/10.1103/PhysRevA.79.033620). URL: <https://link.aps.org/doi/10.1103/PhysRevA.79.033620> (cited on page 8).
- [83] T. Kinoshita, T. Wenger, and D. S. Weiss. “Observation of a one-dimensional Tonks-Girardeau gas”. In: *Science* 305.5687 (2004), pp. 1125–1128. DOI: [10.1126/science.1100700](https://doi.org/10.1126/science.1100700) (cited on page 8).
- [84] B. Paredes, A. Widera, V. Murg, O. Mandel, S. Fölling, I. Cirac, G. V. Shlyapnikov, T. W. Hänsch, and I. Bloch. “Tonks–Girardeau gas of ultracold atoms in an optical lattice”. In: *Nature* 429.6989 (2004), p. 277. ISSN: 1476-4687. DOI: [10.1038/nature02530](https://www.nature.com/articles/nature02530). URL: <https://www.nature.com/articles/nature02530.pdf> (cited on page 8).
- [85] N. Strohmaier, Y. Takasu, K. Günter, R. Jördens, M. Köhl, H. Moritz, and T. Esslinger. “Interaction-Controlled Transport of an Ultracold Fermi Gas”. In: *Phys. Rev. Lett.* 99 (22 2007), p. 220601. DOI: [10.1103/PhysRevLett.99.220601](https://link.aps.org/doi/10.1103/PhysRevLett.99.220601). URL: <https://link.aps.org/doi/10.1103/PhysRevLett.99.220601> (cited on page 8).
- [86] E. Haller, M. Gustavsson, M. J. Mark, J. G. Danzl, R. Hart, G. Pupillo, and H.-C. Nägerl. “Realization of an excited, strongly correlated quantum gas phase”. In: *Science* 325.5945 (2009), pp. 1224–1227. DOI: [10.1126/science.1175850](https://doi.org/10.1126/science.1175850) (cited on page 8).
- [87] L. Hackermüller, U. Schneider, M. Moreno-Cardoner, T. Kitagawa, T. Best, S. Will, E. Demler, E. Altman, I. Bloch, and B. Paredes. “Anomalous Expansion of Attractively Interacting Fermionic Atoms in an Optical Lattice”. In: *Science* 327.5973 (2010), p. 1621. DOI: [10.1126/science.1184565](http://science.sciencemag.org/content/327/5973/1621.abstract). URL: <http://science.sciencemag.org/content/327/5973/1621.abstract> (cited on page 8).
- [88] T. Jacqmin, J. Armijo, T. Berrada, K. V. Kheruntsyan, and I. Bouchoule. “Sub-Poissonian fluctuations in a 1D Bose gas: from the quantum quasicondensate to the strongly interacting regime”. In: *Phys. Rev. Lett.* 106.23 (2011), p. 230405. DOI: [10.1103/PhysRevLett.106.230405](https://doi.org/10.1103/PhysRevLett.106.230405) (cited on page 8).

- [89] U. Schneider, L. Hackermüller, J. P. Ronzheimer, S. Will, S. Braun, T. Best, I. Bloch, E. Demler, S. Mandt, D. Rasch, and A. Rosch. “Fermionic transport and out-of-equilibrium dynamics in a homogeneous Hubbard model with ultracold atoms”. In: *Nature Physics* 8.3 (2012), pp. 213–218. ISSN: 1745-2481. DOI: [10.1038/nphys2205](https://doi.org/10.1038/nphys2205). URL: <https://doi.org/10.1038/nphys2205> (cited on page 8).
- [90] N. Fabbri, M. Panfil, D. Clément, L. Fallani, M. Inguscio, C. Fort, and J.-S. Caux. “Dynamical structure factor of one-dimensional Bose gases: Experimental signatures of beyond-Luttinger-liquid physics”. In: *Phys. Rev. A* 91.4 (2015), p. 043617. DOI: [10.1103/PhysRevA.91.043617](https://doi.org/10.1103/PhysRevA.91.043617). URL: <http://link.aps.org/pdf/10.1103/PhysRevA.91.043617> (cited on page 8).
- [91] D. Mitra, P. T. Brown, E. Guardado-Sanchez, S. S. Kondov, T. Devakul, D. A. Huse, P. Schauß, and W. S. Bakr. “Quantum gas microscopy of an attractive Fermi-Hubbard system”. In: *Nature Physics* 14.2 (2018), pp. 173–177. ISSN: 1745-2481. DOI: [10.1038/nphys4297](https://doi.org/10.1038/nphys4297). URL: <https://doi.org/10.1038/nphys4297> (cited on page 8).
- [92] M. Gall, C. F. Chan, N. Wurz, and M. Köhl. “Simulating a Mott insulator using attractive interaction”. In: (2019). arXiv: [1907.09045](https://arxiv.org/abs/1907.09045) [cond-mat.quant-gas] (cited on page 8).
- [93] F. Bloch. “Über die Quantenmechanik der Elektronen in Kristallgittern”. In: *Zeitschrift für Physik* 52.7 (1929), pp. 555–600. ISSN: 0044-3328. DOI: [10.1007/BF01339455](https://doi.org/10.1007/BF01339455). URL: <https://doi.org/10.1007/BF01339455> (cited on page 9).
- [94] M. V. Sadovskii. “Pseudogap in high-temperature superconductors”. In: *Physics-Uspekhii* 44.5 (2001), pp. 515–539. DOI: [10.1070/pu2001v044n05abeh000902](https://doi.org/10.1070/pu2001v044n05abeh000902). URL: <https://doi.org/10.1070%2Fpu2001v044n05ab%2F000902> (cited on page 10).
- [95] T. Timusk and B. Statt. “The pseudogap in high-temperature superconductors: an experimental survey”. In: *Reports on Progress in Physics* 62.1 (1999), pp. 61–122. DOI: [10.1088/0034-4885/62/1/002](https://doi.org/10.1088/0034-4885/62/1/002). URL: <https://doi.org/10.1088%2F0034-4885%2F62%2F1%2F002> (cited on page 10).
- [96] H. J. Schulz. “Incommensurate antiferromagnetism in the two-dimensional Hubbard model”. In: *Phys. Rev. Lett.* 64 (12 1990), pp. 1445–1448. DOI: [10.1103/PhysRevLett.64.1445](https://doi.org/10.1103/PhysRevLett.64.1445). URL: <https://link.aps.org/doi/10.1103/PhysRevLett.64.1445> (cited on pages 10, 87).
- [97] W. Hofstetter, J. I. Cirac, P. Zoller, E. Demler, and M. D. Lukin. “High-Temperature Superfluidity of Fermionic Atoms in Optical Lattices”. In: *Phys. Rev. Lett.* 89 (22 2002), p. 220407. DOI: [10.1103/PhysRevLett.89.220407](https://doi.org/10.1103/PhysRevLett.89.220407). URL: <https://link.aps.org/doi/10.1103/PhysRevLett.89.220407> (cited on page 10).
- [98] Karyn Le Hur and T. Maurice Rice. “Superconductivity close to the Mott state: From condensed-matter systems to superfluidity in optical lattices”. In: *Annals of Physics* 324.7 (2009). July 2009 Special Issue, pp. 1452–1515. ISSN: 0003-4916. DOI: <https://doi.org/10.1016/j.aop.2009.02.004>. URL: <http://www.sciencedirect.com/science/article/pii/S0003491609000451> (cited on page 10).

- [99] A. Auerbach. *Interacting Electrons and Quantum Magnetism*. Graduate Texts in Contemporary Physics. New York, NY: Springer, 1994. ISBN: 9781461269281. DOI: [10.1007/978-1-4612-0869-3](https://doi.org/10.1007/978-1-4612-0869-3). URL: <http://dx.doi.org/10.1007/978-1-4612-0869-3> (cited on pages 10, 18, 59).
- [100] Y. Nagaoka. “Ferromagnetism in a Narrow, Almost Half-Filled s Band”. In: *Phys. Rev.* 147 (1 1966), pp. 392–405. DOI: [10.1103/PhysRev.147.392](https://doi.org/10.1103/PhysRev.147.392). URL: <https://link.aps.org/doi/10.1103/PhysRev.147.392> (cited on pages 10, 88).
- [101] H. Tasaki. “From Nagaoka’s Ferromagnetism to Flat-Band Ferromagnetism and Beyond: An Introduction to Ferromagnetism in the Hubbard Model”. In: *Progress of Theoretical Physics* 99.4 (Apr. 1998), pp. 489–548. ISSN: 0033-068X. DOI: [10.1143/PTP.99.489](https://doi.org/10.1143/PTP.99.489). eprint: <http://oup.prod.sis.lan/ptp/article-pdf/99/4/489/5209512/99-4-489.pdf>. URL: <https://doi.org/10.1143/PTP.99.489> (cited on page 10).
- [102] L. Duca, T. Li, M. Reitter, I. Bloch, M. Schleier-Smith, and U. Schneider. “An Aharonov-Bohm interferometer for determining Bloch band topology”. In: *Science* 347.6219 (2015), pp. 288–292. ISSN: 0036-8075. DOI: [10.1126/science.1259052](https://doi.org/10.1126/science.1259052). eprint: <https://science.sciencemag.org/content/347/6219/288.full.pdf>. URL: <https://science.sciencemag.org/content/347/6219/288> (cited on page 11).
- [103] K. Viebahn, M. Sbroscia, E. Carter, J-C. Yu, and U. Schneider. “Matter-Wave Diffraction from a Quasicrystalline Optical Lattice”. In: *Phys. Rev. Lett.* 122 (11 2019), p. 110404. DOI: [10.1103/PhysRevLett.122.110404](https://doi.org/10.1103/PhysRevLett.122.110404). URL: <https://link.aps.org/doi/10.1103/PhysRevLett.122.110404> (cited on page 11).
- [104] N. W. Ashcroft and N. D. Mermin. *Solid State Physics*. Saunders College, Philadelphia, 1976 (cited on page 12).
- [105] C. Pethick and H. Smith. *Bose–Einstein Condensation in Dilute Gases*. Cambridge University Press, 2008. DOI: [10.1017/CB09780511802850](https://doi.org/10.1017/CB09780511802850) (cited on page 12).
- [106] C. Chin, R. Grimm, P. Julienne, and E. Tiesinga. “Feshbach resonances in ultracold gases”. In: *Rev. Mod. Phys.* 82 (2 2010), pp. 1225–1286. DOI: [10.1103/RevModPhys.82.1225](https://doi.org/10.1103/RevModPhys.82.1225). URL: <https://link.aps.org/doi/10.1103/RevModPhys.82.1225> (cited on page 13).
- [107] T. Giamarchi. “One-dimensional physics in the 21st century”. In: *Comptes Rendus Physique* 17.3 (2016). Physique de la matière condensée au XXIe siècle: l’héritage de Jacques Friedel, pp. 322–331. ISSN: 1631-0705. DOI: <https://doi.org/10.1016/j.crhy.2015.11.009>. URL: <http://www.sciencedirect.com/science/article/pii/S1631070515002261> (cited on pages 13, 15).
- [108] M. B. Stone, D. H. Reich, C. Broholm, K. Lefmann, C. Rischel, C. P. Landee, and M. M. Turnbull. “Extended Quantum Critical Phase in a Magnetized Spin- $\frac{1}{2}$ Antiferromagnetic Chain”. In: *Phys. Rev. Lett.* 91 (3 2003), p. 037205. DOI: [10.1103/PhysRevLett.91.037205](https://doi.org/10.1103/PhysRevLett.91.037205). URL: <https://link.aps.org/doi/10.1103/PhysRevLett.91.037205> (cited on page 13).
- [109] B. Lake, D. A. Tennant, C. D. Frost, and S. E. Nagler. “Quantum criticality and universal scaling of a quantum antiferromagnet”. In: *Nature Materials* 4.4 (2005), pp. 329–334. ISSN: 1476-4660. DOI: [10.1038/nmat1327](https://doi.org/10.1038/nmat1327). URL: <https://doi.org/10.1038/nmat1327> (cited on pages 13, 78).

- [110] M. Klanjšek, H. Mayaffre, C. Berthier, B. Chiari, O. Piovesana, P. Bouillot, C. Kollath, E. Orignac, R. Citro, and T. Giamarchi. “Controlling Luttinger Liquid Physics in Spin Ladders under a Magnetic Field”. In: *Phys. Rev. Lett.* 101 (13 2008), p. 137207. DOI: [10.1103/PhysRevLett.101.137207](https://doi.org/10.1103/PhysRevLett.101.137207). URL: <https://link.aps.org/doi/10.1103/PhysRevLett.101.137207> (cited on page 13).
- [111] M. Bockrath, D. H. Cobden, J. Lu, A. G. Rinzler, R. E. Smalley, L. Balents, and P. L. McEuen. “Luttinger-liquid behaviour in carbon nanotubes”. In: *Nature* 397.6720 (13 1999), pp. 598–601. ISSN: 1476-4687. DOI: [10.1038/17569](https://doi.org/10.1038/17569). URL: <https://doi.org/10.1038/17569> (cited on page 13).
- [112] J. Lee, S. Eggert, H. Kim, S.-J. Kahng, H. Shinohara, and Y. Kuk. “Real Space Imaging of One-Dimensional Standing Waves: Direct Evidence for a Luttinger Liquid”. In: *Phys. Rev. Lett.* 93 (16 2004), p. 166403. DOI: [10.1103/PhysRevLett.93.166403](https://doi.org/10.1103/PhysRevLett.93.166403). URL: <https://link.aps.org/doi/10.1103/PhysRevLett.93.166403> (cited on page 13).
- [113] H. Frahm and V. E. Korepin. “Correlation functions of the one-dimensional Hubbard model in a magnetic field”. In: *Phys. Rev. B* 43 (7 1991), pp. 5653–5662. DOI: [10.1103/PhysRevB.43.5653](https://doi.org/10.1103/PhysRevB.43.5653). URL: <https://link.aps.org/doi/10.1103/PhysRevB.43.5653> (cited on pages 14, 39).
- [114] C. Kollath and U. Schollwöck. “Cold Fermi gases: a new perspective on spin-charge separation”. In: *New J. Phys.* 8.10 (13 2006), p. 220. DOI: [10.1088/1367-2630/8/10/220](https://doi.org/10.1088/1367-2630/8/10/220). URL: <https://doi.org/10.1088/1367-2630/8/10/220> (cited on pages 15, 49).
- [115] F. D. M. Haldane. “Effective Harmonic-Fluid Approach to Low-Energy Properties of One-Dimensional Quantum Fluids”. In: *Phys. Rev. Lett.* 47 (25 1981), pp. 1840–1843. DOI: [10.1103/PhysRevLett.47.1840](https://doi.org/10.1103/PhysRevLett.47.1840). URL: <https://link.aps.org/doi/10.1103/PhysRevLett.47.1840> (cited on page 15).
- [116] F. Woynarovich. “Excitations with complex wavenumbers in a Hubbard chain. I. States with one pair of complex wavenumbers”. In: *Journal of Physics C: Solid State Physics* 15.1 (13 1982), pp. 85–96. DOI: [10.1088/0022-3719/15/1/007](https://doi.org/10.1088/0022-3719/15/1/007). URL: <https://doi.org/10.1088/0022-3719/15/1/007> (cited on pages 18, 44, 59).
- [117] M. Ogata and H. Shiba. “Bethe-ansatz wave function, momentum distribution, and spin correlation in the one-dimensional strongly correlated Hubbard model”. In: *Phys. Rev. B* 41.4 (13 1990), pp. 2326–2338. DOI: [10.1103/PhysRevB.41.2326](https://doi.org/10.1103/PhysRevB.41.2326). URL: <https://link.aps.org/doi/10.1103/PhysRevB.41.2326> (cited on pages 18, 44, 57, 59).
- [118] C. F. Coll. “Excitation spectrum of the one-dimensional Hubbard model”. In: *Phys. Rev. B* 9 (5 1974), pp. 2150–2158. DOI: [10.1103/PhysRevB.9.2150](https://doi.org/10.1103/PhysRevB.9.2150). URL: <https://link.aps.org/doi/10.1103/PhysRevB.9.2150> (cited on page 20).
- [119] S. Schmitt-Rink, C. M. Varma, and A. E. Ruckenstein. “Spectral Function of Holes in a Quantum Antiferromagnet”. In: *Phys. Rev. Lett.* 60 (26 1988), pp. 2793–2796. DOI: [10.1103/PhysRevLett.60.2793](https://doi.org/10.1103/PhysRevLett.60.2793). URL: <https://link.aps.org/doi/10.1103/PhysRevLett.60.2793> (cited on pages 22, 77).
- [120] B. I. Shraiman and E. D. Siggia. “Mobile Vacancies in a Quantum Heisenberg Antiferromagnet”. In: *Phys. Rev. Lett.* 61 (4 1988), pp. 467–470. DOI: [10.1103/PhysRevLett.61.467](https://doi.org/10.1103/PhysRevLett.61.467). URL: <https://link.aps.org/doi/10.1103/PhysRevLett.61.467> (cited on pages 22, 77).

- [121] S. Sachdev. “Hole motion in a quantum Néel state”. In: *Phys. Rev. B* 39 (16 1989), pp. 12232–12247. DOI: [10.1103/PhysRevB.39.12232](https://doi.org/10.1103/PhysRevB.39.12232). URL: <https://link.aps.org/doi/10.1103/PhysRevB.39.12232> (cited on pages 22, 77).
- [122] C. L. Kane, P. A. Lee, and N. Read. “Motion of a single hole in a quantum antiferromagnet”. In: *Phys. Rev. B* 39 (10 1989), pp. 6880–6897. DOI: [10.1103/PhysRevB.39.6880](https://doi.org/10.1103/PhysRevB.39.6880). URL: <https://link.aps.org/doi/10.1103/PhysRevB.39.6880> (cited on pages 22, 77).
- [123] E. Dagotto, A. Moreo, and T. Barnes. “Hubbard model with one hole: Ground-state properties”. In: *Phys. Rev. B* 40 (10 1989), pp. 6721–6725. DOI: [10.1103/PhysRevB.40.6721](https://doi.org/10.1103/PhysRevB.40.6721). URL: <https://link.aps.org/doi/10.1103/PhysRevB.40.6721> (cited on page 22).
- [124] F. Grusdt, M. Kánasz-Nagy, A. Bohrdt, C. S. Chiu, G. Ji, M. Greiner, D. Greif, and E. Demler. “Parton Theory of Magnetic Polarons: Mesonic Resonances and Signatures in Dynamics”. In: *Phys. Rev. X* 8 (1 2018), p. 011046. DOI: [10.1103/PhysRevX.8.011046](https://doi.org/10.1103/PhysRevX.8.011046). URL: <https://link.aps.org/doi/10.1103/PhysRevX.8.011046> (cited on pages 22, 23).
- [125] W. F. Brinkman and T. M. Rice. “Single-Particle Excitations in Magnetic Insulators”. In: *Phys. Rev. B* 2 (5 1970), pp. 1324–1338. DOI: [10.1103/PhysRevB.2.1324](https://doi.org/10.1103/PhysRevB.2.1324). URL: <https://link.aps.org/doi/10.1103/PhysRevB.2.1324> (cited on page 23).
- [126] D. Elbio. “Correlated electrons in high-temperature superconductors”. In: *Rev. Mod. Phys.* 66 (3 1994), pp. 763–840. DOI: [10.1103/RevModPhys.66.763](https://doi.org/10.1103/RevModPhys.66.763). URL: <https://link.aps.org/doi/10.1103/RevModPhys.66.763> (cited on page 23).
- [127] A. Bohrdt, F. Grusdt, and M. Knap. “Dynamical formation of a magnetic polaron in a two-dimensional quantum antiferromagnet”. In: *Phys. Rev. Lett.* 101 (13 2019), p. 137207. DOI: [10.1103/PhysRevLett.101.137207](https://doi.org/10.1103/PhysRevLett.101.137207). arXiv: [1907.08214](https://arxiv.org/abs/1907.08214) [cond-mat.quant-gas]. URL: <https://link.aps.org/doi/10.1103/PhysRevLett.101.137207> (cited on page 23).
- [128] A. Omran. “A microscope for Fermi gases”. 2016. URL: <http://nbn-resolving.de/urn:nbn:de:bvb:19-194401> (cited on page 25).
- [129] M. Boll. “Spin and density resolved microscopy of Hubbard chains”. 2016. URL: <http://nbn-resolving.de/urn:nbn:de:bvb:19-202294> (cited on pages 25, 34).
- [130] D. S. C. Biggs and M. Andrews. “Acceleration of iterative image restoration algorithms”. In: *Appl. Opt.* 36.8 (13 1997), pp. 1766–1775. DOI: [10.1364/AO.36.001766](https://doi.org/10.1364/AO.36.001766). URL: <http://ao.osa.org/abstract.cfm?URI=ao-36-8-1766> (cited on page 34).
- [131] P. T. Brown, D. Mitra, E. Guardado-Sanchez, P. Schauß, S. S. Kondov, E. Khataimi, T. Paiva, N. Trivedi, D. A. Huse, and W. S. Bakr. “Spin-imbalance in a 2D Fermi-Hubbard system”. In: *Science* 357.6358 (13 2017), 1385–1388. DOI: [10.1126/science.aam7838](https://doi.org/10.1126/science.aam7838). URL: <https://science.sciencemag.org/content/357/6358/1385> (cited on page 35).
- [132] J. Sirker and A. Klümper. “Thermodynamics and crossover phenomena in the correlation lengths of the one-dimensional t-J model”. In: *Phys. Rev. B* 66 (24 2002), p. 245102. DOI: [10.1103/PhysRevB.66.245102](https://doi.org/10.1103/PhysRevB.66.245102). URL: <https://link.aps.org/doi/10.1103/PhysRevB.66.245102> (cited on page 36).

- [133] E. V. Gorelik, D. Rost, T. Paiva, R. Scalettar, A. Klümper, and N. Blümer. “Universal probes for antiferromagnetic correlations and entropy in cold fermions on optical lattices”. In: *Phys. Rev. A* 85 (6 2012), p. 061602. DOI: [10.1103/PhysRevA.85.061602](https://doi.org/10.1103/PhysRevA.85.061602). URL: <https://link.aps.org/doi/10.1103/PhysRevA.85.061602> (cited on pages 36, 37).
- [134] H. L. Essler, H. Frahm, F. Göhmann, A. Klümper, and V. E. Korepin. *The one-dimensional Hubbard model*. Vol. 101. Cambridge University Press, 2005, p. 137207. DOI: [10.1103/PhysRevLett.101.137207](https://doi.org/10.1103/PhysRevLett.101.137207). URL: <https://link.aps.org/doi/10.1103/PhysRevLett.101.137207> (cited on pages 36, 37).
- [135] B. Sciolla, A. Tokuno, S. Uchino, P. Barmettler, T. Giamarchi, and C. Kollath. “Competition of spin and charge excitations in the one-dimensional Hubbard model”. In: *Phys. Rev. A* 88 (6 2013), p. 063629. DOI: [10.1103/PhysRevA.88.063629](https://doi.org/10.1103/PhysRevA.88.063629). URL: <https://link.aps.org/doi/10.1103/PhysRevA.88.063629> (cited on page 37).
- [136] S. Trotzky, Y-A. Chen, U. Schnorrberger, P. Cheinet, and I. Bloch. “Controlling and Detecting Spin Correlations of Ultracold Atoms in Optical Lattices”. In: *Phys. Rev. Lett.* 105 (26 2010), p. 265303. DOI: [10.1103/PhysRevLett.105.265303](https://doi.org/10.1103/PhysRevLett.105.265303). URL: <https://link.aps.org/doi/10.1103/PhysRevLett.105.265303> (cited on page 37).
- [137] D. Greif, G. Jotzu, M. Messer, R. Desbuquois, and T. Esslinger. “Formation and Dynamics of Antiferromagnetic Correlations in Tunable Optical Lattices”. In: *Phys. Rev. Lett.* 115 (26 2015), p. 260401. DOI: [10.1103/PhysRevLett.115.260401](https://doi.org/10.1103/PhysRevLett.115.260401). URL: <https://link.aps.org/doi/10.1103/PhysRevLett.115.260401> (cited on page 37).
- [138] J. M. Tranquada, B. J. Sternlieb, J. D. Axe, Y. Nakamura, and S. Uchida. “Evidence for stripe correlations of spins and holes in copper oxide superconductors”. In: *Nature* 375.6532 (13 1995), pp. 561–563. ISSN: 1476-4687. DOI: [10.1038/375561a0](https://doi.org/10.1038/375561a0). URL: <https://doi.org/10.1038/375561a0> (cited on pages 39, 87).
- [139] T. A. Hilker, G. Salomon, F. Grusdt, A. Omran, M. Boll, E. Demler, I. Bloch, and C. Gross. “Revealing hidden antiferromagnetic correlations in doped Hubbard chains via string correlators”. In: *Science* 357.6350 (13 2017), pp. 484–487. ISSN: 0036-8075. DOI: [10.1126/science.aam8990](https://doi.org/10.1126/science.aam8990). URL: <http://science.sciencemag.org/content/357/6350/484> (cited on pages 44, 49, 57).
- [140] H. V. Kruis, I. P. McCulloch, Z. Nussinov, and J. Zaanen. “Geometry and the hidden order of Luttinger liquids: The universality of squeezed space”. In: *Phys. Rev. B* 70 (7 2004), p. 075109. DOI: [10.1103/PhysRevB.70.075109](https://doi.org/10.1103/PhysRevB.70.075109). URL: <https://link.aps.org/doi/10.1103/PhysRevB.70.075109> (cited on page 44).
- [141] J. Voit. “One-dimensional Fermi liquids”. In: *Rep. Prog. Phys.* 58.9 (13 1995), pp. 977–1116. DOI: [10.1088/0034-4885/58/9/002](https://doi.org/10.1088/0034-4885/58/9/002). URL: <https://doi.org/10.1088/0034-4885/58/9/002> (cited on page 49).
- [142] G. Salomon, J. Koepsell, J. Vijayan, T. A. Hilker, J. Nespolo, L. Pollet, I. Bloch, and C. Gross. “Direct observation of incommensurate magnetism in Hubbard chains”. In: *Nature* 565.7737 (13 2019), pp. 56–60. ISSN: 1476-4687. DOI: [10.1038/s41586-018-0778-7](https://doi.org/10.1038/s41586-018-0778-7). URL: <https://doi.org/10.1038/s41586-018-0778-7> (cited on pages 49, 57).

- [143] C. Kollath, U. Schollwöck, and W. Zwerger. “Spin-Charge Separation in Cold Fermi Gases: A Real Time Analysis”. In: *Phys. Rev. Lett.* 95.17 (13 2005), 176 bibrangedash 401. DOI: [10.1103/PhysRevLett.95.176401](https://doi.org/10.1103/PhysRevLett.95.176401). URL: <https://link.aps.org/doi/10.1103/PhysRevLett.95.176401> (cited on page 49).
- [144] G. A. Fiete. “Colloquium: The spin-incoherent Luttinger liquid”. In: *Rev. Mod. Phys.* 79.3 (13 2007), pp. 801–820. DOI: [10.1103/revmodphys.79.801](https://doi.org/10.1103/revmodphys.79.801). URL: <https://link.aps.org/doi/10.1103/PhysRevLett.101.137207> (cited on page 54).
- [145] J. Zaanen, O. Y. Osman, H. V. Kruis, Z. Nussinov, and J. Tworzydło. “The geometric order of stripes and Luttinger liquids”. In: *Philos. Mag. B* 81.10 (13 2001), pp. 1485–1531. DOI: [10.1080/13642810108208566](https://doi.org/10.1080/13642810108208566). URL: <https://link.aps.org/doi/10.1103/PhysRevLett.101.137207> (cited on page 57).
- [146] H. Castella, X. Zotos, and P. Prelovsek. “Integrability and Ideal Conductance at Finite Temperatures”. In: *Phys. Rev. Lett.* 74.6 (13 1995), pp. 972–975. DOI: [10.1103/PhysRevLett.74.972](https://doi.org/10.1103/PhysRevLett.74.972). URL: <https://link.aps.org/doi/10.1103/PhysRevLett.74.972> (cited on page 58).
- [147] X. Zotos, F. Naef, and P. Prelovsek. “Transport and conservation laws”. In: *Phys. Rev. B* 55.17 (13 1997), pp. 11029–11032. DOI: [10.1103/PhysRevB.55.11029](https://doi.org/10.1103/PhysRevB.55.11029). URL: <https://link.aps.org/doi/10.1103/PhysRevB.55.11029> (cited on page 58).
- [148] S. Kivelson and J. R. Schrieffer. “Fractional charge, a sharp quantum observable”. In: *Phys. Rev. B* 25.10 (13 1982), pp. 6447–6451. DOI: [10.1103/PhysRevB.25.6447](https://doi.org/10.1103/PhysRevB.25.6447). URL: <https://link.aps.org/doi/10.1103/PhysRevB.25.6447> (cited on page 67).
- [149] P. W. Anderson. “The Resonating Valence Bond State in La₂CuO₄ and Superconductivity”. In: *Science* 235.4793 (13 1987), pp. 1196–1198. ISSN: 0036-8075. DOI: [10.1126/science.235.4793.1196](https://doi.org/10.1126/science.235.4793.1196). eprint: <https://science.sciencemag.org/content/235/4793/1196.full.pdf>. URL: <https://science.sciencemag.org/content/235/4793/1196> (cited on page 77).
- [150] A. Auerbach and B. E. Larson. “Small-polaron theory of doped antiferromagnets”. In: *Phys. Rev. Lett.* 66 (17 1991), pp. 2262–2265. DOI: [10.1103/PhysRevLett.66.2262](https://doi.org/10.1103/PhysRevLett.66.2262). URL: <https://link.aps.org/doi/10.1103/PhysRevLett.66.2262> (cited on page 77).
- [151] M. Punk, A. Allais, and S. Sachdev. “Quantum dimer model for the pseudogap metal”. In: *Proceedings of the National Academy of Sciences* 112.31 (13 2015), pp. 9552–9557. ISSN: 0027-8424. DOI: [10.1073/pnas.1512206112](https://doi.org/10.1073/pnas.1512206112). eprint: <https://www.pnas.org/content/112/31/9552.full.pdf>. URL: <https://www.pnas.org/content/112/31/9552> (cited on page 77).
- [152] A. S. Alexandrov and J. T. Devreese. *Advances in polaron physics*. Vol. 101. Springer, 2010, p. 137207. ISBN: 9783642018961. DOI: [10.1007/978-3-642-01896-1](https://doi.org/10.1007/978-3-642-01896-1). URL: <https://link.aps.org/doi/10.1103/PhysRevLett.101.137207> (cited on page 77).
- [153] M. Lubasch, V. Murg, U. Schneider, J. I. Cirac, and M.-C. Bañuls. “Adiabatic Preparation of a Heisenberg Antiferromagnet Using an Optical Superlattice”. In: *Phys. Rev. Lett.* 107 (16 2011), p. 165301. DOI: [10.1103/PhysRevLett.107.165301](https://doi.org/10.1103/PhysRevLett.107.165301). URL: <https://link.aps.org/doi/10.1103/PhysRevLett.107.165301> (cited on page 85).

- [154] A. Kantian, S. Langer, and A. J. Daley. “Dynamical Disentangling and Cooling of Atoms in Bilayer Optical Lattices”. In: *Phys. Rev. Lett.* 120 (6 2018), p. 060401. DOI: [10.1103/PhysRevLett.120.060401](https://doi.org/10.1103/PhysRevLett.120.060401). URL: <https://link.aps.org/doi/10.1103/PhysRevLett.120.060401> (cited on page 85).
- [155] J. T. Stewart, J. P. Gaebler, and D. S. Jin. “Using photoemission spectroscopy to probe a strongly interacting Fermi gas”. In: *Nature* 454 (13 2008), 744 EP –. DOI: [10.1038/nature07172](https://doi.org/10.1038/nature07172). URL: <https://doi.org/10.1038/nature07172> (cited on page 87).
- [156] P. T. Brown, D. Mitra, E. Guardado-Sanchez, R. Nourafkan, A. Reymbaut, C.-D. Hébert, S. Bergeron, A.-M. S. Tremblay, J. Kokalj, D. A. Huse, P. Schauf, and W. S. Bakr. “Bad metallic transport in a cold atom Fermi-Hubbard system”. In: *Science* 363.6425 (13 2019), pp. 379–382. ISSN: 0036-8075. DOI: [10.1126/science.aat4134](http://science.sciencemag.org/content/363/6425/379). URL: <http://science.sciencemag.org/content/363/6425/379> (cited on page 87).
- [157] Nichols, M. A. and Cheuk, L. W. and Okan, M. and Hartke, T. R. and Mendez, E. and Senthil, T. and Khatami, E. and Zhang, H. and Zwierlein, M. W. “Spin transport in a Mott insulator of ultracold fermions”. In: *Science* 363.6425 (13 2019), pp. 383–387. ISSN: 0036-8075. DOI: [10.1126/science.aat4387](http://science.sciencemag.org/content/363/6425/383). URL: <http://science.sciencemag.org/content/363/6425/383> (cited on page 87).
- [158] J. M. Tranquada, D. J. Buttrey, V. Sachan, and J. E. Lorenzo. “Simultaneous Ordering of Holes and Spins in $\text{La}_2\text{NiO}_{4.125}$ ”. In: *Phys. Rev. Lett.* 73 (7 1994), pp. 1003–1006. DOI: [10.1103/PhysRevLett.73.1003](https://link.aps.org/doi/10.1103/PhysRevLett.73.1003). URL: <https://link.aps.org/doi/10.1103/PhysRevLett.73.1003> (cited on page 87).
- [159] S. R. White and D. J. Scalapino. “Density Matrix Renormalization Group Study of the Striped Phase in the 2D $t - J$ Model”. In: *Phys. Rev. Lett.* 80 (6 1998), pp. 1272–1275. DOI: [10.1103/PhysRevLett.80.1272](https://link.aps.org/doi/10.1103/PhysRevLett.80.1272). URL: <https://link.aps.org/doi/10.1103/PhysRevLett.80.1272> (cited on page 87).
- [160] J. von Stecher, E. Demler, M. D. Lukin, and A. M. Rey. “Probing interaction-induced ferromagnetism in optical superlattices”. In: *New Journal of Physics* 12.5 (13 2010), p. 055009. DOI: [10.1088/1367-2630/12/5/055009](https://doi.org/10.1088/1367-2630/12/5/055009). URL: <https://doi.org/10.1088/1367-2630/12/5/055009> (cited on page 88).
- [161] E. C. Stoner and E. P. Wohlfarth. “A Mechanism of Magnetic Hysteresis in Heterogeneous Alloys”. In: *Philosophical Transactions of the Royal Society A: Mathematical, Physical and Engineering Sciences* 240 (826 1948), pp. 599–642. DOI: [10.1098/rsta.1948.0007](https://doi.org/10.1098/rsta.1948.0007). URL: <https://link.aps.org/doi/10.1103/PhysRevLett.101.137207> (cited on page 88).
- [162] G.-B. Jo, Y.-R. Lee, J.-H. Choi, C. A. Christensen, T. H. Kim, J. H. Thywissen, D. E. Pritchard, and W. Ketterle. “Itinerant Ferromagnetism in a Fermi Gas of Ultracold Atoms”. In: *Science* 325.5947 (13 2009), pp. 1521–1524. ISSN: 0036-8075. DOI: [10.1126/science.1177112](https://science.sciencemag.org/content/325/5947/1521.full.pdf). eprint: <https://science.sciencemag.org/content/325/5947/1521.full.pdf>. URL: <https://science.sciencemag.org/content/325/5947/1521> (cited on page 88).
- [163] G. Valtolina, F. Scazza, A. Amico, A. Burchianti, A. Recati, T. Enss, M. Inguscio, M. Zaccanti, and G. Roati. “Exploring the ferromagnetic behaviour of a repulsive Fermi gas through spin dynamics”. In: *Nature Physics* 13.7 (13 2017), pp. 704–709. ISSN: 1745-2481. DOI: [10.1038/nphys4108](https://doi.org/10.1038/nphys4108). URL: <https://doi.org/10.1038/nphys4108> (cited on page 88).

- [164] S. S. Kancharla and S. Okamoto. “Band insulator to Mott insulator transition in a bilayer Hubbard model”. In: *Phys. Rev. B* 75 (19 2007), p. 193103. DOI: [10.1103/PhysRevB.75.193103](https://doi.org/10.1103/PhysRevB.75.193103). URL: <https://link.aps.org/doi/10.1103/PhysRevB.75.193103> (cited on page 89).
- [165] M. Golor, T. Reckling, L. Classen, M. M. Scherer, and S. Wessel. “Ground-state phase diagram of the half-filled bilayer Hubbard model”. In: *Phys. Rev. B* 90 (19 2014), p. 195131. DOI: [10.1103/PhysRevB.90.195131](https://doi.org/10.1103/PhysRevB.90.195131). URL: <https://link.aps.org/doi/10.1103/PhysRevB.90.195131> (cited on page 89).
- [166] T. A. Maier and D. J. Scalapino. “Pair structure and the pairing interaction in a bilayer Hubbard model for unconventional superconductivity”. In: *Phys. Rev. B* 84 (18 2011), p. 180513. DOI: [10.1103/PhysRevB.84.180513](https://doi.org/10.1103/PhysRevB.84.180513). URL: <https://link.aps.org/doi/10.1103/PhysRevB.84.180513> (cited on page 89).
- [167] R. T. Scalettar, J. W. Cannon, D. J. Scalapino, and R. L. Sugar. “Magnetic and pairing correlations in coupled Hubbard planes”. In: *Phys. Rev. B* 50 (18 1994), pp. 13419–13427. DOI: [10.1103/PhysRevB.50.13419](https://doi.org/10.1103/PhysRevB.50.13419). URL: <https://link.aps.org/doi/10.1103/PhysRevB.50.13419> (cited on page 89).
- [168] S. Chakravarty, A. Sudbø, P. W. Anderson, and S. Strong. “Interlayer Tunneling and Gap Anisotropy in High-Temperature Superconductors”. In: *Science* 261.5119 (13 1993), pp. 337–340. ISSN: 0036-8075. DOI: [10.1126/science.261.5119.337](https://doi.org/10.1126/science.261.5119.337). eprint: <https://science.sciencemag.org/content/261/5119/337.full.pdf>. URL: <https://science.sciencemag.org/content/261/5119/337> (cited on page 89).

Acknowledgements

Learning is a continuous process that begins at birth. Every single teacher of mine has, in some way or another, contributed in leading me to this stage of my life where I am completing my PhD. It would be impossible to name them all, and I shall restrict myself to the ones who gave me company and support during the last three and a half years.

First and foremost, none of the results presented here would have been possible without the team working in the lab - Joannis Koepsell, Guillaume Salomon, Timon Hilker, Pimonpan Sompert, Sarah Hirthe, Dominik Bourgund, Martin Boll and Ahmed Omran. I will never forget all the times where one of us had to couple a fiber in one end of the room while the other measured optical power at a location that was only accessible by sneaking in their hand at uncomfortable angles in the other end of the room. Or the joy of unwrapping a new laser and the sadness (to the point of indifference) of dealing with the death of old lasers. Thank you for sharing the lab experience with me and peacefully resolving conflicts involving Thorlabs snacks.

A team can only be successful with the right leadership. I've had the fortune of being mentored by two of the finest physicists in the field today. Christian Gross, for having an inexplicable knack for getting things to work efficiently - be it computer code, paper drafts, optical setups or me! Immanuel Bloch, for somehow always managing to be aware of the latest developments in the lab and knowing which directions to take, for effortlessly spreading his infectious enthusiasm and for never letting us worry about available funds. I am very grateful for your supervision.

A day at work also involves taking lunch and kicker breaks, which has led to plenty of interesting conversations and crawling under the table. For this, I additionally thank Joop Adema, Roman Bause, Petar Bojovic, Jae-yoon Choi, Marcel Duda, Scott Eustice, Lorenzo Festa, Christoph Gohle, Rudolf Haindl, André Heinz aka Kicker Son-Goku, Simon Hollerith, Nikolaus Lorenz, Joaquin Minguzzi, Philip Osterholz, Annie Park, Antonio Rubio-Abadal, Jun Rui, Neven Santic, Frauke Seeßelberg, Andreas Schindewolf, Etienne Staub, Lea-Marina Steinert, Jan Trautmann, Anne-Sophie Walter, David Wei, Johannes Zeiher. I also thank Monika Aidelsburger, Pranjal Bordia, Nelson Darkwah-Oppong, Simon Fölling, Sebastian Scherg, Christian Schweizer and Karen Wintersperger from the LMU labs for helping me out when I needed it.

My time as a student here has been made a thousand times easier thanks to the support of Kristina Schuldt, Ildiko Kecskesi, Doreen Seidl, Anton Mayer, Karsten Förster, Olivia Mödl and Bodo Hecker.

Thanks also to Fabian Grusdt and Annabelle Bohrdt for being fantastic collaborators and friends.

A special thanks to all those people who were instrumental to the "life" in work-life balance. I could not have completed my PhD without your support. A huge

thanks to the entire MINT Ultimate community for showing me how to mix competition and fun. For keeping me fresh, for sending it and for all the memories. You are amazing friends and every morning I wake up surprised you still want to hang out with me despite my sense of humour. Many thanks to Laura Kleinknecht for being there for me throughout the duration of my thesis. Thanks to all the others who made me feel welcome in this strange and foreign land - Frau Graf, the folks at Toytown, Chiara Decaroli, Josep cabedo Bru, Fadi Salti, Marce Giraldo and the rest of the Europhotonics gang, the group of Morgan Mitchell and Pamina Winkler. And finally, to my parents - you are reading this thesis today only because you encouraged me to be curious at a young age and gave me the freedom to pursue what I wanted. Thank you.